UNIVERSITY OF BERGEN
Faculty of Mathematics and Natural Sciences

Peak-summer energy and carbon fluxes on a thawing permafrost site

Master's thesis in Meteorology

Isak Haldorsson Slettebø

November 20, 2018

Acknowledgements

First, I would like to thank Anak for coming with me all the way to Finnmark in mid-summer, carrying some pretty heavy gear to the field and helping me install the instruments. I say as Al Capone: 'You can get much further with a kind word and a Nepalese than with a kind word alone.'

Next, I want to thank my supervisors Hanna and Jochen for helpful feedback on short notice and throughout this year, and for allowing me to follow my own interests within this very interdisciplinary project.

Thanks to my co-supervisor Casper as well as Renée, Jack and Althug for a nice time in the field, especially the dinners, the card games and the many car trips. Casper together with Hanna also gave valuable input on my abstract for the EGU conference, which allowed me to go to Austria and present my study. My second co-supervisor Stephan kindly introduced me to the initially confusing TK3 software, and he and Jochen tipped me about the summer field course in Schleswig, which was extremely useful. Danke sehr! A big thanks to my friend Juan Michael Sargado who out of pure charity helped me with the ogives, despite having his own PhD to finish. Sebastian Westermann and Norbert Pirk also deserve mentioning for letting me know about the footprint tool.

I am grateful for all the lecturers I have had during these years, especially Helge Drange, Thomas Spengler and Harald Sodemann at UiB, Marius Jonassen and the UNIS people, and Christoph Thomas and Wolfgang Babel at Bayreuth.

Jeg var så heldig å få økonomisk støtte fra fylkeskommunen til å dra på konferanser. Tusen takk, Hordaland!

Men de som har preget studietiden min mest, er selvsagt alle medstudentene. Viktigst har det vært med de sene kveldene på Rommet og i kantina, inkludert karaokesiesta og smalahovemiddager, og 17. maiferinger.

Omsorg og videre økonomisk støtte har jeg primært Mamma og Pappa (og Lånekassen) å takke for, som jeg selv etter 24 år på Jorden er ganske avhengig av. Til slutt vil jeg takke Vårherre for inspirasjon gjennom hele studieløpet.

Cover image: View of the field site from Iškoras. Photographer: Renée McDonald.

Contents

Abstract

We present measurements of surface fluxes taken between 7 July and 6 August 2017, on a palsa mire near the Iškoras mountain in Finnmark, northern Norway. Palsa mires are a particular landform found at the edge of the discontinuous permafrost zone, where mean annual temperatures are close to 0 °C and climate change is expected to have a high impact.

Turbulent fluxes of sensible heat, latent heat and CO_2 were measured with the eddy-covariance (EC) method, while complementary energy balance data was provided by a net radiometer and two soil heat flux plates. The raw turbulence data was processed by the validated TK3 software package, which applies the plausability tests, corrections and quality controls needed for reliable flux calculations. Through a footprint analysis we found the average turbulent fetch area to overlap well with our ecosystem of interest, in that only 20 % of the footprint climatology was outside the palsa mire. However, we observed a greater carbon uptake during northerly winds than otherwise, which suggests that the more vegetated area to the north of the palsa mire also influenced our flux measurements.

Overall, our results are similar to those of other studies from the growing season at sub-Arctic sites. The mean daytime Bowen ratio was 74 %, which is typical for high-latitude wetlands in summertime. The soil heat flux was positive most of the time, and our cumulative flux estimates indicated a large soil heat uptake during the campaign, which is characteristic for permafrost regions during the warm season. However, the average flux from the upper sensor at 10 cm was only 8 % of the net radiation. This is in general less than what other permafrost studies have found for the ground heat flux, likely due to the deep sensor placement in the soil. The average net ecosystem exchange of CO_2 during the campaign was –1.1 μmol/m^{2}s, which indicates carbon uptake and compares well to what has been reported in other studies from similar sites in summertime. Differences in carbon budgets between sub-Arctic ecosystems seem to be associated with the vegetation cover. A certain long-term increase in CO_2 flux amplitude was found, likely related to vegetation growth. We were not able to verify the surface energy balance equation with our measurements, but using longwave radiation data we managed to estimate the true ground heat flux at the surface. This gave a better, though not perfect, balance. Our ogive test suggested that a significant fraction of the turbulent fluxes were inadequately sampled with a block averaging period of only 30 min, which also contributed to the observed imbalance in surface heat fluxes.

Chapter 1

Introduction

Permafrost regions have received considerable scientific attention in recent decades (Hinzman and Kane, 1992; Vourlitis and Oechel, 1999; Davidson and Janssens, 2006). While Arctic ecosystems have historically acted as carbon sinks (Oechel et al., 2000), research now indicates that global warming might trigger a positive climate feedback loop of permafrost carbon release to the atmosphere as greenhouse gases, due to the thawing of previously frozen soils (Stocker et al., 2013, p. 93). Thawing will enhance the microbial breakdown of organic carbon, which can shift northern tundra soils to a carbon source.
Estimates of the carbon reservoir contained in northern permafrost soils have varied over the last decades – generally they have increased substantially since the 1990s but decreased slightly during recent years. Currently, the northern terrestrial permafrost region is believed to hold around around 1300 ±200 Pg of soil organic carbon, even though large uncertainties remain, especially due to e.g. data gaps in the high Arctic (Tarnocai et al., 2009; Hugelius et al., 2014). This is twice the amount of carbon present in the atmosphere and about 40 % of the global soil organic carbon pool, and if just a fraction of the permafrost carbon were released to the atmosphere as greenhouse gases, it could accelerate climate change (Tarnocai et al., 2009; Schuur et al., 2008, 2015).
Even more difficult to assess than the carbon pool size is how the permafrost will respond to present and future warming. The spread in man-made greenhouse gas emission scenarios translates to a difference of several °C in future global temperature increase, which places an upper bound for predictability in any branch of climate change (see Ciais et al., 2013, p. 519). However, even if perfect information on future anthropogenic emissions were available, substantial uncertainty would remain for the case of permafrost carbon. In fact, permafrost carbon is one of the least understood climate feedback mechanisms, despite its potentially large contribution to climate change (Kuhry et al., 2010; Tarnocai et al., 2009). Major uncertainties are due to an insufficiant understanding of permafrost soil mechanisms, such as 1) the rate of thawing, and 2) the timing and fraction of soil carbon release after thawing, and 3) the ratio of CO_2/methane emissions after thawing (Ciais et al., 2013, p. 528).

Several mitigating effects such as greater permafrost carbon uptake by plants due to

e.g. higher temperatures, increased nutrient availability and elevated atmospheric CO_2 levels, as well as reduced snow cover which could lead to stronger wintertime cooling of the soil, add further complication to the predicted fate of permafrost carbon (Stieglitz et al., 2003; Schuur et al., 2008). Consequently, modelling approaches of the permafrost carbon cycle under future warming do not yield consistent results (Collins et al., 2013, p. 1116), and the earth system models employed for the IPCC's Fifth Assessment Report of 2013 did not include any explicit representation of this feedback (Ciais et al., 2013; Schuur et al., 2015, p. 526).

The sheer size of the permafrost carbon pool and the amplified warming observed in high northern latitudes, as well as the mentioned uncertainties in predicting the feedback mechanism, suggest that careful monitoring of permafrost regions is much needed. This applies perhaps especially to the warmer permafrost regions, which have mean annual temperatures close to 0 °C and are particularly sensitive to climate change (Christensen et al., 2004). Furthermore, land-cover changes associated with permafrost degradation warrant greater attention towards the surface energy balance in high latitudes, because the impacts on land-atmosphere coupling processes such as evaporation and radiation budgets are poorly understood (Stiegler et al., 2016).

1.1 Permafrost basics

Permafrost regions occupy about 24 % of the exposed land area in the northern hemisphere, while there are also large permafrost areas under the Arctic Ocean continental shelf (Heginbottom et al., 2013; Schuur et al., 2015). The permafrost warming is well-documented and has been going on for at least 30 years (Brown and Romanovsky, 2008), whereas the air temperature in high northern latitudes has risen by 0.6 °C per decade over the same period – twice the global average warming rate (Schuur et al., 2015). Further permafrost retreat will follow as global temperatures continue to rise in the future, but projections of the associated changes in the carbon cycle are poorly constrained.

1.1.1 Definition

The term "permafrost" was coined by Muller (1947, p. 3) and defined as ground in which a temperature below 0 °C has existed continuously for at least two years. However, even in permafrost regions, the surface layer of ground, referred to as the active layer and briefly discussed in Section 2.6, is only seasonally frozen. Below the active layer, most permafrost is indeed consolidated by ice, but there are situations where water does not freeze at temperatures < 0 °C, due to e.g. chemical solutes in the ground water. The definition proposed by Muller (1947) is basically still valid today (van Everdingen, 1998, p. 55) and is given solely according to the temperature criterion, regardless of texture, water content and other ground characteristics. Permafrost is often associated with soils, but Muller (1947) prefers using 'ground', because frozen conditions can also affect other earth material such as bedrock and sediment.

1.1.2 Permafrost zones

On a regional scale, permafrost is not simply present or absent – rather, it is classified in a spectrum according to its lateral extent as a proportion of a larger area. Such a categorisation results in 2-4 permafrost zones worldwide (Péwé, 2018; Heginbottom et al., 2013; Bolch and Christiansen, 2015). In the continuous permafrost zone, more than 90 % of the ground area is underlain by permafrost, whereas discontinuous permafrost covers between 0 and 90 % of the ground area. This zone is therefore subdivided into permafrost that is e.g. *widespread* (50-90 % extent), *sporadic* (10-50 %) and permafrost that occurs in *isolated patches*. The distribution of permafrost in the northern hemisphere is illustrated in Fig. 1.1.

Figure 1.1: Distribution and classification of permafrost zones in the northern hemisphere. Cartographer: Ahlenius (2007).

The permafrost zones are largely organized in a north-south pattern, with the very cold continuous permafrost zone dominating north of the polar circle, and the more temperate discontinuous permafrost zone occupying more of the sub-Arctic regions. One exception, which is the basis of the present thesis, is the Fennoscandian lowland permafrost.[1] This permafrost is relatively high-latitude (65 °to 71 °N), but mostly sporadic in extent due to the warming by Atlantic ocean currents. Moreover, its influence increases towards the south, i.e. away from the coast, because of the more favourable continental climate in the interior of the peninsula (Åhman, 1977, p. 12).

[1]By *lowland* we refer to terrain elevated by not more than ~ 500 m.a.s.l., and exclude the alpine permafrost found in mountain areas such as Dovre and Jotunheimen in southern Norway, following Gisnås (2011).

1.1.3 Palsas

A common landform associated with permafrost in Fennoscandia is palsas (Borge et al., 2017). Palsas are mounds of peat possessing a frozen core of ice and peat or mineral soil (van Everdingen, 1998, p. 51), and peat is plant material which, due to anaerobic conditions, does not fully decay. Palsas range in height from about 0.5 m to 7 m, but rarely exceed 4 m on Finnmarksvidda, and are typically wider than 2 m in diameter.

The genesis and characteristics of palsas are still a topic of fruitful debate (Seppälä, 2011), and there are at least three explanations to how palsas form (Guerney, 2001). One of these is the snow-cover mechanism. According to this theory, palsas are formed locally in places where the wintertime snow cover is thinner than in adjacent areas. Winter cooling can then penetrate more deeply in the soil, so that the frost survives summertime thaw. Areas with too much wintertime precipitation will not support palsa formation, due to the protective effects of a thick snow cover – Åhman (1977) found the limit of palsa extent in northern Norway to coincide well with the 100 mm winter precipititation curve, which separates the dry interior landscape from the coastal zone. Bare, windswept areas within such a curve will rise above the surroundings, be still more exposed to the wind and experience a low snow cover also in the following years, inducing a positive feedback mechanism.

Palsas are probably the most striking indication of permafrost near the southern fringe of the discontinous permafrost zone (Åhman, 1977, p. 18), and can provide very useful information for monitoring the state of permafrost in the areas sensitive to climate change (Guerney, 2001). Indeed, recent palsa degradation has been documented in both Fennoscandia (Borge et al., 2017; Zuidhoff and Kostrup, 2000) and North America (Vallée and Payette, 2007). Seppälä (2011) argues that the reported palsa retreat might not be associated with global warming, but could be the result of (random) changes in the hydrological cycle. However, at least in northern Norway, a moderate positive trend in precipitation since 1915 has been observed (Vikhamar-Schuler et al., 2010), and precipitation is expected to increase by about 20 % – mostly in summertime – by the end of this century, likely related to climate change (Norsk klimaservicesenter, 2016). This comes in addition to the projected future temperature increase, which is expected to be especially strong in wintertime.

1.2 Brief history of eddy covariance

A greater need for monitoring ecosystem processes, motivated not just by the permafrost carbon feedback but more generally by the global changes seen in the atmosphere and biosphere since the industrial revolution, prompted the launch of several ground-based measurement networks in the 1990s such as Euroflux (Aubinet et al., 2000), AmeriFlux (Rannik et al., 2012, p. 243), and eventually the global FLUXNET (Baldocchi et al., 2001). The hundreds of FLUXNET sites are spread across all continents and measure the flux of CO_2, water vapor and sensible heat on a continuous and long-term basis, using the *eddy covariance* (EC) method.

The EC technique provides the most reliable direct measurement of turbulent fluxes (Arya, 2001, p. 227). Important theoretical groundwork for the EC method was laid in the late 19th and early 20th century, by German and British scientists such as Osborne Reynolds, Ludwig Prandtl and Geoffrey Taylor (Faber, 2018). However, the direct measurement of eddies using fast-response anemometers was proposed only in 1946 by the Russian physicist Alexander M. Obukhov (see Foken, 2006) for momentum flux, and soon by e.g. Montgomery (1948) for fluxes of heat and water vapor. Instrumentation came about in the wake of these studies, but applications were limited until modern sonic anemometry was invented in the early 1960s. Up to the 1980s, micrometeorological experiments in the US, Europe and USSR were not designed to monitor fluxes over a range of different ecosystems, but rather to investigate fundamental features of atmospheric turbulence over homogeneous and eventually heterogeneous terrain (Foken et al., 2012a, p. 2). Only once refinements in sonic anemometry and infrared spectrometry in the 1980s and 1990s allowed for continuous flux measurements, and processing software became accessible to ecosystem scientists, did the EC method evolve into a widely used technique – also for CO_2 flux measurements. Micrometeorological measurements of CO_2 exchange had been taken for several decades at this time, but not using eddy covariance – the earlier studies would employ the so-called flux-gradient method, which is based on the gradient of a constituent between two vertical levels. Several other methods for measuring the CO_2 flux exist and are still in use today, such as plant and soil chambers and leaf-cuvettes. These techniques provide valuable spatial resolution which can be used to measure the variability within a plant community, and also allow the partitioning into different CO_2 flux components. However, they disturb the local conditions, introducing error, and measure only at a point scale, which makes it difficult to estimate the average CO_2 exchange from a large ecosystem (Baldocchi, 2003).

1.3 State of the art

In this thesis, we measure the eddy-covariance fluxes of CO_2 and energy at a thawing palsa mire in Finnmark, northern Norway, during the 2017 peak summer. With complementary measurements we estimate the full surface energy balance, which is often used as a quality control of EC data (Aubinet et al., 2000). Since the surface energy balance is an important meteorological concept regardless of the carbon cycle, we put emphasis on all the different energy components as well as the carbon exchange.

Evidence for widespread and sustained palsa degradation in Finnmark was reported by Borge et al. (2017). They concluded that lateral erosion of palsas in Finnmark has been going on for several decades, possibly since before 1950, and speculated that present changes observed in Fennoscandia might foreshadow what lies ahead for the much larger and colder permafrost regions in Russia, for example. However, very few field studies on carbon and energy exchange have been conducted in the Nordic permafrost region, though we are not the first.

Laurila et al. (2001) measured the annual eddy flux of CO_2 between 1996 and 1998 at several sites in northern Finland, Greenland and on Svalbard, some underlain by permafrost. They argued that, although climate warming could stimulate plant growth in

summertime, a prolonged growing season might not magnify the carbon uptake, because autumn light supply will remain scant also in the future. On the other hand, soil respiration rates would not face such limitations and could be more sensitive than photosynthesis to climate change. Nykänen et al. (2003) installed an array of static chambers on a palsa mire in Finland and recorded the annual CO_2 and methane budgets for 1998 and 1999. The wet surfaces and the shrub-vegetated palsa surfaces were annual carbon sinks, whereas the bare palsa surface was a carbon source. Using the eddy-covariance method, Christensen et al. (2012) reported an annual uptake of CO_2, but a release of methane, between 2001 and 2008 on a palsa mire at Stordalen in northern Sweden.

In the same area, Stiegler et al. (2016) compared the surface energy balance on three different peatland sites during the 2013 summer, and found a shift towards greater latent heat release on the degraded permafrost, relative to the still intact palsa ecosystems. O'Shea et al. (2014) measured CO_2 and methane fluxes using both a ground-based (EC and chamber) station and airborne sensing along transects over forests and peatlands in northern Finland and Sweden. While not all of these areas were underlain by permafrost, Olefeldt et al. (2012) reported an annual carbon accumulation at the Stordalen palsa mire similar to that of permafrost-free boreal peatlands. This was also observed by Nykänen et al. (2003).

A large body of eddy-covariance studies exists for the Canadian, Alaskan and Russian permafrost regions as well (Laurila et al., 2012, Table 14.1). However, to our knowledge the only eddy-covariance studies in Norway have been conducted on Svalbard, such as by Westermann et al. (2009). Furthermore, a permafrost map of Norway, Sweden and Finland presented by Gisnås et al. (2016) suggests that the permafrost influence is quite variable even within Fennoscandia. Studies in different parts of this region are therefore needed to account for the diversity in e.g. climate and vegetation, which may influence the exchange of carbon and energy.

Our study will add to the sparse data set on heat and carbon exchange in the Arctic, but we hope it may also inspire similar efforts across the high latitudes, in all seasons and using different methods – especially in the very under-sampled and under-recognized parts of Canada and Russia (Metcalfe et al., 2018).

Chapter 2

Theory

2.1 Surface energy balance

Most of the energy in the atmosphere is transferred at the surface Foken (2008b, p. 8), where solar irradiance is abruptly converted into other energy fluxes. If we imagine the surface as an infinitesimally thin layer with zero heat capacity, there can be no heat storage in this layer, and due to energy conservation, the heat fluxes at such an idealized surface must be balanced. Both the atmosphere and the deeper ground are engaged in this energy redistribution, which is given by

$$-R_{net} = SH + LH + Q_G \tag{2.1}$$

The instantaneous net radiation $-R_{net}$ is equal to the sum of the sensible and latent turbulent heat fluxes SH and LH, and the ground heat flux Q_G. Under special conditions, eq. 2.1 does not include all components relevant to the energy transfer – contributions from e.g. heat storage in plants might play a role over vegetated ground (Liebethal, 2006, p. 2). However, on relatively bare surfaces such as the peat mire of our study, eq. 2.1 seems adequate, and the heat storage term is omitted following Munn (1966, p. 3).
Using the sign convention outlined by Foken (2008b, p. 9), we consider fluxes out of surface as positive, and those into the surface as negative. This might seem counterintuitive, but it has the advantage that all terms on the right hand side of eq. 2.1 become positive at noon.

In the following, we will go through all the terms of the surface energy balance, because a good understanding of each component is necessary in order to discuss a) the overall energy budget near Iškoras in the peak summer of 2017 and b) the surface energy balance closure problem, which sheds light on the quality of our eddy-covariance measurements.

2.2 Radiation

Solar radiation is the driving source of energy for the planet earth and is the ultimate cause of all weather phenomena (Marchgraber, 1967; Trenberth et al., 2009). The solar irradiance received by a horizontal surface at the outer edge of the earth's atmosphere at zero zenith angle, referred to as the solar irradiance, is about 1361 W/m^2 (Ohmura, 2012, p. 5).[1] It can be described by the Stefan-Boltzmann law, which relates the surface temperature T of a body to its irradiance F:

$$F = \epsilon\sigma T^4 \tag{2.2}$$

where $\sigma = 5.67 \cdot 10^{-8} \frac{W}{m^2 K^4}$ is the Stefan-Boltzmann constant and $\epsilon \in [0, 1]$ is the emissivity, which depends on the surface and the wavelength. Note that the sun, which has a surface temperature of $\sim$ 6000 K, emits at a much greater intensity than any terrestrial bodies. For perfect *black bodies*, ϵ is unity in all wavelengths. Most natural surfaces are not black but rather *grey bodies*, yet their emissivities are usually greater than 0.9 (Arya, 2001, p. 31).

Because the projection of Earth onto a surface normal to the sun's rays is a circle with an area of πr^2_{earth}, whereas the total surface area of a sphere is $4\pi r^2$, we need to divide the solar irradiance by 4 to obtain the average solar emission incident on Earth. This gives a mean radiant flux density of about 341 W/m^2 available for consumption by the Earth's atmosphere and surface. In total, 30 % of this incoming radiation is scattered or reflected out to space by clouds, aerosols, air molecule and the surface (Wallace and Hobbs, 2006, p. 420). If the rest were simply absorbed by the surface and re-emitted out to space, the Earth would have a temperature of only 255 K, and would not support life except perhaps in the deep ocean (Chapin III et al., 2011, p. 24).
Strictly speaking, the Earth's radiative emission *must* balance the heat received by the sun in order to maintain thermodynamic equilibrium (see Wallace and Hobbs, 2006, Fig. 10.1), and the emission from the atmosphere out to space is indeed that of a black body at 255 K. Fortunately, the Earth's surface itself does *not* need to balance the solar radiation, and due to the warming effect of the atmosphere, it has a comfortable mean temperature of about 288 K.
In addition to the reflected 30 % of the solar radiation, another 20 % is absorbed primarily by tropospheric water vapor and clouds, but also partly by ozone in the stratosphere. The remaining 50 % is absorbed by the surface.
Even though the atmosphere and Earth in total emit the same amount of energy as they absorb, the spectral characteristics of the absorbed and emitted radiation are very different. In Fig. 2.1, the normalised radiative emission is plotted against wavelength for two black bodies: one with a surface temperature of 6000 K, corresponding to the sun, and one with a temperature of 250 K, corresponding roughly to the Earth and atmosphere. There

[1] Sources differ on the exact magnitude of the solar irradiance, with estimates ranging from 1350 to 1400 W/m^2 (Arya, 2001, p. 33). The solar irradiance was formerly termed the solar constant, but this is now considered inaccurate as the solar irradiance was found to vary on several timescales, most notably the solar cycle, which lasts for about 11 years and has an amplitude of $\sim$ 1 W/m^2 (Wallace and Hobbs, 2006, pp. 439-440).

is a clear separation between the two curves, with almost no overlap in the intermediate region around 4 μm.

Thus, radiation in the atmosphere is typically separated into two classes (Andrews, 2000, p. 53):

- Solar, or shortwave, radiation, which ranges from the ultra-violet region to the near-infrared region, between roughly 0.1 and 4 μm. The solar spectrum has a wavelength of peak intensity at $\approx$ 0.475μm, and the visible range, which lies between 0.39 μm and 0.76 μm, happens to be at the (logarithmic) centre of this spectrum.

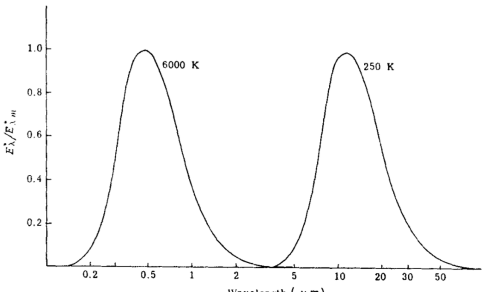

Figure 2.1: Normalised black-body irradiance per unit wavelength for the sun (left) and the Earth (right). Adopted from Fleagle and Businger (1980, p. 226).

- Thermal, or longwave, radiation, which has wavelengths from about 4 to 100 μm. This range is contained within the infrared region, but can be subdivided into thermal and far infrared radiation.

Shortwave radiation may be scattered or reflected by the atmosphere or the surface, but ultimately it originates from the sun, which has a surface temperature of about 6000 K. Longwave photons, however, are emitted directly from the ground or atmosphere, and with a significantly cooler surface, the Earth has a black-body spectrum shifted towards much longer wavelengths. In fact, the wavelength of peak intensity $\lambda_{\max}$ emitted by a black body is inversely proportional to the surface temperature of that body:

$$\lambda_{max} = \frac{2897}{T} \tag{2.3}$$

This equation is known as Wien's displacement law, because black-body emission plotted against wavelength is *displaced* towards lower wavelengths as the temperature rises. It can be shown that the sun's surface temperature as calculated from eq. 2.2 departs by about 6 % from its surface temperature predicted by eq. 2.3 (Wallace and Hobbs, 2006, pp. 119), which means that the sun is not a perfect black body, even though it may be approximated as one (Munn, 1966, p. 9).

Because the vertical is the main axis of radiative energy transfer in the atmosphere, it is useful in micrometeorology to subdivide the two radiation components into *upwelling* and *downwelling* terms. The net radiation R_{net} received at the surface can then be expressed as

$$--R_{net} = -SD - LD + SU + LU \tag{2.4}$$

where S and L denote shortwave and longwave radiation, and D and U indicate downwelling and upwelling, respectively, following the same sign convention as before. A typical diurnal course in the absence of clouds is given in Fig. 2.2.

SD can come directly from the sun or from the atmosphere as scattered radiation, and depends not just on latitude, topography, season and time of day, but also on cloud cover, aerosols and to some extent the water vapor content of the atmosphere. On clear days, SD follows a strict diurnal cycle, rising from zero some time in the morning and culminating around noon, but aerosols can modify this cycle through scattering and reflection, and atmospheric gases such as oxygen, ozone and CO_2 do absorb shortwave radiation at certain wavelength bands (Arya, 2001). In midnight sun conditions such as during the first half of our campaign, SD does not vanish completely at night, but can reach down to less than 1 W/m^2. SU is the part of SD that is reflected by the ground, and the magnitude of this term depends on the so-called albedo coefficient α:

$$\alpha = -\frac{SD}{SU} \tag{2.5}$$

The albedo is a measure of the 'whiteness' or reflectivity of the particular surface. Like emissivity, the reflectivity varies with wavelength: Grass is green because it reflects green light and absorbs most of the other colors (Munn, 1966, p. 14). However, in meteorological applications we are not interested in the wavelength-dependent characteristics of radiative transfer, but rather the total fluxes integrated over all wavelengths in the solar or terrestrial spectrum. Thus, albedo represents the reflectivity integrated over short wavelengths, e.g. between roughly 0.3 and 4 μm, and is assumed negligible in the infrared spectrum, whereas emissivity refers to the longwave spectrum (Rosenberg et al., 1983, p. 42). This is why black bodies are not necessarily black in color: Fluffy snow, for instance, is at the same time one of the best emitters – in the longwave spectrum – and reflectors – in the shortwave spectrum – found in nature, with albedo and emissivity up to > 0.95 and > 0.99, respectively (see Munn, 1966; Arya, 2001; Foken, 2008b, chap. 1).

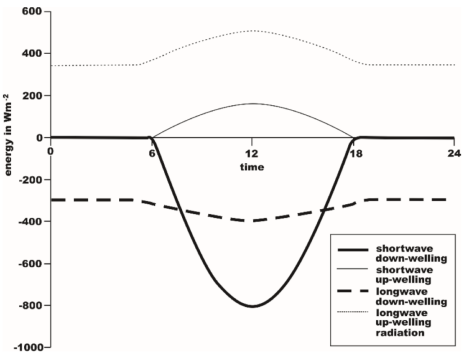

Figure 2.2: Schematic of a typical diurnal cycle for the four radiative components. Taken from Foken (2008b).

On the other hand, albedo is only 0.1 for wet, grey soil and even less for rough water at low zenith angles. Peat soils typically have an albedo of 0.05-0.15, but this depends on the soil moisture, as higher moisture content from e.g. precipitation causes lower reflectivities (Garratt, 1992, p. 121). Diurnal variability in terms of a parabolic signal is often found in the albedo on vegetative surfaces due to the solar elevation angle, with maxima near sunrise and sunset, and minima around noon (see Rosenberg et al., 1983, pp. 45-47).

The albedo can also be modified by vegetation changes. Several studies, e.g. te Beest et al. (2016), have noted the positive effect of reindeer grazing on surface reflectivity in tundra ecosystems – grazing makes the surface whiter. However, vegetation changes in the Arctic promoted by man-made climate change can create darker surfaces, and thus induce a positive feedback to global warming (Pearson et al., 2013).
As the surface absorbs the remaing shortwave radiation, it is warmed up and will emit longwave radiation by way of eq. 2.2. This irradiance is LU in eq. 2.4, and if the surface emissivity is known, LU provides a good proxy for the surface temperature (Arya, 2001, p. 46). Strictly speaking, a small fraction of the measured LU signal originates from the reflected downwelling longwave radiation, i.e.

$$LU = \epsilon\sigma T_{surf}^4 + (1 - \epsilon)LD \tag{2.6}$$

where the second term on the right hand side is the part of LD that is not absorbed by the surface (Munn, 1966, p. 17). However, finding the exact surface emissivity experimentally is difficult, and $(1 - \epsilon)LD$ is usually considered negligible.

If surface temperature estimates using LU are not completely 'waterproof', finding the temperature of the atmosphere by LD is much more complicated, because LD does not necessarily originate from one surface, but rather a whole multitude of atmospheric layers. Opaque clouds emit like black bodies, but more transparent cloud types have their own characteristic emissivities. Kuhn (1963, p. 637) found cloud emissivites ranging from 0.1 to 1, with lower values for thin clouds like cirrostratus, and higher values for stratiform clouds. Even under a thick cloud cover with $\epsilon \approx 1$, estimating the cloud-base temperature from surface-based LD measurements is problematic because the LD signal may be attenuated by infrared absorption within the boundary layer.

Regardless of the emissivity, clouds will absorb LU and limit the radiative cooling from the ground. This is why nighttime and wintertime surface temperatures are generally much lower under a clear sky than in overcast conditions. During summer days, on the other hand, clouds have a cooling effect on the surface because they reflect and absorb solar radiation. Low stratus clouds are particularly effective at depleting solar radiation (Arya, 2001, p. 33).

LD also depends on the greenhouse gas distributions in the atmosphere. Indeed, the greenhouse effect is due to the absorption of LU by certain gases, primarily water vapor and CO_2, and this absorption will warm the atmosphere and increase LD. Finally, LD increases with increasing atmospheric temperatures, but because a large part of LD comes from the free troposphere, which is not directly affected by the diurnal cycle in solar radiation, LD shows only a modest diurnal signal. LU is usally greater than LD, both day and night, but under low clouds or fog, the two longwave components can cancel each other (Foken, 2008b, p. 13). One final remark about both longwave components is that they never drop to zero, but rather settle at a few 100 W/m^2 in the night due to eq. 2.2.

2.3 Ground heat flux

The surface absorbs solar radiation during the day and warms up, whereas in the night it reemits heat back to the atmosphere as longwave radiation and cools. However, the surface communicates not only with the atmosphere, but also with deeper layers in the soil as it distributes some of the heat downwards. Heat in solid media is transported by conduction, which differs from convection in that no mass exchange is involved in conductive processes, only molecular kinetic energy along temperature gradients. Soil temperatures depend on solar heating, but the diurnal signal decays exponentially with depth, and the phase is shifted due to thermal inertia. The thermal wave propagation, amplitude decay and time shift are illustrated in Fig. 2.3.

A simular pattern unfolds on annual time scales, but the annual wave penetrates to about 10 m, rather than just $\approx$ 1 m which is typical for one day (Arya, 2001, p. 48). In addition, whereas maximum surface temperatures are found in summertime, the layer above the depth of zero annual amplitude is warmest during winter (Foken, 2008b, p. 15).

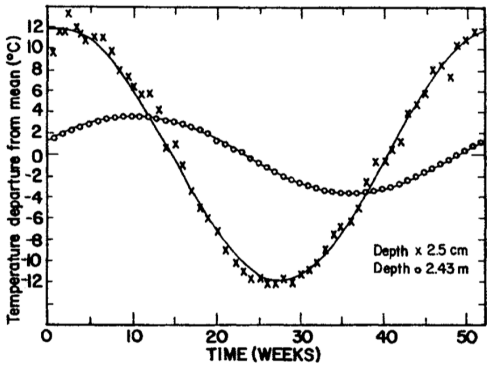

Figure 2.3: Time series of measured soil temperatures at different depths on a semi-arid site in Australia. Adopted from Arya (2001, p. 48), after West (1952).

The downward ground heat flux Q_G, i.e. the soil heat flux at the surface, is found to be proportional to the vertical temperature gradient in the soil and reads

$$Q_G = a_G \frac{\partial T}{\partial z} \tag{2.7}$$

where a_G is the thermal conductivity [W m^{-1} K^{-1}], which depends on the soil properties. It follows from eq. 2.7 that diurnal and annual waves are also found in the soil heat flux. The heat transfer equation can be solved numerically if the soil temperature profile is available. Unfortunately, contact thermometry on the surface is made very difficult by roughness and the large temperature gradients in the air and soil, which may reach 20 K/mm under strong solar heating (Arya, 2001, p. 46), (Rosenberg et al., 1983, p. 79). Thus, the in-situ signal on the surface is bound to be contaminated by air temperature fluctuations, as well as the absorption of solar radiation. Soil heat flux sensors suffer from the same problem, and should not be exposed to the air. In field-based research, the issue of the surface temperature is usually overcome by adding the soil heat flux measured in situ at a greater depth, e.g. z_d = 20 cm, to the rate of change in the ground heat storage

between z_d and the surface, in practice up to say z_u = 5 cm, such that

$$Q_G(0) = Q_G(-z_d) + \int_{-z_d}^{-z_u} \frac{\partial}{\partial t} C_S(z) T(z) dz \tag{2.8}$$

where C_S is the volumetric heat capacity [J m^{-3} K^{-1}] of the soil, i.e., the heat required to warm up one cubic meter of soil by one Kelvin. This approach is preferred over that in 2.7, because the thermal conductivity is more complicated to measure than the heat capacity (Arya, 2001, p. 52). The numerical equivalent of eq. 2.8 is

$$Q_G(0) = Q_G(-z_d) + \frac{C_S \mid \Delta z \mid [\overline{T(t_2)} - \overline{T(t_1)}]}{t_2 - t_1} \tag{2.9}$$

where the first term is the flux at a depth, and the second term represents the change in heat storage, following Foken (2008b, p. 16). Overbars indicate depth averages at a given point in time, and the heat capacity is assumed constant. Eq. 2.8 and eq. 2.9 are obtained by integrating the first law of thermodynamics – the law of energy conservation – over the soil column. If there are no heat sinks or sources within an elemental volume of thickness δz, and heat flow is confined to the vertical, this law can be expressed as

$$\frac{\partial}{\partial t}(C_S T) = \frac{\partial Q_G}{\partial z} \tag{2.10}$$

At any depth, the rate of change of the internal energy of a soil volume is equal to the vertical convergence (going downwards) of the soil heat flux. Now, if eq. 2.7 is substituted into eq. 2.10, we get Fourier's one-dimensional heat transfer equation

$$\frac{\partial T}{\partial t} = \frac{\partial}{\partial z}\left(\frac{a_G}{C_S}\frac{\partial T}{\partial z}\right) \tag{2.11}$$

assuming the heat capacity is constant in time. The ratio $\frac{a_G}{C_S} = \alpha_h$ is termed the thermal diffusivity [$m^2 s^{-1}$], and can be understood as a measure of the time it takes for temperature changes to travel (Oke, 1987, pp. 43-45). C_S and a_G strongly increase with soil moisture, because water replaces air in the soil pore space, and water has a much ($\sim$ 1000 times) higher heat capacity than air, and also a higher conductivity. The diffusivity of peat is in general low compared to other soil types, and is almost independent of soil moisture (Arya, 2001, p. 50).
Fourier's equation can be solved analytically if the soil is assumed to be homogeneous, and the temperature T(-z,t) is prescribed as a trigonometric function dampened exponentially and shifted by the depth, i.e.

$$T(-z,t) = T_m + A_s exp(\frac{-z}{d}) sin\left[\frac{2\pi}{P}(t - t_m) + \frac{-z}{d}\right] \tag{2.12}$$

where T_m is the temperature at a depth unaffected by the diurnal cycle, A_s is the thermal wave amplitude at the surface and P is the wave period, i.e. 24 hours for the diurnal case. The damping depth d = $\sqrt{P\alpha_h/\pi}$ is such that at z = d, the amplitude is reduced to 1/e or 37 % of its surface value, and t_m is the time such that T(0,t_m) = T_m

when the surface temperature is rising. The phase lag z/d is proportional to the depth, and at z = πd the wave phase is completely reversed. Eq. 2.11 can model soil temperatures over both daily and annual time scales through a homogeneous column, i.e. where the thermal diffusivity is constant in time and depth. However, this is rarely the case in a rainy environment, and moisture variability will modify the thermal diffusivity, though not much for peat soil. Furthermore, precipitation and clouds in general will break down the sinusoidal temperature pattern. We therefore propose a slightly modified version of eq. 2.11, where the dampening and time shifting are the same, but the varying surface conditions are taken into account, assuming surface temperature data is available:

$$T(-z,t) = \overline{T_{surf}} + T'_{surf}(t - \frac{12z}{\pi d}) \cdot exp(\frac{-z}{d}) \tag{2.13}$$

where $T'_{surf} = T_{surf} - \overline{T_{surf}}$ is the oscillating component of the surface temperature, and

$$t - \frac{12z}{\pi d} = t - 6 \cdot \frac{z}{d} \Big/ \frac{\pi}{2} \tag{2.14}$$

is the time delay expressed in hours. The number 6 arises because $\pi/2$ represents a quarter of a 24-h day, that is, six hours. Eq. 2.13 is not a solution of eq. 2.11, but should nevertheless provide a more realistic estimate of the soil temperature. It is assumed in both eq. 2.13 and eq. 2.12 that mean daily temperatures at the surface and at some depth are equal. This might be problematic in permafrost areas where steep temperature gradients in the soil column are found. Yet, the difference should be small for shallow levels, say z $\sim$ 0.1 m, because the damping depth for the annual wave is $\sqrt{365}$ = 19.1 times the diurnal dampening depth (Arya, 2001, pp. 53-54).

The ground heat flux is often treated as a second-order term by meteorologists (Gentine et al., 2012). Nevertheless, the instantaneous flux can be quite significant and sometimes even dominate the surface energy balance, especially during the night and under bare soil (Liebethal et al., 2005, pp. 253-254). Besides, the greatest ground heat flux is found in permafrost regions (Chapin III et al., 2011, p. 98), where heat accumulates in the soil during summer rather than simply being released again every night, which is typical in warmer ecosystems (Stull, 1988, p. 282). We must therefore expect it to play an important role in the energy balance on a sub-Arctic permafrost site such as ours.

2.4 Turbulent fluxes

2.4.1 The atmospheric surface layer

The nonradiative heat budget and the net ecosystem exchange of CO_2 on the land-air interface originate from molecular diffusion processes such as conduction, evapotranspiration and photosynthesis. However, while these mechanisms are dominant in the viscuous and molecular sublayer, which extends up to $\sim$ 0.01 m, turbulent exchange is about 10^5 more

efficient than molecular processes in the surface layer, which reaches up to 50-100 m (Foken, 2008b, pp. 7, 30).

The surface layer is the part of the boundary layer where transfer of scalars is controlled by small-scale turbulence in the form of eddies and where vertical fluxes are roughly constant with height (Oke, 1987, p. 40). It is characterised by wind shear generated by both mechanical friction at the surface, and by thermal turbulence due to buoyancy (Rosenberg et al., 1983, p. 134). The atmospheric boundary layer (ABL) is similar to the surface layer in definition, in that it is also in contact with the surface and is often recognised by a diurnal cycle (American Meteorological Society, 2018), but at higher levels ABL communicates more directly with the free atmosphere.

By analogy to the two-dimensional boundary layer in a wind tunnel, Garratt (1992, pp. 1-2) subdivides the atmospheric boundary layer into an inner and outer region, the former representing the surface layer. In the outer region of the boundary layer, with a depth of ~ 100-2000 m, influence from the surface is limited, and in the atmosphere, the Coriolis effect cannot in general be neglected. This layer is sometimes termed the Ekman layer, as the combined effects of friction and Coriolis forces give rise to the so-called Ekman spiral. In the inner layer, however, surface characteristics become very important, and effects from the earth's rotation are small.

2.4.2 Reynolds rules and stationarity

Several assumptions are necessary before we move on to generalised equation of scalar conservation. First, we introduce the *Reynolds decomposition*, which partitions scalars and wind components into their time mean and their turbulent term, i.e.

$$\zeta = \overline{\zeta} + \zeta' \tag{2.15}$$

where ζ is any such physical parameter, and $\overline{\zeta}$ is defined as

$$\overline{\zeta} = \frac{1}{T}\int_{t}^{t+T} \zeta(t)dt \tag{2.16}$$

for an averaging period T, e.g. 30 min. The Reynolds decomposition is useful because it allows for great simplification in describing turbulence statistics, owing to the Reynolds postulates as reviewed below:

$$\begin{aligned}
\overline{\zeta'} &= 0 \\
\overline{\zeta\psi} &= \overline{\zeta}\,\overline{\psi} + \overline{\zeta'\psi'} \\
\overline{\overline{\zeta}\psi} &= \overline{\zeta}\,\overline{\psi} \\
\overline{a\zeta} &= a\overline{\zeta} \\
\overline{\zeta + \psi} &= \overline{\zeta} + \overline{\psi},
\end{aligned} \tag{2.17}$$

where ψ is another time-dependent parameter, and a is a constant. Stricly speaking, the Reynolds postulates apply only to *ensemble means*, not means over time (Foken et al., 2012a, p. 63). In other words, statistical properties should be taken from a large number of

realisations under identical conditions, rather than from a limited time interval. However, such an ensemble can hardly be obtained in practice, and we have no choice but to accept time averages as the best statistics available.

Time averages are a good approximation under the condition that the turbulent fluctuations are *statistically stationary*, that is, variances and covariances must converge as the averaging period T increases. See e.g. Kaimal and Finnigan (1994, pp. 255-256) for a more thorough discussion of stationarity in turbulence. At any rate, the condition of stationarity will never be strictly met in the atmosphere, and we can at best hope for quasi-stationarity over a limited time interval (Arya, 2001, p. 150).

2.4.3 Eddy covariance

Having clarified some fundamental concepts, we now proceed to the derivation of the eddy-covariance flux. For an infinitesimal control volume dV, the conservation of scalars and momentum can be described in flux form as

$$\frac{\partial \rho_d \zeta}{\partial t} + \boldsymbol{\nabla} \cdot (\mathbf{u} \rho_d \zeta) + K_\zeta \Delta(\rho_d \zeta) = S_\zeta \tag{2.18}$$

where ρ_d is the density of dry air, ζ is any scalar or vector quantity, $\mathbf{u}$ is the wind vector, K_ζ is the molecular diffusion coefficient for ζ, S_ζ is the net source or sink, e.g. forces if ζ represents a wind component, and $\boldsymbol{\nabla}$ and Δ denote the gradient and Laplacian operators. According to eq. 2.18, the rate of change of a quantity is the sum of atmospheric transport, molecular diffusion and production by a source or absorption by a sink. In the case where ζ is unity, eq. 2.18 becomes the continuity equation

$$\frac{\partial \rho}{\partial t} + \boldsymbol{\nabla} \cdot (\mathbf{u} \rho) = \frac{D\rho}{Dt} + \rho \boldsymbol{\nabla} \cdot \mathbf{u} = 0 \tag{2.19}$$

where $\frac{D}{Dt}$ represents the Lagrangian derivative, and S = 0 because there can be no sources of dry air in the atmosphere. At this point, and without loss of generality, we substitute ζ in eq. 2.18 by the mixing ratio χ_c of an atmospheric constituent such as water vapor or CO_2. The following routine can also be used for e.g. the sensible heat flux, when ζ is instead replaced by the air enthalpy.
Neglect molecular diffusion and rewrite eq. 2.18 to obtain

$$\frac{\partial \rho_d \chi_c}{\partial t} + \boldsymbol{\nabla} \cdot (\mathbf{u} \rho_d \chi_c) = S_c \tag{2.20}$$

Now we apply the Reynolds decomposition to eq. 2.20, and average over a certain time interval:

$$\overline{\frac{\partial (\overline{\rho_d} + \rho_d')(\overline{\chi_c} + \chi_c')}{\partial t}} + \boldsymbol{\nabla} \cdot \overline{(\overline{\mathbf{u}} + \mathbf{u}')(\overline{\rho_d} + \rho_d')(\overline{\chi_c} + \chi_c')} = \overline{\overline{S_c} + S_c'} \tag{2.21}$$

The averaging time T must be large enough to detect all turbulent contributions to the flux including the larger eddies, but small enough not to violate the assumption of

stationarity, i.e. not to mistake real trends such as the diurnal cycle, for turbulent signals (Arya, 2001, p. 149). In general, the optimal T may vary depending on e.g. measurement height and atmospheric stability, but T = 30 min is accepted as a compromise between the afore-mentioned opposing effects, and will not introduce remarkable errors (Foken, 2008b, p. 106).

Following Leuning (2005), we expand eq. 2.21 and obtain

$$\overline{\rho_d}\overline{\frac{\partial \chi_c}{\partial t}} + \overline{\chi_c}\overline{\frac{\partial \rho_d}{\partial t}} + \boldsymbol{\nabla} \cdot [\overline{\chi_c}(\overline{\mathbf{u}\rho_d} + \overline{\mathbf{u}'\rho_d'}) + \overline{\rho_d}\overline{\mathbf{u}'\chi_c'} + \overline{\mathbf{u}}\overline{\rho_d'\chi_c'} + \overline{\chi_c'\mathbf{u}'\rho_d'}] = \overline{S_c} \quad (2.22)$$

All first moments such as $\overline{\overline{\mathbf{u}\rho_d}\chi_c'}$ are omitted because the mean of a fluctuation is zero. Moreover, the covariance between ρ_d and χ_c vanishes because fluctuations in density through either temperature or pressure changes do not affect the dimentionless mixing ratio [kg/kg or mol/mol]. Variations in water vapor content would affect both ρ_d and χ_c, but would have limited effect on the covariance. Likewise, the third moment $\overline{\chi_c'\mathbf{u}'\rho_d'}$ is known to be small and can be disregarded.

Unfortunately, infrared gas analyzers used in the field do not measure mixing ratios, but rather densities or molar concentrations. Such variables are in general not conserved, and will indeed change upon fluctuations in temperature and water vapor content. Density fluctuations due to variations in water vapor density and temperature may lead to erroneous flux measurements, but the WPL correction, further discussed in Section 5.2.4, takes these effects into account.

Having tossed out the two last terms on the left-hand side, and noting that $\overline{\mathbf{u}\rho_d} + \overline{\mathbf{u}'\rho_d'} = \overline{\mathbf{u}\rho_d}$, we can rewrite eq. 2.22 as

$$\overline{\rho_d}\overline{\frac{\partial \chi_c}{\partial t}} + \overline{\chi_c}[\overline{\frac{\partial \rho_d}{\partial t}} + \boldsymbol{\nabla} \cdot \overline{\mathbf{u}\rho_d}] + \overline{\mathbf{u}\rho_d} \cdot \boldsymbol{\nabla}\overline{\chi_c} + \boldsymbol{\nabla} \cdot (\overline{\rho}_d\overline{\mathbf{u}'\chi_c'}) = \overline{S_c} \quad (2.23)$$

But the terms in square brackets are recognized from eq. 2.19 as the left-hand side of the continuity equation, and must therefore vanish. Eq. 2.23 describes the budget of χ_c within an infinitesimal control volume dV. However, what we seek is a measure of the net exchange of scalars between the surface and the atmosphere. Therefore, we need to express scalar conservation in a finite volume V over an area A and with measurement height h, which is done by integration:

$$\begin{aligned}\iiint_V \overline{S_c}\, dx\, dy\, dz = \iiint_V [&\overline{\rho_d}\overline{\frac{\partial \chi_c}{\partial t}} + \overline{u\rho_d}\overline{\frac{\partial \chi_c}{\partial x}} + \overline{v\rho_d}\overline{\frac{\partial \chi_c}{\partial y}} + \overline{w\rho_d}\overline{\frac{\partial \chi_c}{\partial z}} \\ &+ \frac{\partial \overline{\rho_d}\overline{u'\chi_c'}}{\partial x} + \frac{\partial \overline{\rho_d}\overline{v'\chi_c'}}{\partial y} + \frac{\partial \overline{\rho_d}\overline{w'\chi_c'}}{\partial z}]\, dx\, dy\, dz \end{aligned} \quad (2.24)$$

We can align the cartesian coordinate system with the mean flow, so that both $\overline{v\rho_d} = 0$ and $\overline{w\rho_d} = 0$. Physically, this corresponds almost to $\overline{v} = \overline{w} = 0$ (Leuning, 2005), and the algorithm for this coordinate rotation is detailed in Section 5.2.1 Now, two simplifying steps follow. First, the eddy flux divergence as given in the second line of

eq. 2.24, is usually much greater in the vertical than the horizontal. In fact, assuming *horizontal homogeneity* in the layer underneath the measurement system, we can disregard all horizontal gradients, including the advection terms, as well as the integration over A. Over a homogeneous surface, the spatial mean for large averaging distances L or areas, sampled at one horizontal position, approaches the true mean of the whole surface (Arya, 2001, p. 159).

The keen reader might notice that stationarity, which we discussed earlier in this section, and homogeneity seem like two sides of the same coin. In fact, stationarity and homogeneity are indeed related by the so-called *ergodic principle*, which states that the statistics of stationary and homogeneous variables converge to the ensemble mean as T and L increase (Wyngaard, 2010, p. 35). Specifically, if the ergodic principle holds, a time average measured by one mast approaches the true horizontal average over a larger domain, e.g. an ecosystem. However, as with stationarity, homogeneity is a luxury that does not apply to most surfaces – it is even more difficult to satisfy in the atmosphere than stationarity – and in field applications we will have to cope with quasi-homogeneous surfaces or worse (Arya, 2001, p. 150).

The second approximation we make is to assume steady-state conditions, where $\frac{\partial}{\partial t} = 0$. Then the volume integral reduces to

$$\int_0^h \overline{S_c}\, dz = \int_0^h \frac{\partial \overline{\rho_d}\overline{w'\chi_c'}}{\partial z}\, dz \tag{2.25}$$

Solving the integral, we obtain

$$\overline{\rho_d}\overline{w'\chi_c'}|_h - \overline{\rho_d}\overline{w'\chi_c'}|_0 =< \overline{S_c} > \tag{2.26}$$

where $< \overline{S_c} >$ is the height integral $\int_0^h \overline{S_c}\, dz$ of the source between the ground and the measurement height h. We arrive at the final result when noting that the wind is identically 0 at the surface, so that

$$\overline{w'\chi_c'}|_h = F_c \tag{2.27}$$

where $F_c = \frac{<\overline{S_c}>}{\overline{\rho_d}}$ is the average source in the entire control colume V, divided by dry air density. Eq. 2.27 is the cornerstone of all eddy-flux measurements, because it suggests that the atmosphere-surface exchange of a constituent c can be determined by quantifying the covariance between c and the vertical wind. The fluxes of sensible (SH) and latent heat (LH) and CO_2 (NEE) are then given by

$$\begin{aligned} SH &= c_p \overline{\rho_d}\overline{w'T'} \\ LH &= L\overline{w'q'} \\ NEE &= \overline{w'c'} \end{aligned} \tag{2.28}$$

where c_p is the specific heat of air, L is the latent heat of water evaporation, T is the air temperature, and q and c are the molar densities of water vapor and CO_2, respectively.

2.4.4 Turbulence spectrum

The turbulence spectrum is the energy distribution associated with the range of turbulent eddy wavelengths (Foken, 2008b, p. 19). Eddies are thought to have three-dimensional extent, but can be compared to whirls in common terminology (Arya, 2001, p. 155). Since turbulent eddies are what we measure using the eddy covariance method, a little background on the turbulent spectrum is needed. The energy spectrum of interest to the micrometeorologist spans a time range from about 50 ms to 30 min, or a frequency range between roughly 10^{-4} Hz and 20 Hz.

Within this spectrum, three subranges stand out. The range of production is where the mean flow interacts with the boundary layer, generating the largest, energy-containing eddies. These eddies are typically of size l, which is proportional and roughly equal to some characteristic flow dimension, e.g., the pipe diameter for flow in a pipe, or the boundary layer height for flow in the atmospheric boundary layer (Wyngaard, 2010). The smallest eddies are found in the dissipative range and vary in size from a few mm to ~ 1 cm. Dissipation is a viscuous process, which depends on the viscosity coefficient v. In this range, the eddies are transformed to heat and bring the turbulence spectrum to an end.

The Russian scientist Kolmogorov argued that, in the dissipative range, the turbulence statistics such as means and covariances are isotropic, i.e. the smallest eddies have lost all information on the background flow (Wyngaard, 2010, pp. 153-154). This suggests that universal velocity and length scales in the dissipation range can be derived by simple dimensional arguments, depending only on two basic fluid properties: the energy dissipation rate ϵ and the kinematic viscosity v. The dissipation length scale η is the only combination of v and ϵ that yields a length [m], and reads

$$\eta = \left(\frac{\nu^3}{\epsilon}\right)^{1/4} \tag{2.29}$$

which is about 10^{-3} m in a convective boundary layer in the atmosphere.

Eddies much smaller than the boundary layer depth, but much larger than 1 mm, are found in the inertial subrange. The inertial subrange is particularly important to micrometeorologists (Foken, 2008b, p. 20), because its eddies are also isotropic, and can be measured directly by an eddy-covariance system.

An important feature of the turbulence spectrum is that the three subranges transfer the same amount of energy. If suddenly the synoptic wind is intensified, this signal will reach first the production range and generate large eddies, then these eddies will break down and enter the inertial subrange, and finally, the small eddies will crumble by viscuous forces in the dissipative range and turn into heat.

2.5 Carbon cycle

The terrestrial carbon cycle is divided into two processes: photosynthetic CO_2 uptake and respiratory CO_2 release. These two processes are not balanced like the surface energy budget – one can be greater than the other on short and often long time scales. Nevertheless, the (nonzero) difference between carbon gain and carbon loss, referred to

as the balance (Chapin III et al., 2011, p. 123), is what controls the carbon distribution between land, atmosphere and ocean, and between ecosystems.

2.5.1 Photosynthesis

Photosynthesis is the process by which plants consume solar radiation and water, to reduce inorganic carbon dioxide CO_2 from the atmosphere into organic molecules, i.e. primary sugars. Oxygen (O_2) is released back to the atmosphere as a waste product, whereas the sugar molecules are kept by the plant (Chapin III et al., 2011, p. 126). The net photosynthetic reaction is

$$CO_2 + H_2O -> CH_2O + O_2 \tag{2.30}$$

following (Schlesinger, 1991, p. 109). Through photosynthesis, plants gain the material to grow and develop storage organs such as leaves, stems and fruits.
Even though photosynthesis is what drives most biological processes in ecosystems (Chapin III et al., 2011, p. 123), the radiation used for photosynthesis represents only a negligible component of the surface energy balance – under certain conditions up to about 8 % of the incoming solar radiation is consumed, but on average this fraction is less than 1 % (Munn, 1966, p. 30). This is partly because the radiation available to plant capture is confined to the visible region, which represents only about 40 % of incoming solar radiation, and because leaves reach light saturation long before the time of full sunlight intensity around noon.

Important controls of photosynthesis are e.g. the supply of atmospheric CO_2, light, water and nutrients, as well as air temperature. The **CO_2** enters plants by *diffusion*, i.e. transport along gradients, through small pores on the leaf surface called stomata. However, as CO_2 is gained through these pores, so is **water** lost by transpiration. Since both water and CO_2 are needed in photosynthesis, plants encounter a tradeoff between CO_2 absorption and water evaporation. Depending on the environmental resources available, plants will regulate the stomata size to maximize photosynthesis and limit water loss. Owing to the 35 % increase in atmospheric CO_2

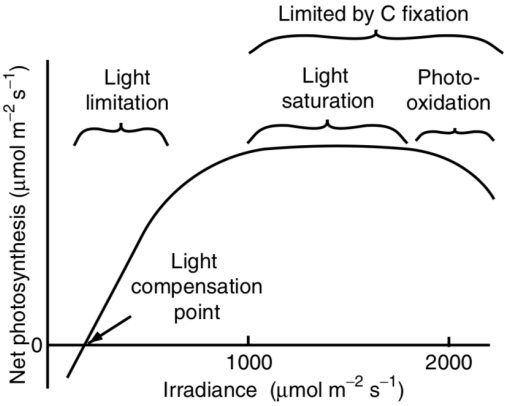

Figure 2.4: Light response curve for a typical plant. The point of light saturation depends on plant and environment, but the linear slope before saturation is similar among most plants. Adopted from Chapin III et al. (2011, p. 128).

concentration since the beginning of the industrial age, the photosynthetic production has increased on a global scale. This is called the CO_2 fertilization effect. However, atmospheric CO_2 is so well mixed that it cannot explain much of the regional variation in photosynthesis.

On the other hand, **light intensity** can vary by a factor of 1000 due to e.g. cloud cover and changes in the solar angle, as well as canopy cover and structure. Light supply controls the cycles of photosynthesis on diurnal, seasonal, and sometimes interannual time scales, after e.g. volcanic eruptions, but does also not in general explain the spatial variability in carbon uptake found across regions. Regions of very high light, such as arid grasslands and deserts, are often affected by other environmental limitations such as water stress. As illustrated in fig. 2.4, photosynthesis is proportional to light intensity, but only up to a certain saturation point. When integrated over a canopy, the point of light saturation is elevated due to e.g. shading of sub-canopy leaves (Rosenberg et al., 1983, p. 289), but plant communities also experience light saturation.

Closely related to light availability, but different in several respects, is the control of **temperature** on photosynthesis. Unfavourable temperatures, high as well as low, will limit carbon uptake either by lowering the chemical reaction rate or causing enzyme inactivation and pigment destruction. Temperature extremes can greatly disrupt plant functions and are in many cases more adverse to photosynthesis than the average temperature. The plants that do grow in regions with extreme temperatures, such as in high-latitude ecosystems, cope with the environmental stress in different ways: Annual plants die, deciduous plants shed their leaves and some evergreen plants become dormant. For these reasons, there is little carbon uptake during the cold season at high latitudes.

Soil nutrients – nitrogen compounds in particular – do not take direct part in the photosynthesis reaction, but are required in the production of photosynthetic enzymes. Even though atmospheric nitrogen is abundant in its molecular form, it needs to be assimilated into ecosystems before plants can make use of it. Nitrogen therefefore exerts a strong control on the photosynthetic capacity.

Moreover, the rate of photosynthesis at any solar irradiance level is known to increase under high **winds**, as shown by e.g. Baldocchi et al. (1981). This is because turbulent mixing of the air will enhance the temperature and CO_2 gradients from the leaf surface to the atmosphere, thus strengthening the diffusion of CO_2, and also in part because the mechanical distortion of canopies will enable light to reach to the lower, otherwise shaded leaves (Rosenberg et al., 1983, pp. 298-299).

Finally, an important effect in high latitudes is the **snow cover**. A snow pack protects plants from low wintertime temperatures and also provides water supply, particularly in springtime (Callaghan et al., 2005). On the other hand, late snowfall inhibits spring thawing and cools the soil, which can limit plant growth (Scott and Rouse, 1995).

On an ecosystem scale, photosynthesis is termed *gross primary production* (GPP) and depends on the integrated effects of the environmental factors listed above. Differences in GPP across ecosystems are largely due to the length of the growing season and the wintertime environment.

2.5.2 Respiration

Respiration can be thought of as the inverse of photosynthesis (Rosenberg et al., 1983, p. 288). It involves the oxidation of organic carbon molecules from photosynthesis and the release of CO_2, water and energy, but the chemical processes of respiration – and the governing environmental factors – are different from photosynthesis.

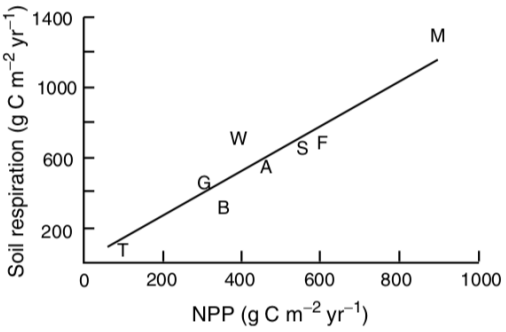

Figure 2.5: Respiration is closely related to photosynthesis across biomes such as tundra (T), boreal forest and woodland (B) and so on. Taken from Chapin III et al. (2011, p. 206).

Microbial respiration is the release of CO_2 associated with the decomposition of live and dead organic material by microbes. Plant respiration is the carbon release by mitochondria, and is an essential process for plant growth and maintenance. Both plant respiration and microbial respiration depend strongly on photosynthesis, because the carbon input dictates the amount of available organic matter for decomposition and oxidation.

However, respiration does not require light and can continue during the night. Moreover, respiration can occur in colder environments than plant growth, and microbial respiration has been reported at soil temperatures down to –10 °C (Mikan et al., 2002). Even the Arctic winter supports respiration – estimates of the wintertime contribution to total annual CO_2 losses by respiration in Arctic and boreal ecosystems range from 15 % to 50 % (Grogan and Jonasson, 2006). Yet, increases in temperature do cause elevated respiration rates in the short term by e.g. stimulating the microbial enzyme activity. This effect is constrained on diurnal to seasonal and longer time scales by various factors, but is nonetheless expected to cause a significant carbon release as warming continues in cold environments (Schuur et al., 2015). The relationship between temperature and tundra soil respiration is exponential up to a certain point, as illustrated in Fig. 2.6

The second environmental control of respiration is moisture supply. Like photosynthesis, respiration increases with increasing moisture, as long as enough oxygen is available. If soil moisture exceeds 100-150 % of the dry soil mass, on the other hand, decomposition is inhibited by the slow oxygen diffusion rate in water compared to air. Anaerobic conditions would also limit plant growth, but to a lesser extent. Thus, organic carbon tends to accumulate in wetlands, even at high latitudes where photosynthetic activity is low. In fact, wet soils at all latitudes have been a net carbon sink for thousands of years and contain about a third of Earth's soil organic matter (Chapin III et al., 2011, p. 204). The decomposition that does take place in wetlands can release trace gases such as methane and nitrous oxide, which have a much greater heat trapping capacity per molecule than

CO_2. However, because methane is an excellent energy source if there is oxygen present, it is often consumed by bacteria as it diffuses through the soil column, thus not reaching the atmosphere. Incubation experiments, i.e. studies of soil samples under controlled conditions, indicate that CO_2 will dominate the permafrost carbon feedback even when the different warming potentials are taken into account (Schädel et al., 2016; Lee et al., 2011).

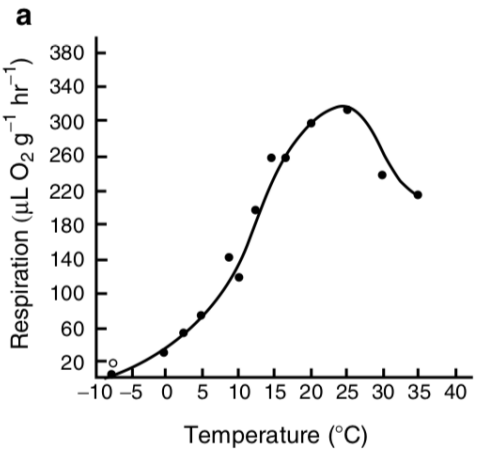

Figure 2.6: Response of tundra soil respiration to temperature changes, from laboratory incubations. Taken from Chapin III et al. (2011, p. 201).

The sum of all CO_2 respiration from plants and microbes over an ecosystem is called ecosystem respiration, R_{eco}. Subtracting R_{eco} from GPP, we obtain the net ecosystem production NEP:

$$NEP = GPP - R_{eco} \quad (2.31)$$

where GPP and R_{eco} are inorganic carbon fluxes. NEP represents the approximated net carbon uptake by an ecosystem. In the absence of large disturbances such as wildfires, average NEP over days or weeks is small because GPP and R_{eco} are similar in magnitude. The instantaneous NEP, however, is rarely balanced. At daytime, GPP is greater than R_{eco}, and vice versa during the night. A similar cycle is observed on an annual time scale, with positive NEP during the growing season and negative NEP during seasons unfavourable for photosynthesis. On the other hand, the integrated NEP over a full year is not necessarily 0 – in fact, model estimates indicate that the terrestrial biosphere as a whole has been a net carbon sink in most of the years since 1960 (Le Quéré et al., 2009).

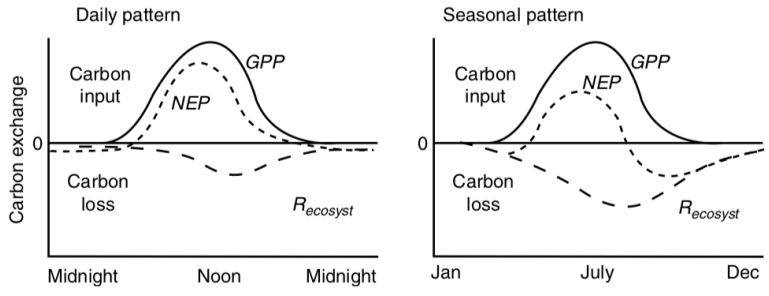

Figure 2.7: Idealized diurnal and seasonal patterns of NEP, GPP and R_{eco}, where positive signs indicate carbon uptake. After Chapin III et al. (2011, p. 209).

NEP is not restricted to atmospheric fluxes, because some of the CO_2 from microbial respiration is dissolved as it meets soil water and does not reach the atmosphere. Nonetheless, NEP is insufficient to describe the full net carbon budget for an ecosystem. Fluxes of for instance dissolved organic carbon and particulate matter through streams and winds, as well as non-CO_2 gas fluxes and wildfire emissions, also contribute to the net carbon accumulation rate (Chapin III et al., 2006). However, if the ecosystem hasn't recently been disturbed by e.g. droughts and wildfires, NEP incorporates the most important contributions to the net carbon budget.

But measuring NEP directly from eq. 2.31 is made very difficult by the fact that stimuli for GPP, such as increases in temperature or moisture, also tend to enhance R_{eco}. So while the individual terms in NEP may be large, their imbalance is usually small and hard to assess accurately. Fortunately, NEP can be closely approximated by another quantity which we touched upon in Section 2.4, namely the net ecosystem exchange of CO_2, or simply the NEE. NEE is defined as the lateral and vertical net CO_2 flux from the ecosystem of interest to the atmosphere, and is by convention positive whenever CO_2 is released to the atmosphere, and negative when CO_2 is absorbed by the ecosystem.

[-NEE] differs from NEP in that non-atmospheric sinks and sources of inorganic carbon, which would contribute to GPP or R_{eco} and thus NEP, are not incorporated in NEE. Furthermore, since NEE is usually measured by an eddy-covariance system at a certain height, e.g. a few m, there is a risk that the CO_2 flux as recorded by the sensors departs from the true NEE, that is the net rate of change in CO_2 within the box of atmosphere. Such isses could arise for instance when the assumption of stationarity or horizontal homogeneity is not met, which could introduce advection to the true carbon budget. Advection is not limited to the night, but when turbulent – i.e. non-advective – mixing is impeded by negative buoyancy associated with a stable stratication, it becomes more important. This effect often leads to underestimated nighttime CO_2 fluxes (Aubinet et al., 2012). Laurila et al. (2012) argue that issues related to advection are negligible in mire landscapes, since mires are found primarily on flat terrain. However, even seemingly level landscapes are often gently undulating (Munn, 1966, p. 189), which could introduce some gravity-driven circulation to mires. Fortunately, some of the CO_2 released under stable stratification will often accumulate beneath the flux tower, and is expected simply to be measured at a later stage when turbulence is reinitiated (Aubinet et al., 2012), or to be incorporated in the storage term, which can included in eddy-covariance calculations (Mauder and Foken, 2015).

Despite the above mentioned limitations, NEE provides a reasonable estimate for the geographic distributions of NEP, which is close to the net carbon budget in steady-state ecosystems (Chapin III et al., 2011, pp. 208, 227).

2.6 Thermal regimes in permafrost

The boundary between continuous and discontinuous permafrost does not necessarily parallel mean annual air isotherms (Washburn, 1973, p. 21). However, it seems that the critical mean annual air temperature (MAAT) for continuous permafrost lies between –6 and –8 °C, even though discontinuous permafrost has been observed at MAATs lower than

–9 °C (Washburn, 1973, p. 21). Relict permafrost, i.e. permafrost that is in disequilibrium with the present climate, has been found in e.g. Alaska and Norway in areas of positive MAAT (Brown and Péwé, 1973; Gisnås, 2011), but in general the southern limit of discontinuous permafrost roughly corresponds to the –1 °C isotherm (Brown, 1967).

From the observations listed above, it is clear that the mean annual ground temperature (MAGT) may depart significantly from MAAT. Environmental factors such as vegetation, soil type and hydrological and geological conditions can all modify the permafrost extent as predicted by MAAT alone (Osterkamp and Burn, 2015). The presence of snow cover is a particularly important variable, because a wintertime snow pack will protect the ground from very cold air (Wallace and Hobbs, 2006, p. 35). This effect explains why MAGTs are usually 2 °C to 4 °C higher than MAAT. Indeed, the absence of seasonal snow cover is critical for permafrost formation in the discontinuous permafrost region, because here MAATs are close to the melting point (Zhang, 2005).

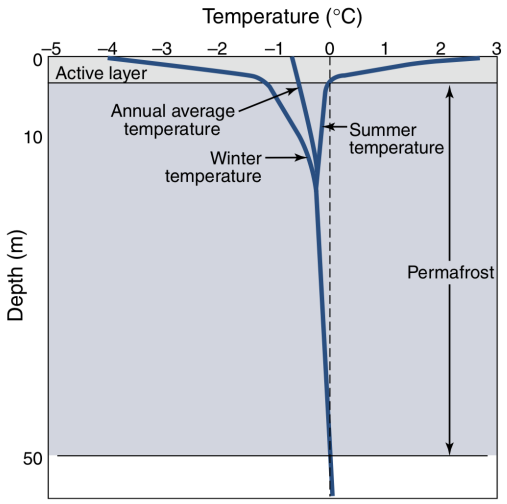

Figure 2.8: Typical annual course of the vertical temperature profile in a permafrost region. The active layer thaws and freezes on a seasonal basis, whereas the deeper ground is frozen throughout the year. The geothermal gradient provides heating from the Earth's interior and limits the depth of the permafrost layer. Adopted from Wallace and Hobbs (2006, p. 35).

However, the local net effect of snow on the ground thermal regime may be difficult to assess, owing to the distinct physical properties of snow compared to other ground material (Zhang, 2005): On the one hand, snow is a poor thermal conductor, which insulates the ground during winter. Furthermore, snow is an excellent absorber of longwave radiation – this too would limit wintertime cooling. On the other hand, snow has a high albedo and emissivity, as discussed in Section 2.2, which would both act to cool the surface. Another cooling factor is the latent heat required to melt snow: a late snowfall will typically have a cooling effect, as it delays springtime thawing of the ground.

The timing of snowmelt plays an important role in the surface energy balance of Arctic and alpine areas, because it represents an abrupt change in surface characteristics – in particular a strong decrease in the albedo, which leads to an increase in absorbed radiation (e.g. Westermann et al., 2009; Cline, 1997). At any rate, local differences in wind are the primary control of snow cover, and will largely dictate the permafrost distribution near

the southern fringe of the discontinuous permafrost region (Åhman, 1977, p. 14).

The effect of peat soil and moss is quite different: Since dry peat and moss are poor thermal conductors, they will limit summertime warming of the ground. But as they are water saturated by autumn rain, conductivity increases, especially when the water freezes, which will promote wintertime cooling (Osterkamp and Burn, 2015). The annual cycle in peat conductivity can in part explain why peatlands are so common in some discontinous permafrost areas, but we should keep in mind that peak rainfall often occurs not during autumn but during summer, at least in the interior of Finnmark, which would undermine this argument. It is in fact accepted that summertime precipitation over peatlands can cause deep permafrost thaw (Seppälä, 2011).

Permafrost depth ranges from up to 1500 m in northern Siberia and 740 m in northern Alaska, to ~ 50 m or less in the Nordic area (Péwé, 2018; Christiansen et al., 2010), generally decreasing towards warmer regions. A schematic of the annual temperature cycle in a permafrost layer is given in Fig. 2.8. No matter the vertical extent, permafrost is capped by a layer that freezes and thaws seasonally – the *active layer*. The active layer depth in summer depends on air temperatures and ground thermal properties such as latent heat, and ranges from about 20 cm to 1-2 m in soils, but can exceed 10 m in dry materials, that is, bedrock, sand or gravel (Osterkamp and Burn, 2015; Christiansen et al., 2010). The active layer is where nearly all biological activity below ground occurs, and is the medium that exchanges heat and gas with the atmosphere (Osterkamp and Burn, 2015).

Chapter 3

Study area

3.1 The Finnmark plateau

Our station was located on Finnmarksvidda in northern Norway. Finnmarksvidda is a 22,000 km^2 plateau in the county of Finnmark, located at the northeastern corner of Norway and bordering Finland and Russia. A map of Finnmark's position in Northern Europe and a more detailed map of Finnmark with our site indicated, are shown in Fig. 3.1. Finnmark (69 °N) is situated well within the Arctic circle, but has a milder climate than areas at the same latitudes in Russia and North America. Indeed, the wintertime temperatures in the interior of Finnmark are similar to those of big Canadian cities such as Winnipeg, located 20° further south (Government of Canada, 2018). Furthermore, in 1881, when the Arctic sea ice extended to the southern coast of Iceland and covered most of the Barents Sea, the waters near Finnmark remained open (Blindheim and Østerhus, 2005, p. 33), even though several ice bergs were observed from land (Furseth, 2011, p. 21). The relatively temperate climate on the coast is due to the Norwegian current, which is connected to the Gulf Stream and brings warm water from the subtropics. However, when compared to the rest of Norway, Finnmark appears to have the most harsh climate of all the Norwegian counties. Westerly winds prevail in the free atmosphere above Finnmark, but the inland is sheltered by the mountains at the western and northwestern coast (Dannevig, 2009). The influence of the ocean on the plateau climate is therefore limited, resulting in impressive seasonal temperature differences. During the winter, temperatures are frequently the lowest in Europe, occasionally dropping to less than –40 °C. What is perhaps more surprising is the summertime temperatures, which are often the highest in Norway, but also sometimes in Europe.[1] These extremes are generally reported at the same stations, located in valleys running through the interior or simply at local troughs on the plateau, such as Karasjok and Sihččajávri. The cold extremes during the polar night are associated with strong inversions, as the cold air drifts downslope and accumulates in low terrain. In the absence of strong synoptic activity, temperatures

[1] On 31 May 2013, the Finnmark town of Karasjok was in fact the warmest place in Europe, at 34 °C (Kirkebøen, 2013). Higher temperatures were found in Turkey, but then on the Asian side.

will drop to less than –30 °C on such sites, but tend to stay above –15 °C at high points on the plateau. Despite extreme winter temperatures in the inlands, the only town in mainland Norway (and Europe) with a true polar climate, according to Köppen's classification scheme (Encyclopædia Britannica, 2018), is Vardø, located on the eastern coast of Finnmark (Pedersen, 2013).[2] The mean annual air temperature ranges from up to +4 °C at the Finnmark coast to –3 °C on the plateau. On a seasonal time scale, mean air temperatures on the plateau are around +11 °C in summertime, but negative in the other seasons and ≈ –15 °C in wintertime (see Vikhamar-Schuler et al., 2010, Fig. 24).

Figure 3.1: a) Finnmark's position in northern Europe, and b) map of Finnmark with the study area indicated by an arrow. Sources: d-maps.com and Kartverket/KF-arkiv.

Annual precipitation is up to 1000 mm in the coastal areas, but only 300 to 500 mm on the plateau, which is in the rainshadow of the mountains to the west. Precipitation in the interior is very low during winter and spring, typically less than 20 mm per month. This might explain why Finnmark, the largest of all the Norwegian counties, only produces 1% of the total hydropower (Vinjar and Askheim, 2017). The 1971-2000 climatological mean number of days with dry snow is between 100 and 200 per year for the vast majority of the Finnmark plateau (NVE, 2018), but probably closer to 200 in the Karasjok area

[2]Köppen (1936, p. 16) defines polar climate according to the highest mean monthly surface temperature, which must be lower than +10 °C.

since negative temperatures are dominant from mid-October to late April (yr.no, 2018b). Average maximum snow depth generally decreases from up to several meters near the coast to less than 50 cm in the interior, but it appears that some orographic precipitation is triggered by the mountains on the plateau such as Iškoras, which leads to a thicker snow pack.

Biogeographically, Finnmarksvidda belongs to the Euro-Siberian coniferous forest biome, the *taiga*, which spans the whole Eurasian continent from the Pacific Ocean through Siberia and Northern Russia to the Atlantic Ocean. The world's northenmost pine forest is found in Stabbursdalen, at the northern edge of the plateau. Most of Finnmarksvidda, however, is covered not by coniferous forest but rather by sparse mountain birch forest, as well as bog, with treeless tundra vegetation being the exception (Gjærevoll, 1978, p. 7).

Finnmarksvidda is more vegetated than other important plateaus in Norway, e.g. Hardangervidda, which are bare and consist primarily of wide, open hills. The bogs are abundant, and though they may seem uninteresting to a geoscientist, they should certainly attract the biologist, given the massive mosquito swarms which indicate high productivity in the brief growing season.

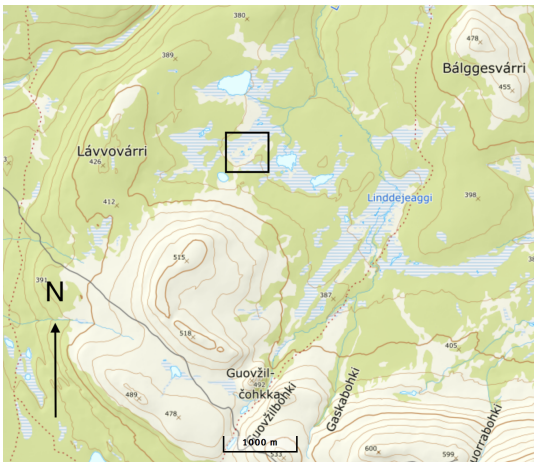

Figure 3.2: Map of the local terrain, with our field site indicated by a black square. Source: norgeskart.no.

One particular type of bogs found on Finnmarksvidda is the palsa mire, which was introduced in Section 1.1.3. Palsa mires are the dominating ecosystems in the permafrost areas on Finnmarksvidda, which occupy about 20 % of the Finnmark land surface.

3.2 Field site

Our station was located at the interior of a slighlty elevated peat surface on Finnmarksvidda, 20 km south of the village of Karasjok (69°34'N 25°30'E, elevation 358 m.a.s.l). The field site is a palsa mire of size ≈ 250 m x 200 m, surrounded by mountain birch forest and wetlands in a gently wavy terrain. A topographic map of the site and its surroundings is given in Fig. 3.2, indicating that our station was on quite level terrain. The wetlands including the palsa mire are at the bottom of a shallow depression enclosed by several small hills such as Lávvovárri 2 km to the west (426 m.a.s.l.) and Bálggesvárri (478 m.a.s.l.) 4 km to the northeast, as well as a larger mountain ridge reviewed in the next paragraph. The tree line goes at 400-450 m, and trees do cover large parts of the wetlands,

but the palsa mire is treeless. The site contains numerous thaw ponds ranging from a few m to around 30 m in diameter, possibly associated with the larger lakes outside of the palsa mire. These lakes are > 100 m wide and are connected to creeks which run down to the Kárášjohka river about 15 km north.

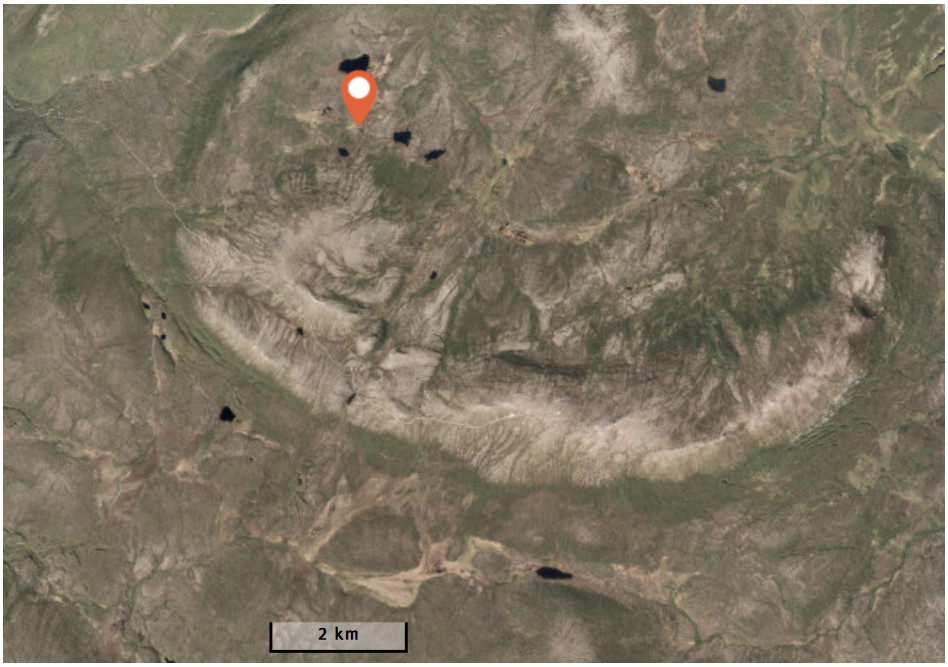

Figure 3.3: Satellite image of the Iškoras mountain which surrounds the southern sector of the field site, indicated by a marker. Source: norgeskart.no.

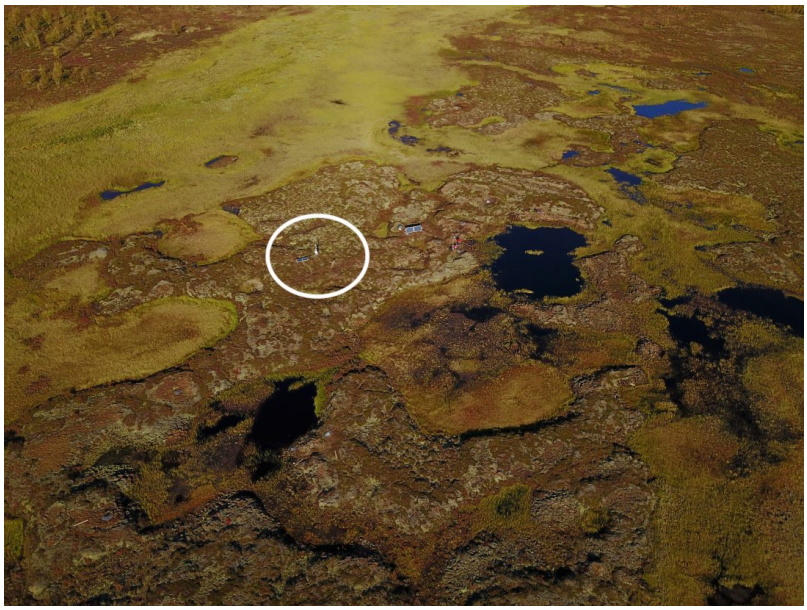

Figure 3.4: Drone image of the field site, with our station indicated in white. Source: Sebastian Westermann, University of Oslo.

The most notable feature of the local landscape is the Iškoras mountain, a 10 km long banana-shaped ridge a few km to the south of our station, seen Fig. 3.3. Iškoras is the highest point within a radius of 65 km and has its main summit at 644 m.a.s.l., which is around 300 meters above the surrounding terrain. At its western edge Iškoras peaks at 518 m.

Important plant species are low heath shrubs such as wild rosemary and dwarf birch. Between the shrubs, there are patches of exposed peat underlying a thin layer of lichens, whereas the thaw ponds are vegetated by short grass and moss. Heterogeneity on the site is in part due to vegetation, but perhaps more importantly to the surface relief, with height differences of up to 1 m within short distances. A drone image of the field site is shown in Fig. 3.4, and Fig. 4.1 in the next chapter gives some impression of the vegetation and surface roughness.

Chapter 4

Measurements

4.1 Campaign

Our campaign lasted from 7 July and 10 September 2017, but due to some malfunction in the data logger, no data was recorded after 6 August. The peat and bogs on the site are sensitive to pressure changes from trespassing people, and to minimize such disturbances we built a simple boardwalk across the palsa mire for carrying equipment to the station. We placed all instruments at the center of a dry peat surface, aiming to measure the ecosystem-scale exchange of CO_2 and energy between the palsa mire and the air. The instrument set-up is shown in Fig. 4.1.

We employed four different instruments for our study: one Campbell CSAT3 sonic anemometer (sonic), one Li-Cor LI-7500 open-path infrared gas analyzer (IRGA), one Kipp & Zonen CNR 1 net radiometer and two Hukseflux HFP01 soil heat flux plates. The eddy-covariance (EC) system, consisting of the sonic and the IRGA, measured fluxes of CO_2, sensible heat and latent heat. We fastened the sonic to a horizontal boom oriented towards the north, its center being 2.12 m above the ground, and levelled it to within $\approx \pm 1^\circ$ uncertainty. The IRGA was fastened to a lower boom, but mounted at the same height as the CSAT3, and at about 15 cm to the south of the anemometer. We tilted the IRGA by 10° to limit issues from precipitation and dew formation.

The net radiometer, which measures all four radiative fluxes reviewed in Section 2.2, was installed about 5 m away from the flux tower, pointing to the south and mounted on a tripod at a 1.0 m height, carefully but not perfectly levelled. Finally, we installed the heat flux plates by cutting out a block of soil, inserting the plates at the side of the exposed soil at 10 cm and 20 cm, and putting the block back again. Active layer depth was not monitored during the campaign, but both soil heat flux plates were placed in thawed soil, about 1.5 m from the EC system. The combination of these four instruments allowed us to estimate the surface energy balance throughout the measurement period. All instruments were connected to a Campbell CR5000 datalogger, which records turbulent data at frequency f = 20 Hz and slow fluxes at f^{-1} = 1 minute. The datalogger and the

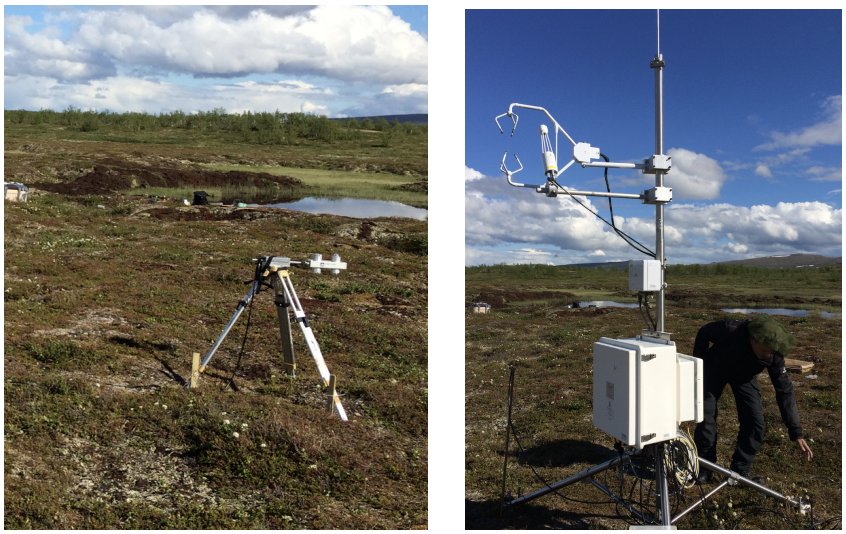

(a) (b)

Figure 4.1: a) Net radiometer mounted on a tripod, facing south. b) Set-up of the eddy covariance system, facing north. Palsas and thaw ponds are seen in the background.

instruments were powered by two solar panels.

4.2 Instrumentation

4.2.1 Sonic anemometer

The CSAT3 is an ultrasonic anemometer that measures the three-dimensional wind speed and the sonic temperature, which is applied in eddy flux calculations. The instrument, as illustrated in in Fig. 4.2, consists of three pairs of non-orthogonal transducers, each transmitting and receiving ultrasonic signals at a high frequency. Because the distance between the transducers is known, the flight time is used to calculate the wind speed along the three axes, as well as the sonic temperature in the measurement cell.

The flight time for a pulse between two transducers is a function of the speed of sound c, which is independent of the wind but varies with air density, and the wind speed u_a along the non-orthogonal axis. Following Campbell Scientific (2012), this relation is expressed as

$$t_o = \frac{d}{c + u_a} \tag{4.1}$$

for the first signal, going out, and similarly, for the second signal going back:

$$t_b = \frac{d}{c - u_a} \tag{4.2}$$

where t_o is the flight time out, t_b the flight time back, and d is the known distance between two corresponding sensors, for CSAT3 11.55 cm. Wind components perpendicular to the optical paths will affect the measured speed of sound, but this is corrected for by the CSAT3 firmware. Now it only takes a coordinate transformation to get the three orthogonal wind components in x, y and z directions.

The speed of sound c varies, but because it is equal for the two pulses, we can combine the two relations and solve for u_a:

$$u_a = \frac{d}{2}\left(\frac{1}{t_o} - \frac{1}{t_b}\right) \tag{4.3}$$

For flux calculations we are also interested in the air temperature, which is related to the speed of sound c. We find c by inverting Eq. 4.1 and Eq. 4.2 and adding them together:

$$c = \frac{d}{2}\left(\frac{1}{t_o} + \frac{1}{t_b}\right) \tag{4.4}$$

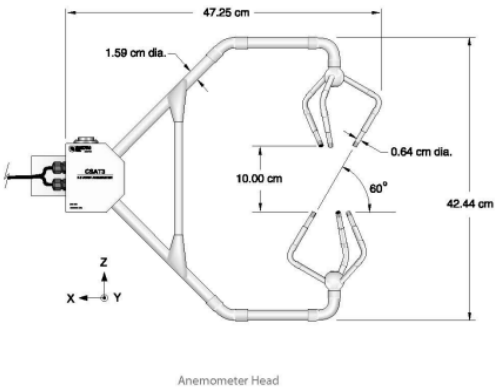

Figure 4.2: Schematic of the CSAT3 non-orthogonal sonic anemometer. Adopted from Campbell Scientific (2012).

The speed of sound through any medium depends on the density of that medium, which for air is a function of temperature and humidity, if pressure variations are small. This relationship can be expressed as follows:

$$c^2 = \frac{\gamma p}{\rho} = \gamma R_d T_v \tag{4.5}$$

where γ is the ratio of specific heat of moist air at constant pressure, c_p, to that at constant volume, c_v, p is pressure, ρ is air density, and R_d is the dry air gas constant. The final factor T_v is called virtual temperature, the temperature a dry air parcel would need in order to have same density and pressure as a moist air parcel. The virtual temperature is defined as $T_v = T(1 + 0.38\frac{e}{p})$, where e and p denote water vapour pressure and total air pressure, respectively, and it is therefore always greater than the actual temperature. Dry air is heavier than moist air, all else equal, hence it must be warmed up to reach the same density.

Because moisture can vary, it is convenient to replace γ in Eq. 4.5 by γ_d, the ratio of specific heats for dry air. It can be shown that

$$c^2 = \gamma_d R_d T(1 + 0.51q) \tag{4.6}$$

where T is the actual air temperature, and q is the specific humidity [g/kg]. Following Kaimal and Gaynor (1991), we now define the sonic temperature $T_s = T\left(1 + 0.32\frac{e}{p}\right)$. It follows that, since $q \approx 0.622\frac{e}{p}$,

$$c^2 = \gamma_d R_d T_s \tag{4.7}$$

or

$$T_s = \frac{c^2}{\gamma_d R_d} \tag{4.8}$$

which gives the sonic temperature in Kelvin. The sonic temperature T_s differs from the true air temperature by 1-2 % (Rebmann et al., 2012), but is very similar to the virtual temperature. However, it is good practice in micrometeorology to keep this distinction (Kaimal and Gaynor, 1991).

Sonic anemometers can operate during precipitation, but whenever the transducer faces are sufficiently obscured, e.g. if rain, snow or dew puddles on the lower transducers or hangs down from the upper ones, they will stop measuring until the face is cleared. In our campaign we employed wicks on the transducers, which speed up the water removal and hence mitigate these issues, but not completely. Zhang et al. (2016) analyzed errors from a Gill sonic anemometer during precipitation, and found a higher sensitivity to rain in the sonic temperature than in the wind components. They argued that since water droplets in the measurement cell will accelerate the speed of sound c, the sonic temperature T_s would be more affected than the wind u_a, because u_a does not directly depend on c, whereas T_s is proportional to c^2.
Non-orthogonal sonic anemometers such as CSAT3 have the advantage that they cause less flow distortion than orthogonal models. However, the probe, boom, mast and other supports upwind of the optical path all influence the measurements to some extent, and wind coming from the *shadow sector* will be contanimated. It is therefore recommended to orient the anemometer into the prevailing wind, but this requires knowledge of the local climatology, which was not available on our site. Campbell Scientific (2012) reports good accuracy within ±170° azimuth from the negative x-axis, but flow distortion is addressed in 5.3.2.

Different measurement rates are possible, typically 10 Hz or 20 Hz. At Iškoras, our field site, it was set to run at 20 Hz, that is once every 0.05 seconds. Wind speeds in the horizontal have a measurement resolution, i.e. smallest measurable change as given by the root mean square error (rms), of 1 mm s^{-1}, and in the vertival rms = 0.5 mm s^{-1}. The rms of c is 15 mm s^{-1}, which translates to a temperature error of 0.025 °C. The accuracy outside the distortion angle is < ±8 cm s^{-1} for horizontal wind speed and < ±4 cm s^{-1} for

the vertical.

The reader may refer to the instruction manual (Campbell Scientific, 2012) for more details on the instrument.

4.2.2 Infrared gas analyzer

The LI-7500 is an open-path infrared gas analyzer (IRGA) that measures the molar density of water vapor and CO_2 for flux calculations (LI-COR, 2004b), as well as the air pressure. It can run at a sampling rate of up to 20 Hz, but unlike sonic anemometers, the LI-7500 is of little use on its own because high-frequency measurements of gases make no sense unless they are complemented by turbulent wind data.

The IRGA sensor head, as seen in Fig. 4.3, consists of three main parts: an infrared source, a chopper filter wheel and a lead selenide detector (LI-COR, 2005). The infrared source emits a radiative beam through a window, but this needs filtering to be centered around three different wavelenghts, which is done by the chopper filter wheel. The three wavelengths are 4.26 μm and 2.59 μm, which absorb CO_2 and H_2O, respectively, and 3.59 μm which is transparent to both gases. The chopper wheel rotates 150 rounds per second, and it is assumed that the air does not change within one round, but this condition is sometimes violated during precipitation, which we will address at the end of this section. The filtered beam is then transmitted through the measurement cell, and the detector measures the absorption for each wavelength. The transparent wavelength provides a reference transmissivity for comparison with the two absorbing wavelengths. This relation is described below, following LI-COR (2004b):

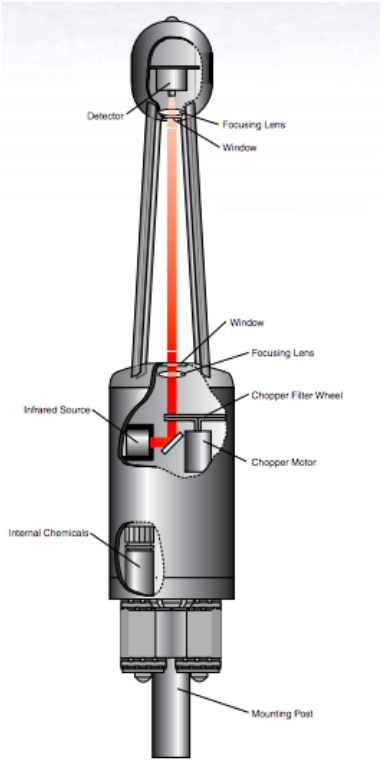

Figure 4.3: Cut-away representation of the LI-7500 sensor head. An infrared radiation beam is emitted through an optical path of in situ air. Measurements of the absorption are then converted to molar densities. Adopted from LI-COR (2005).

$$\alpha_i = 1 - \frac{A_i}{A_{ir}} \tag{4.9}$$

Here, α_i is the absorptance of gas i, A_i is the power received in an absorbing wavelength by the detector for gas i, and $A_{ir} > A_i$ is the power received in the reference, transparent

wavelength. The absorptance is then used to calculate the molar density ρ_i [mol m^{-3}] of gas *i*:

$$\rho_i = P_{ei} f_i \left(\frac{\alpha_i}{P_{ei}} \right) \tag{4.10}$$

where $f_i()$ is an empirically-derived polynomial calibration function, and P_{ei} is the equivalent pressure, which we will outline in the next paragraph. Finally, Eq. 4.9 is combined with Eq. 4.10, which yields

$$\rho_i = P_{ei} f_i \left(\left[1 - \frac{A_i}{A_{ir}} z_i \right] \frac{S_i}{P_{ei}} \right) \tag{4.11}$$

The zero coefficient z_i is a tuning parameter that accounts for drift in the zero reference levels due to temperature changes in the ambient air. S_i is a span adjustment coefficient that adjusts the sensitivity to changes in absorptance, which can also vary with time due to mechanic imperfections. Both z_i and S_i are set during calibration.

The equivalent pressure P_{ei}[1] of gas *i* must not be confused with its partial pressure. Rather, P_{ei} of gas *i* is the weighted sum of partial pressures of the ambient gases, each weighted by a pressure broadening[2] coefficient a_j which relates how gas *j* broadens the spectral band of gas *i* LI-COR (2004a). This effect is called *spectral cross-sensitivity* (LI-COR, 2018). Gases of similar structure are more effective at broadening the absorption lines of each other, which explains why each ambient gas gets its own broadening coefficent. Fortunately, the other greenhouse gases in the atmosphere do not influence the absorption by CO_2 and water vapor, and for water vapor the equivalent pressure is simply the total air pressure, which is measured in the LI-7500 control box. On the other hand, the CO_2 absorption is indeed altered by both H_2O and O_2 (LI-COR, 2004b). It is assumed that the O_2 content is the same during calibration as in the field, and that the contribution from O_2 to the CO_2 signal is incroporated in the calibration function. But since the H_2O level in the atmosphere is highly variable, the contribution from the mole fraction of water must be accounted for. Unless the air is completely dry, CO_2 will have an equivalent pressure slightly higher than the total pressure. This correction is fairly small, but significant. A related but slightly different effect is the inherent instrumental cross-sensitivity between gases, which is due to imperfect optical filtering. The instrumental cross-sensitivity will always magnify the true concentration, and the spectral cross-sensitivity will lead to overestimated CO_2 levels. Fortunately, both effects are corrected for in the software provided by the manufacturer.

As for sonic anemometers, the performance of open-path IRGAs is weather-dependent. Dew deposition on the windows can lead to bad readings if the droplets grow large enough, but tilting the sensor head by a certain angle relative to the vertical reduces this risk. Precipitation is perhaps a greater concern, because it can obstruct the optical path such that the air sample changes continuously. If an airborne hydrometeor is in the measurement cell for just an instant, it can jeopardize the comparison between sample and reference, i.e. the fraction in 4.9, because A_i no longer represents the same air as A_{ir},

[1] Equivalent pressure is sometimes referred to as effective pressure.

[2] Pressure broadening is the increase in absorption band width with increasing pressure.

as they are not measured simultaneously. Readings under rainy conditions can be of very poor quality, and tilting the instrument makes little difference during the rainfall. Flies and mosquitious, of which there were thousands at our site, would cause similar issues whenever they block the air sample.

At 20 Hz sampling rate, the LI-7500 has a root mean square error of 0.0061 mmol m^{-3} for CO_2 and 0.26 mmol m^{-3} for H_2O. For more on the theoretical background and technical specifications, refer to e.g. the instruction manuals LI-COR (2004b) and LI-COR (2004a).

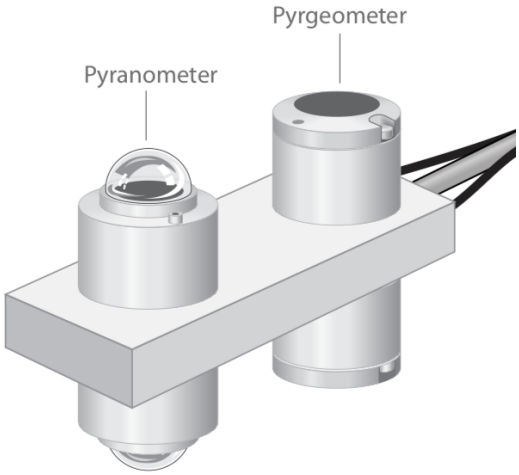

Figure 4.4: Illustration of the CNR 1 Kipp & Zonen net radiometer. Adopted from Campbell Scientific (2010).

4.2.3 Radiometer

The natural separation between longwave and shortwave radiation in the Earth's atmosphere can be exploited in radiative balance measurements. Consequently, the CNR 1 Kipp & Zonen net radiometer consists of four sensors: two CM 3 pyranometers measuring solar radiation, and two CG 3 pyrgeometers for the longwave radiation. It is seen from Fig. 4.4 that one of each sensor type is faced upwards, and the other is faced downwards, for the downwelling and upwelling components, respectively.

The CM 3 pyranometers consist primarily of a thermopile sensor and a glass dome. The thermopile is painted with a black coating. This ensures total absorption of all wavelengths, but only the radiation within the desired shortwave or longwave band is transmitted to the sensor. This radiation is then absorbed and converted to heat, which yields a temperature gradient through the detector. The temperature gradient then generates an electric voltage signal that is proportional to the measured shortwave radiation.

Following Kipp & Zonen (2002), the conversion between voltage V and flux of irradiance E for the CM 3 is simply

$$E = \frac{V}{C} \tag{4.12}$$

where C is a calibration constant, identical for the four sensors, but variable between

different CNR 1 instruments.[3] The CG 3 pyrgeometer works similarly to the pyranometer, with one important exception: CG 3 measures the difference in infrared emission between the ground or atmosphere, and the sensor itself. Because all bodies emit blackbody radiation, we have to add the infrared irradiance associated with sensor temperature. The conversion equation for the CG 3 is

$$E = \frac{V}{C} + 5.67 \cdot 10^{-8} \cdot T^4 \tag{4.13}$$

where T is the pyrgeometer temperature in Kelvin.

The radiation outside the desired spectrum is filtered out by a dome for the case of the CM 3, and by a flat window for the CG 3. This filtering is illustrated in Fig. 4.5.

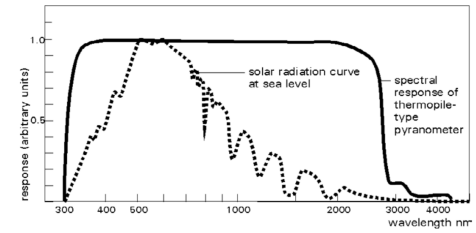

(a)

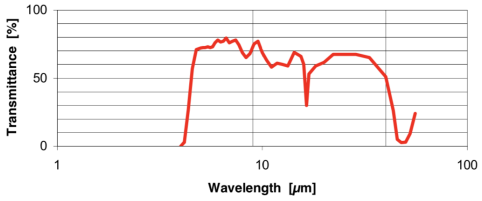

(b)

Figure 4.5: Spectral sensitivity of (a) the glass dome for the CM 3 pyranometer, given by the solid line and (b) the CG 3 pyrgeometer window. Shortwave radiation in (a) is transmitted through the dome, whereas longer wavelengths are obstructed. The dashed line represents the solar spectrum under a blue sky. The low-pass filter in (b) is opaque to wavelengths shorter than 4.5 μm. Adopted from Kipp & Zonen (2002).

There are a few points to make regarding the shortcomings of the CNR 1 radiometer, and the pyrgeometer, measuring longwave, is especially sensitive to certain errors. One clear difference between the two sensors is the window shape. The CG 3 flat window has the advantage over a classical spherical shape that it allows for uniform coating on the surface, which improves the low-pass filtering (Kipp & Zonen, 2003). However, its field of vision is only 150 degrees, whereas the CM 3 dome can sense all 180 degrees, which

[3]The four sensors are trimmed by shunting resistors in the CNR 1 body to have the same calibration constant (Kipp & Zonen, 2002, p. 7).

corresponds to the whole hemisphere. Fortunately, the blind sector near the horizon does not contribute significantly to the longwave signal.

What is worse is the effects of moisture. If water is deposited on the CG 3 window, which typically happens late at night or early in the morning after strong radiative cooling, the spectral transmittance illustrated in Fig. 4.5b is no longer valid. Dew and frost are excellent absorbers of infrared radiation, and to alleviate issues related to nighttime cooling, a heating device can be incorporated in the radiometer. However, when the heater is turned on, it will introduce some errors, both modifiying the sensor temperature needed for CG 3 measurements, and causing zero drifts in the CM 3 (Kipp & Zonen, 2002). This is still preferred over the adverse effects from water deposition, but for the present study we did not employ a heater, due to power limitations. Rain- and snowfall on the CG 3 window may also obstruct the far infrared radiation, but this is not as problematic, because during cloudy conditions, the boundary layer is typically well mixed and the cloud base has a temperature close to that of the surface layer. Thus, the CG 3 signal $\frac{V}{C}$ in eq. 4.13 should be close to zero anyway. This is certainly not the case when dew or frost is forming: Longwave outgoing radiation at night cools the boundary layer, but does not affect the free troposphere. In such conditions, there should be a strong negative signal from the upper pyrgeometer, but this remains undetected if the window is obscured.
The greatest limitation of the pyrgeometers, however, is the window heating error, which arises when the upward-facing CG 3 window absorbs solar radiation. Even though shortwave radiation is blocked by the low-pass filter, it can still heat up the window itself, which will then emit longwave radiation towards the thermopile. This is only a problem in daytime, but on clear days with solar radiation of 1000 W/m^2, an offset of 25 W/m^2 or 5-10 % of typical longwave values should be expected. This error can be avoided by shading or ventilating, but neither of these options were practical on our site. The so-called f-correction (Foken, 2008b, p. 193), which takes this heating into account, was not applied. Likewise, the CM 3 may suffer from far infrared cooling during the night, which can lead to negative readings of up to 15 W/m^2 instead of 0.
Moreover, on sunny days with low atmospheric humidity, some solar infrared radiation in the range between 2.5 and 5.0 μm can reach the ground and increase the measured downward longwave signal by a few percent. Fortunately, the low-pass filter, which blocks all wavelengths shorter than 4.5 μm, is opaque to most of this signal.
Finally, the shadow cast by the sensor and tripod might disturb the source area of both upwelling terms. However, since the area of influence is quite large – its radius being 10 times greater than the measurement height, i.e. > 300 m^2 in our case – the error from small shadows is unlikely to exceed 1 %.

4.2.4 Soil heat flux sensors

A heat flux sensor measures the heat flux through the device itself. Like the CNR 1 radiometer, the HFPO1 is a thermopile, i.e. it converts a temperature difference to an electric voltage signal U. This signal, which is proportional to the temperature difference,

is then divided by a reference sensitivity S_{ref} to give the heat flux:

$$Q_G = \frac{U}{S_{ref}} \tag{4.14}$$

where Q_G is the flux and U is the voltage signal. An illustration of this concept is given in Fig. 4.6. The sensor has a conductivity of 0.76 W m^{-1} K^{-1} (Hukseflux, 2016a), which is greater than peat soil conductivities, ranging from around 0.06 m^{-1} K^{-1} to 0.5 m^{-1} K^{-1} depending on the soil moisture (Arya, 2001, p. 50). It is therefore recommended to ensure close contact between the plates and the soil – there should be no air pockets around the sensors, because the conductivity of air is about an order of magnitude lower than that of peat soil. Most soil heat flux sensors are built for mineral soil (Laurila et al., 2012), which is less porous than peat, and unlike the HFP01SC model, HFP01 does not include a self-calibrator which accounts for different conductivities. Thus, even in the absence of air pockets, a heat flow deflection error is introduced by the plate, but this effect is lower towards the center of the sensor, from which most of the signal originates.

If the plates are installed and buried properly, the measurements are assumed to be representative of the undisturbed soil heat flux at the location of the sensor. However, Hukseflux (2016b) recommends using two sensors for each depth at a distance of > 5 m, because it is difficult to find one location representative of the whole catchment. Differences in surface and soil characteristics are inevitable, and our site was certainly not homogeneous. Moreover, it is better not to install the sensor at the surface or just beneath, but rather to bury it at some depth between 0.05 m and 0.1 m, since surface-based thermometry poses several problems. These are e.g. a) moisture flow distortion b) absorption of solar radiation and c) higher exposure to other surface processes, which could alter the sensor's mechanical stability. On the other hand, the deeper the installation, the larger the offset from the instantaneous soil heat flux at the surface, both in terms of flux amplitude and time delay. Thus, heat flux plates should in general be accompanied by soil thermometers placed at shallower levels, for instance at 0.04 and 0.02 m, to calculate the heat storage using so-called calorimetry. In fact, Liebethal et al. (2005) suggests burying the flux plates quite deeply, ideally at a depth where the flux equals zero, and add the heat storage.

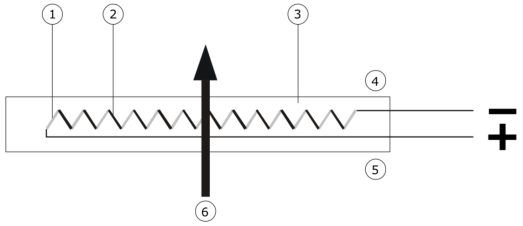

Figure 4.6: The HFP01 heat flux sensor is a thermopile and consists of a number of thermocouples. The heat flux, marked by the arrow, runs across the sensor body and is proportional to the temperature difference and the average heat conductivity of the sensor. Adopted from Hukseflux (2016b).

Unfortunately, we were not able to follow all the procedures recommended by the manufacturer and the literature, since we did not bring soil thermometers to the site and had to rely exclusively on two heat flux plates. The impressive surface heterogeneity within just a few meters, both in terms of albedo and surface relief, suggested that we would not be able to find a representative sensor location for the average ground heat flux, given our limited instrumentation. Unlike the other instruments in our campaign, heat flux plates measure on a point-scale. However, although deeper installation levels are not necessarily more representative of an ecosystem on annual time scales,[4] they do ensure some filtering of the fine-scale variability at the surface (Heginbottom et al., 2013, p. 441). Thus, we buried the two sensors at 0.1 and 0.2 m depth on the same location, which certainly resulted in an underestimation of the ground heat flux at the surface.

[4]Even at great depths where the diurnal and seasonal signals are gone, significant horizontal temperature gradients can be found due to e.g. snow cover differences in wintertime and slope aspect.

Chapter 5

Data and methods

5.1 Calculating fluxes

The turbulent flux of any scalar s is the covariance $\overline{w's'}$, where w' is the fluctuation of the vertical wind. However, as outlined in Section 2.4, the eddy covariance method is based on several assumptions. If these are not fullfilled, the fluxes must be corrected. Numerous eddy-covariance processing softwares that perform these corrections are available, but for the present study we have used the TK3 "Turbulence Knight 3" package, which is developed at the University of Bayreuth (Mauder and Foken, 2015) and has been validated by Fratini and Mauder (2014).

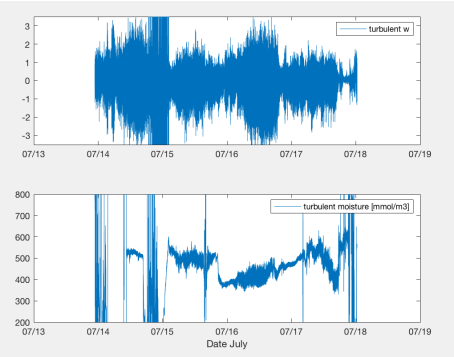

Figure 5.1: Sample of the turbulent vertical wind [m/s] (top panel) and water vapor density (lower panel) measured by the sonic anemometer and IRGA, respectively.

The very first part of the flux calculation procedure is the transformation of raw electronic voltage signals into meteorological parameters, but this is done internally in the instrument firmware and is detailed in Section 4.2. In the following chapter, we will go through most of the necessary algorithms involved in calculating good-quality fluxes from an eddy-covariance system. All steps are outlined in Mauder and Foken (2015) and discussed in greater detail in e.g. Foken et al. (2012b), should the reader be interested.

5.1.1 Plausability tests

Once meteorological units are obtained, the first correction step in the processing is the plausability tests. The high-frequency data can contain erroneous values, such as outliers beyond the physically meaningful range, spikes, or constant values over a certain time. The most important source of noise for our dataset was likely precipitation, which can obstruct not only CSAT3 and LI-7500 sensors, but also the measurement cells. Other spikes can arise from an insufficient power supply or electronic noise. The quality control is two-fold: First of all, physically unlikely values are tossed out of the analysis for flux calculations. Such outliers are identified using consistency limits, i.e. rigid upper and lower bounds for each parameter.

Consistency limits are meant to be conservative (Vickers and Mahrt, 1997), so that all outliers will be rejected even if it means some good data is lost too. These thresholds can be very site-specific, and careful inspection of the turbulent time series and their statistical properties is necessary (Rebmann et al., 2012). In our case, some parameters were more clearly constrained than others. The vertical wind, for instance, as seen in the top panel of Fig. 5.1, exceeded ±2 m/s only about 2 % of the time and then often in a very suspicious manner.

Other parameters, such as water vapor density, given in the lower panel of Fig. 5.1, were more difficult to evaluate, because they had more outliers and varied on long time scales, often several days. Due to this slower variability, the statistics considered for determining thresholds were different from one week to another. We arrived at 200 and 650 mmol/m^3 as upper and lower bounds, which ruled out about 15 % of the time series.

The second part of the quality control is spike detection. Spikes are high frequency noise in a dataset, not necessarily unphysical themselves, but given the values adjacent to them, they are considered erroneous. There is no accepted method for separating plausible physical variability and instrumental problems (Vickers and Mahrt, 1997), perhaps especially not in turbulence measurements, where the true, finescale behaviour *is* spiky and should be. However, one common approach is to define a removal criterion in terms of a specific number of standard deviations. All values that depart by D standard deviations, or standard deviation equivalents (SDE's) for the case of TK3,[1] from the mean of a running window of 15 values are marked as spikes, and are either replaced by interpolation or the last value, or excluded for all further calculations. The same applies to data gaps, which are inevitable in turbulence measurements because all instruments suffer from some malfunction from time to time. For our study there was little difference in the two approaches, but we discarded such gaps, since Rebmann et al. (2012) warn particularly about linear interpolation, which can lead to systematic error.
The discrimination factor D can for instance be set to 3.5. Mauder and Foken (2015) recommend D = 4.5 in a standard deviation scheme, but for SDE's they found D = 7 to work well, and we therefore chose D = 7. The spike detection algorithm used in TK3 follows Vickers and Mahrt (1997) and is more sophisticated than simply replacing all spikes. If at least four spikes lie next to each other, which would correspond to a duration of 0.2 s for a 20 Hz sampling rate, they are considered real and not labelled as spikes. The

[1] Standard deviation equivalents, or *median absolute deviations*, differ from traditional standard deviations in that means are replaced by medians. This is found to be more robust (Mauder et al., 2013).

spike detection process is repeated four times, each time automatically stricter than before because statistical quantities themselves are influenced by spikes. The discrimination factor is increased by 0.1 at every new stage for all variables, except temperature for which it is raised by 0.5. After five rounds of spike detection, a half-hour measurement is "hard-flagged", i.e. labelled as poor-quality, if more than a critical share of the data points have been replaced. Some authors allow for as much as 10 % spikes within one averaging interval, but this is not recommended, and we set this threshold to 1 %.

5.1.2 Cross-correlation analysis

Because an eddy-covariance system consists of two instruments, there is a risk that simultaneously sampled data are stored at different points in time. In other words, the covariance equation between between a scalar x and a wind component u over N data points

$$\overline{x'u'} = \frac{1}{N}\sum_{n=1}^{N}[(x_n - \overline{x})(u_n - \overline{u})] \tag{5.1}$$

is not true, because x_n and u_n from the data logger do not coincide. Such time lags are particularly large for closed-path IRGAs, because they have an intake which is apart from the measurement cell, i.e., they do not measure the in-situ air. For open-path analyzers, the time lags are in part due to different inertia in the electronic signal treatment of the instruments, but above all to the spatial distance between the sensors.

Recall that our open-path IRGA was mounted 15 cm away from the anemometer, pointing south relative to the northward-facing CSAT3. This means that, if the wind is 3 m/s and from the north, an eddy is recorded 0.05 s earlier by the CSAT3 than by the IRGA. Before any further calculations, the TK3 therefore cross-correlates x and u and finds the time shift that returns the maximum value. N was set to 18,000, corresponding to 30 min, for our study.

5.2 Flux corrections

Some of the following steps involve the correction of one flux based on another. For example, the SND algorithm accounts for the effect of water vapor on the sensible heat flux, which means that the quality of this flux will depend on that of the latent heat flux. TK3 therefore runs those corrections iteratively until the fluxes do not change significantly anymore.

5.2.1 Coordinate rotation

One requirement for eddy covariance measurements is the condition that the mean vertical wind is negligible. However, streamlines measured in the lower boundary layer tend to

follow the local surface tilt, which can be close to but is usually not identical to zero.

Moreover, a perfectly level sensor relative to gravity is hard to obtain, resulting in additional tilt of perhaps 1°. Thus, the slope-normal vertical wind will not be parallel to the sensor's vertical axis. Some of the horizontal wind will then be mistaken for vertical motion, which is very undesirable. The misalignment of the sensor relative to gravity and to the local surface is usually accounted for by a rotation, from the coordinate system of the CSAT3 to that of the local windfield.

A three-dimensional coordinate rotation has three degrees of freedom, i.e., three angles that must be determined, which we will denote θ, ϕ and ψ. There are primarily two different rotation schemes used in boundary layer meteorology: the double rotation and the planar fit. Both schemes tilt the coordinate system so that the mean vertical wind vanishes, but they work on different time scales.
In the planar fit, introduced by Wilczak et al. (2001), the mean-streamline plane is calculated by linear regression using a large data ensemble of weeks or even the whole measurement period. The mathematical derivation is complicated, and since we used the double rotation for our calculations, we have not included it. But the post-rotation plane from the planar fit will more or less coincide with the local surface, and the mean vertical wind $\overline{w}$ averaged over the whole data ensemble is zero. However, for individual half hour periods $\overline{w}$ is in general non-zero.

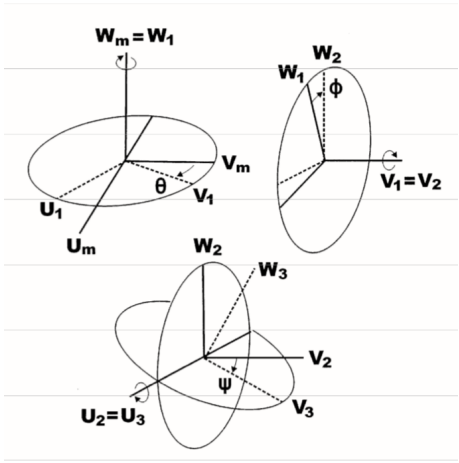

Figure 5.2: Illustration of the double rotation procedure (top panels) after Foken (2008b). The third rotation (lower panel) is not performed.

The tilting performed by the double rotation (DR) method, on the other hand, is such that the vertical wind vanishes for every averaging period. The rotation steps involved are visualized in Fig. 5.2 and were introduced by Tanner and Thurtell (1969). Each half hour period gets its own unique coordinate system, but the information on the mean wind direction is of course kept through the whole procedure. The first step in a DR is the alignment of the x-axis into the mean horizontal flow, which requires rotating the x-y plane by the yaw angle θ about the sensor's z-axis, i.e.,

$$\begin{aligned} \overline{v} &= 0 \\ tan(\theta) &= \left(\frac{\overline{v_1}}{\overline{u_1}}\right) \end{aligned} \tag{5.2}$$

where the index 1 denotes the initial, non-rotated coordinate system of the anemometer. Next, the x'-z plane with the rotated x'-axis, indicated by a prime for convenience, is tilted about the y'-axis until the vertical wind vanishes, resulting in the pitch angle ϕ:

$$\begin{aligned} \overline{w} &= 0 \\ tan(\phi) &= \left(\frac{\overline{w_1}}{\overline{u_2}} \right) \end{aligned} \tag{5.3}$$

The DR was the main rotation method in the early years of eddy-covariance measurements, when most experiments were carried out over "golden days" in fair weather at homogeneous terrain. However, as more difficult conditions were explored in long-term campaigns, shortcomings of the DR became obvious (Lee et al., 2004). First, in low wind there is a risk of over-rotation, resulting in very large and unphysical pitch angles. Second, the information on any nonzero $\overline{w}$ is lost, which is unfortunate if e.g. strong ascent affects the wind field and introduces vertical advective fluxes. And third, the change in coordinate system at every averaging interval leads to a high-pass filtering of the flux data, which means that the rotated time series is in fact discontinuous – this may be problematic at rough or complex sites where large differences in $\overline{w}$ are expected.

On the other hand, the planar fit will be contaminated by strong winds, and the mean wind threshold in TK3 is set already at 5 m/s. So for our study, the planar fit would require discarding precious high-wind data, which we found insupportable. Moreover, even though the terrain on our site was somewhat rough, strong and sustained vertical motion is unlikely owing to e.g. the relatively level surface. For these reasons we chose the DR. TK3 applies the coordinate rotation after having calculated means and covariances, which gives the same result as rotating the raw data.

5.2.2 Moore

The so-called Moore corrections (Moore, 1986), which account for spectral loss from e.g. sensor separation, were by mistake not switched on in our TK3 runs. Fortunately, based on inspection of a period from our dataset of five days where this correction was applied, the correlation between 'pre-Moore' and 'post-Moore' was > 99 % in all three turbulent fluxes. However, Moore-corrected fluxes were somewhat greater (in the absolute sense): an increase of 6 % was seen in the NEE, 5 % in LH and 2 % in SH, which should be kept in mind as we go through the results of our campaign.

5.2.3 SND

As discussed in Section 4.2.1, the sonic anemometer does not measure the actual air temperature, but the so-called sonic temperature T_s. So the covariance between sonic temperature and vertical wind is in fact not the sensible heat flux, but very close to the buoyancy flux (Foken, 2008b, p. 115). To get the true $\overline{w'T'}$, we need to account for the humidity effect in $\overline{w'T'_v}$. The algorithm involved is called the SND correction, named

after Schotanus et al. (1983), who showed that

$$\overline{w'T'} = \overline{w'T'_s} - 0.51 \cdot \overline{T} \cdot \overline{w'q'} \tag{5.4}$$

This correction is necessary and was switched on for our study.

5.2.4 WPL

The WPL correction, after Webb et al. (1980), is applied to the fluxes of CO_2 and latent heat, and accounts for the following issue: Since most infrared gas analyzers measure concentrations of trace gases per volume and not per mass or per mole, fluctuations in water vapor and temperature, which modify the air density, will change the measured concentration even when there is no change in the scalar mixing ratio.

The corrected CO_2 flux becomes

$$\overline{F_c} = \overline{w'\rho'_c} + \mu\frac{\overline{\rho_c}}{\overline{\rho_a}}\overline{w'\rho'_v} + (1 + \mu\sigma)\overline{\rho_c}\frac{\overline{w'T'}}{\overline{T}} \tag{5.5}$$

where ρ_c, ρ_a, ρ_v are the densities of CO_2, dry air and water vapor, respectively, $\mu = \frac{m_d}{m_v} = 1.6$ is the ratio between the molar masses of dry air and water vapor, and $\sigma = \frac{\rho_v}{\rho_a} \approx 0.66$ is the ratio of water vapor and dry air densities.

The correction for the latent heat flux is a simplified version of eq. 5.5:

$$\overline{F_v} = (1 + \mu\sigma)\left(\overline{w'\rho'_v} + \overline{\rho_v}\frac{\overline{w'T'}}{\overline{T}}\right) \tag{5.6}$$

Both were performed by TK3.

5.3 Quality control

The following two tests will return a quality flag for each flux value according to a flag scheme which is selected by the user, in our case that from the so-called Spoleto agreement (Mauder et al., 2013). These classification schemes are more or less the same, in that three quality classes are identified: 1) high quality, 2) moderate quality and 3) low quality. If the two tests disagree on the quality of a flux value, the highest flag (low or moderate quality) of the two is assigned to that flux. All fluxes of the third quality class are rejected, while those of the other two are kept.

5.3.1 Stationarity test

The assumption of stationarity, i.e. steady state conditions during each averaging period, might not always hold, due to e.g. gravity waves or intermittent turbulence (Foken, 2008b, p. 118). Therefore, TK3 runs a steady-state test where each 30-min flux is split into 6 intervals of 5-min length. If the average of these depart by more than a certain threshold from the total 30-min covariance, the flux is considered non-steady and discarded. In

TK3, this threshold is set at 30 %. Unfortunately, there is no guarantee that this test identifies all non-steady cases (Foken et al., 2006). Refer to the TK3 manual (Mauder and Foken, 2015) for mathematical details.

5.3.2 Integral turbulence characteristics test

The final quality test evaluates the integral turbulence characteristics (ITC) of the processed data. According to the so-called flux-variance similarity (see e.g. Kaimal and Finnigan, 1994, chap. 1), the variance of a turbulent parameter divided by its turbulent flux is almost constant or a function of the atmospheric stability. This suggests that we can compare the predicted flux from this theory to its actual value, and discard fluxes that exceed a threshold. The ITC test is supposed to also identify flow distortion effects (Mauder et al., 2013). For the sake of brevity we omit the mathematical derivation of this analysis, but the reader may consult Mauder and Foken (2015) for a thorough discussion of the ITC test in TK3.

5.3.3 Ogive test

As radiation is classified into longwave and shortwave, so is atmospheric motioned typically regarded as either turbulent or synoptic (Stull, 1988, pp. 32-33). A pronounced spectral gap at time scales of about an hour is often found, which is why an averaging time T of 30 min is typically applied to eddy-covariance fluxes. However, this sometimes excludes the flux contributions of large eddies. In other words, T = 30 min can act like a high-pass filter which does not detect longwave atmospheric structures forced by for instance topography and gravity waves (Foken, 2008b, p. 113). So the spectral gap does not always exist, and a significant overlap can be found between large turbulent eddies and real trends such as frontal passages, cloud cover changes and diurnal variations. Extending the averaging period is in general not a recommended solution, because that might jeopardize the assumption of stationarity.

One way to test if the chosen T is sufficient is using so-called *ogives*. The ogive of a turbulent flux is calculated as the cumulative cospectrum of the vertical wind w and the constitutent c, integrated from high to low frequencies:

$$Og_{w,c}(f_0) = \int_{\infty}^{f_0} Co_{w,c}(f)df \tag{5.7}$$

At a sampling rate of 20 Hz, the maximum frequency that can be resolved is 10 Hz, which replaces ∞ in eq. 5.7. We used 3-h data for each ogive, which gave a minimum frequency of $f_0 = \frac{1}{0.5 \cdot 180 min} = 1.86 \cdot 10^{-4}$ Hz. In part following Foken et al. (2006), we normalized the ogives by the maximum absolute value, i.e.

$$\widehat{Og}(f_0) = \frac{Og(f_0)}{max\left|(Og_{w,c}(f))\right|} \tag{5.8}$$

If the normalized ogive converges towards ± 1 at low frequencies, T = 30 min is sufficient. Otherwise, the longwave contributions are probably significant. However,

while this can provide information on the flux quality, there is no simple way to correct non-converging ogives (Massman and Clement, 2004).

TK3 has the option of calculating ogives, but we did it manually in MATLAB using fast Fourier transforms to obtain cospectra. Following Stull (1988, pp. 303, 331), the cospectrum between w and c is expressed as

$$Co_{w,c} = \frac{1}{N^2}[Re(\mathcal{F}_{w'}(N) \cdot Re(\mathcal{F}_{c'}(N) + Im(\mathcal{F}_{w'}(N) \cdot Im(\mathcal{F}_{w'}(N)] \tag{5.9}$$

where N is the number of Fourier coefficients. FFT is equivalent to the discrete Fourier transform $\mathcal{F}_{x'}(N)$ (Stull, 1988, p. 310), where x' is any turbulent parameter.

Since the ogive test is performed with raw turbulence data, the various corrections and plausability tests applied to the fluxes are not included in the ogive calculation. However, the only correction relevant for ogives is that for the time delay between sonic and IRGA measurements, which should be less than 0.5 s (Foken et al., 2006). Since very few cases from our campaign would have time shifts greater than that, we did not account for this effect.

5.4 Flux footprint

Unlike soil heat flux plates and net radiometers installed just above the surface, an eddy covariance tower measures fluxes from a large source area (thousands of m^2) upwind of the sensors (Foken, 2008b, p. 82). The eddy *flux footprint* f depends on e.g. surface roughness, measurement height, atmospheric stability and wind speed and direction, and may or may not overlap well with the catchment of interest. In this study, we have used the footprint parameterization of Kljun et al. (2015), and the required input data is outlined in Kljun (2017). A brief review of this tool is given below.

Mathematically, f [m^{-2}] is the weight function which relates the surface flux $F(x, y, z = 0)$ over a large area to the eddy flux $F(x_0, y_0, z_m)$ as measured by an EC tower at $(x_0, y_0, z = z_m)$:

$$F(x_0, y_0, z_m) = \int_{-\infty}^{+\infty} \int_{-\infty}^{x_0} F(x', y', z = 0) f(x_0 - x, y_0 - y, z_m)\, dx\, dy \tag{5.10}$$

if the wind field is homogeneous. Positive x indicates the streamwise (downwind) direction, y is the crosswind direction and z is the vertical. Horst and Weil (1992) showed that f can be described in terms of a crosswind dispersion function $D_y(x, y)$ and a crosswind-integrated footprint $\overline{f}_y(x, z_m)$, i.e.

$$f(x, y, z_m) = D_y(x, y)\overline{f}_y(x, z_m) \tag{5.11}$$

assuming that the dispersion in the vertical is independent from that in the horizontal. $\overline{f}_y$ incorporates the dispersion in the vertical direction, and does not depend on y because it has already been integrated over the whole y axis.

Horst and Weil (1992) derived $D_y(x, y)$ and $\overline{f}_y$ using analytical techniques, but their solutions are reliable only in near-neutral conditions (Leclerc and Foken, 2014, p. 72). The approach taken by Kljun et al. (2015) is more pragmatic (see also Kljun et al. (2004) and involves so-called Buckingham Π theory (Stull, 1988, chap. 9), which is a method for finding empirical relationships between dimensionless groups.

First, they regard $\overline{f}_y$ as a yet indetermined function of x, z_m, h, $\overline{u}(z_m)$ and u_*, where h, $\overline{u}(z_m)$ and u_* represent boundary layer height, mean velocity at $z = z_m$ and friction velocity, respectively. These variables are thought a priori to be the scales relevant for f_y. The diabatic wind profile (Stull, 1988, pp. 384-385) incorporates the dependence of the footprint on atmospheric stability and surface roughness, via $\overline{u}(z_m)$.

Next, Kljun et al. (2015) present a set of four 'Π groups', i.e. dimensionless combinations of these parameters, and postulate that dimensionless forms of f_y and x[2] can be expressed as combinations of the Π groups, and find such combinations.

Now, the crosswind dispersion $D_y(x, y)$ in eq. 5.11 is assumed to have a Gaussian distribution, i.e.

$$D(x, y) = \frac{1}{\sqrt{2\pi}\sigma_y} exp(-\frac{y^2}{2\sigma_y^2}) \tag{5.12}$$

where y is the footprint's crosswind distance from the x axis. On the other hand, σ_y – the standard deviation of y – depends on boundary layer conditions and the distance from the flux tower, and Kljun et al. (2015) scale σ_y also using Π groups, similarly to $\overline{f}_y$.

These dimensionless forms are then applied to varies footprints of different stability regimes in a 'backward Lagrangian stochastic particle dispersion model' called LPDM-B, and tuned based on the model results. Finally, representative functions are fit to both the crosswind dispersion functions and the crosswind-integrated footprints using the same model, for all stability scenarios. These functions allow for the calculation of two-dimensional footprints and for estimating the relative flux contribution from a certain area.

The flux footprint parameterization (FFP) outlined by Kljun et al. (2015) is not really a footprint model, but provides a 'shortcut' to such models which are much more expensive to run. The validation against LPDM-B simulations gave good results, but like footprint models the FFP is based on assumptions of e.g. stationarity and horizontal homogeneity, and violations of these conditions could lead to unreliable footprint estimates. Fortunately, most of the fluxes that make it through the TK3 tests should be of at least moderate quality.

[2]Since the footprint is always relative to a certain measurement height z_m, f_y depends in practice only on x when this height is given, and not on z.

Chapter 6

Results and discussion

6.1 Weather conditions during the campaign

6.1.1 Comparison with climatology

The weather characteristics for the town of Karasjok in July 2017, when most of our measurements were taken, as well as the 1961-1990 climatology for July, are given in Table 6.1. Karasjok is located about 20 km north from Iškoras in a valley at only 131 m above sea level, and has a different climate than our field site near Iškoras. However, the climatology for Iškoras and its surroundings are unknown, because the weather station on the mountain top was established as late as in 2014. The Karasjok record, on the other hand, goes back to 1876.[1] Despite climate variability within the Finmmark interior, a comparison between the Karasjok summer climatology and the 2017 Karasjok summer should shed light on the whole region, including Iškoras.
Average temperature in Karasjok in July 2017 was 13.4 °C, which is slightly higher than the climatology. The July 2017 maximum temperature of 18.6 °C was almost one °C higher than the climatological maximum, but the minimum temperature increased by just 0.1 °C. Changes in wind speed and precipitation were more pronounced. The average mean wind of 2.2 m/s was more than 2.5 times the climatology, and the monthly max was also higher. The accumulated rainfall in July 2017 was twice the average, and significant rain was measured on almost half of the days, instead of just the climatological 1 in 3 rainy days for July. The rainiest days as reported by eKlima (2018), not given in the table, were 12, 18, 29 and 30 July, with 9.0, 12.4, 47.1 and 11.0 mm, respectively. Thus, July 2017 was a little warmer than usual, but above all windier and rainier. In fact, the interior of Finnmark and Troms had the highest precipiation anomalies in all of Norway in July 2017, as can be seen in Fig. 6.1.

[1] Strictly speaking, the proud Karasjok weather station was shut down in 2012, but a new one, erected in 2004 about 1 km away across the Kárášjohka river, came to replace it.

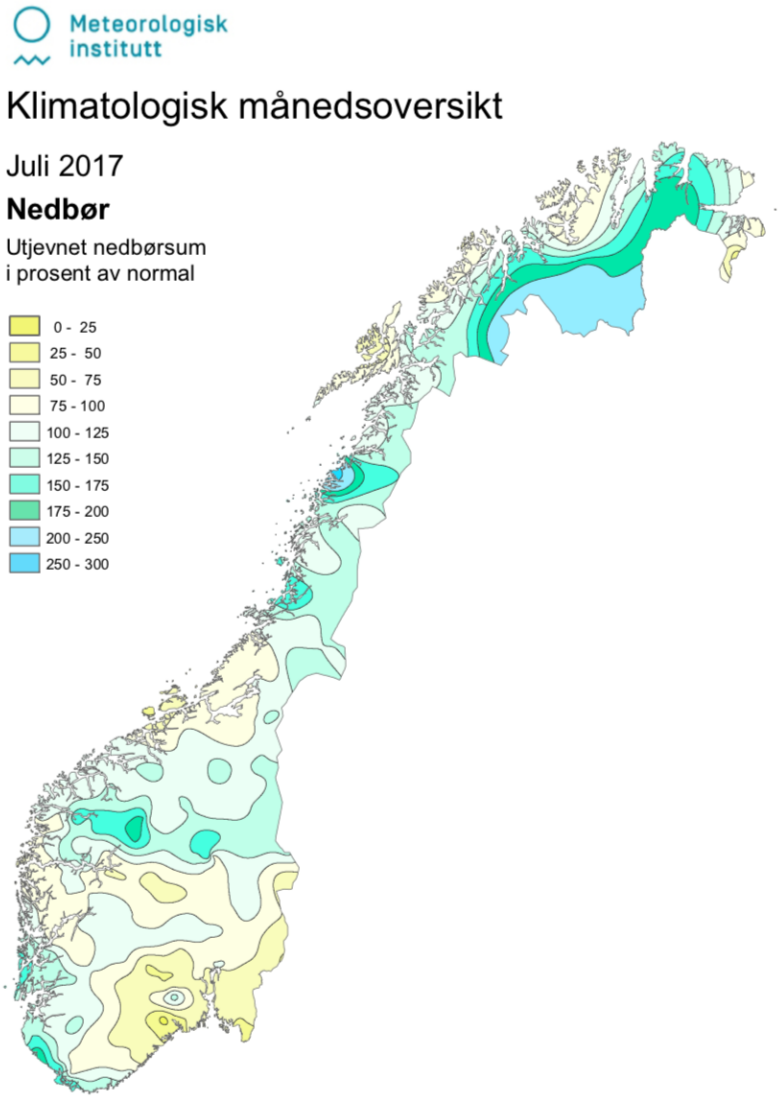

Figure 6.1: Precipitation in Norway in July 2017 relative to the 1961-1990 climatology. Note the high anomalies measured in continental Finnmark. Adopted from Kristiansen et al. (2017, p. 2)

	July 1961-1990	July 2017	Relative change [%]
Temperature [°C]			
Mean	13.1	13.4	2.6
Average daily max	17.7	18.6	5.1
Average daily min	8.2	8.3	1.5
Wind speed [m/s]			
Mean	0.9	2.2	155.8
Max	4.5	7.5	65.0
Precipitation p [mm]			
Total	71.0	143.4	102.0
Days with p > 1 mm	10.5	14.0	33.3

Table 6.1: Weather conditions in Karasjok in July 2017 compared to the 1961-1990 climatology, using data from eKlima (2018).

6.1.2 Basic meteorological parameters

In the following section we will go through the general weather patterns as observed by our instruments during the campaign. Unless otherwise stated, all values are 30-min averages, and all references to time are in local daylight savings time (UTC + 2).

6.1.3 Wind speed and direction

Time series of wind speed, wind direction and air pressure are given in Fig. 6.2. Following World Meteorological Organization (2008), the wind direction was not defined for wind speeds < 0.2 m/s. Wind directions were quite variable during the campaign, but southerly, easterly and northely winds were most common. In the last week of July, all directions were represented. The easterly wind was quite dominant in August, with some contributions from the north and west. Note that, while the wind direction certainly varied from day to day, it also seems to have evolved on time scales of roughly a week. Between 14 and 19 July, the wind turned slowly from northerly to southerly, back to northerly and then settled at northwesterly. This steady wind turning is very different from the behaviour observed between 22 and 31 July, when almost the whole wind rose was covered within single days. Yet, southerly winds are less favoured from 23 to 27 July. While winds in Karasjok are not necessarily representative of our station, we note that Nawri and Harstveit (2012) reported no prevailing wind direction in Karasjok apart from the cold season.

The wind speed U was in general low during the measurement period, with an average of 2.3 m/s. U exceeded 6 m/s only once and was lower than 4 m/s 81 % of the time. Between 9 and 12 July, the daily peak wind speed decreased from 5 m/s to 3 m/s. The wind intensified during the following four days, and reaches its maximum of 6.5 m/s on 16 July. Beginning on 18 July, U weakened for about a week, but then increased for the rest of the month, surpassing 4 m/s on 27 July. U dropped on 31 July, but rised again during the last few days. Diurnal cycles in wind speed are clearly seen on almost all days, including the day of peak U. The data coverage for wind speed and direction was about

86 %, and most of the data gaps are found around 14, 18 and 31 July.

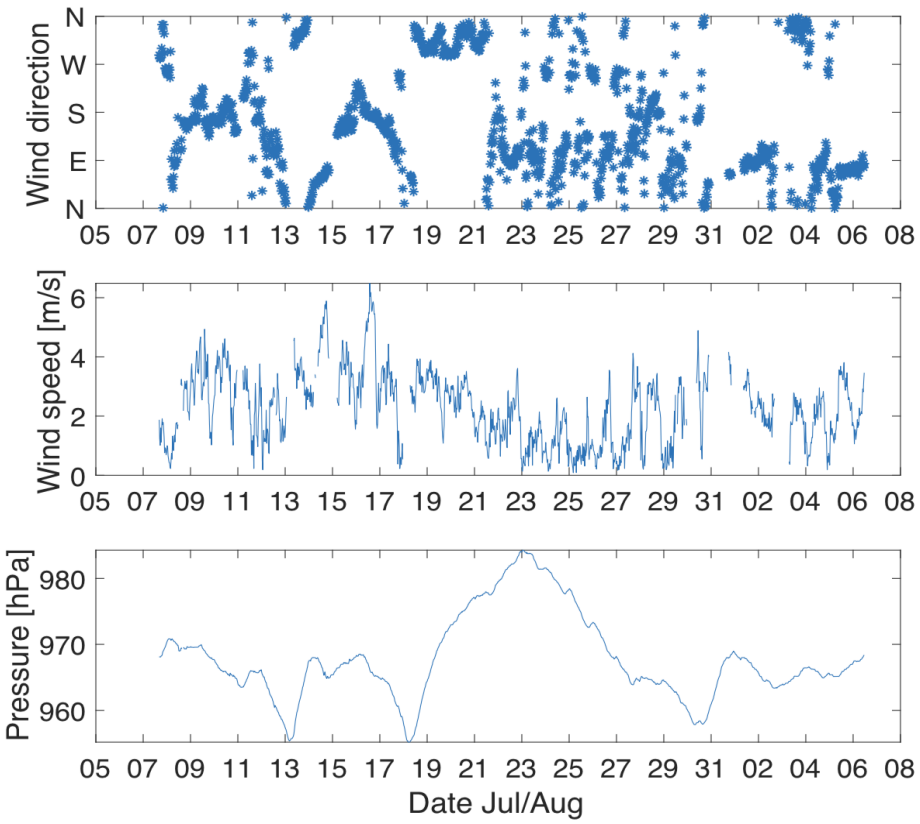

Figure 6.2: Top to bottom: Time series of wind direction, wind speed and air pressure at the site for the whole measurement period. Y-axis tick 'N' denotes northerly flow, i.e. blowing *from* the north, 'E' denotes easterly and so on.

Air pressure P was between 955 hPa and 985 hPa during the whole period, and had an average of 968 hPa. Recall that our site is located at 358 m.a.s.l. Pressure showed almost no diurnal cycle – rather, it varied on longer time scales of 5-15 days. The pressure minima measured on 13, 18 and 30 July seem to coincide well with the large data gaps in wind speed and direction, and high winds also came about roughly at the time of these dips. Frontal passages, bringing rain which can disturb the Li-7500 and CSAT3 sensors and measurement cells, might explain such a pattern, but power limitations from the solar panel under a thick cloud cover could also be a factor. P evolved smoothly throughout the campaign and attained relatively high values around 23 July, which might be the signal of a high-pressure system building up, bringing weak and unsteady winds, above all from

the east.

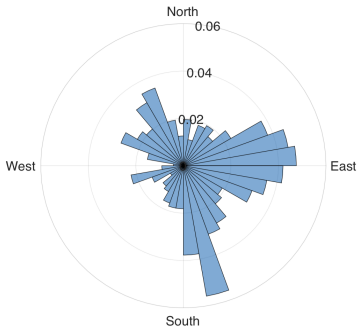

(a)

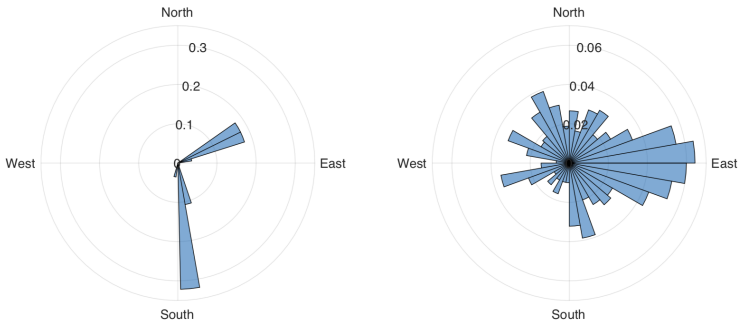

(b)

Figure 6.3: Polar histograms of the whole campaign for a) all wind speeds and b) for wind speed U > 5 m/s (left) and U < 3 m/s (right). The angular ticks 'East', 'North' and so on correspond to winds blowing from the east, north and so forth. Radial ticks denote the relative proportion of the data considered, i.e. 0.04 represents 4 % occurrence.

To get a better picture of the prevailing wind directions for the whole campaign, it is useful to draw a wind rose. This is shown in Fig. 6.3a. The wind rose gives the angle histogram for the wind directions, in this case during the whole measurement period. It is clear also here that the wind was irregular. Easterly winds seem to have been the most favoured, but the most common 10°-interval was south-southeast. Westerly winds were the least represented, but the northwest quadrant did show a certain signal. Thus, there appears to have been a symmetry in the meridional flow, likely related to the diurnal cycle in wind speed and possibly katabatic/anabatic circulation, but the zonal wind was largely easterly.

By putting thresholds on the wind speed, we can investigate the wind directions

associated with a relatively strong or weak flow. In the left panel of Fig. 6.3b, only the high wind episodes are included, defined as when the wind speed U exceeded 5 m/s. This eliminates 98 % of the cases, and only two days meet this criterion, namely 14 and 16 July.

The strong winds were either southerly or northeasterly with almost the same occurrance. However, for the low wind episodes when U < 3 m/s, as given in the lower panel of Fig. 6.3b, the pure southern component was far from dominant, and the whole wind rose received some signal. Even though direct westerly flow was rare, 36 % of the low wind episodes were from the two western quadrants. Yet, it was the easterly wind that prevailed in the low wind regime: 39 % of all the low-wind cases were within the NE-SE sector, i.e. easterly ±45°.

6.1.4 Temperature and humidity

The air temperature T and absolute humidity as measured by the sonic anemometer and the infrared gas analyzer, respectively, are given in Fig. 6.4. T ranged between 1.1 and 23.3 °C, but 80 % of the measurements were between 8.1 and 18.8 °C. The mean temperature for the whole period was 13.1 °C. The very pronounced minimum temperature was recorded at 1 a.m. on 8 July and can be confirmed by radiation data. The diurnal cycle was evident on most of the days, and the largest amplitudes were measured on the days between 24 and 28 July.

However, it is clear that factors other than the time of day also influenced the temperature, because it varied on larger time scales as well. Overall, temperatures were low between 13 and 16 July, 18 and 23 July and during the week in August. Very low amplitutes are seen on 19 and 20 July: Only 2.6 °C separated the maximum and minimum on the 19th. This couple of days was also the coldest in the whole time series, in terms of mean daily temperature. The warmest period started on 23 July and lasted for one week. The maximum temperature was measured on 28 July, but 25 July had the largest temperature difference, of 17.0 °C. In August, T was lower than 15 °C most of the time, and the diurnal cycle was less pronounced, but not absent. The data coverage was 85 %, and much of the missing data is found around 31 July, but also on 13 and 18 July, as well as some of the days in August.

The absolute humidity, referred to here as q [g/m^3], is the measure of water vapor density. Unlike relative humidity, q does not depend directly on the air temperature, but rather on advection and local evaporation. During the campaign, q ranged from 5.0 to 11.5 g/m^3, but the mean for the whole period was 8.5 g/m^3. In general, the humidity increased during the measurement period, as is evident from the least square's line. Local peaks are seen on e.g. 12, 17 and 30 July. Dry air was recorded on 9, 10, 15 and 16 July and between the 19th and 23rd, but also occasionally during the warm week. The humidity increased on 23 July, but remained below 10 g/m^3 most of the time, until the 27th when it showed an impressive variabilty. Large data gaps are seen between 29 July

and 1 August, but the maximum humidity was measured on 2 August. The last five days showed high but declining values. Overall, the data coverage for humidity, measured by the LI-7500, was 68 %, which is the lowest of all the weather parameters. This could be due to precipitation and dew formation – unlike the CSAT3, the LI-7500 is not employed with wicks which speed up the water removal. Power limitations could also have affected the LI-7500 more than the CSAT3, since the IRGA requires a somewhat greater voltage.[2] Some of the quick drops in humidity, e.g. on 12 July and 3 August, are unphysical. The mean *relative* humidity was 77 %.

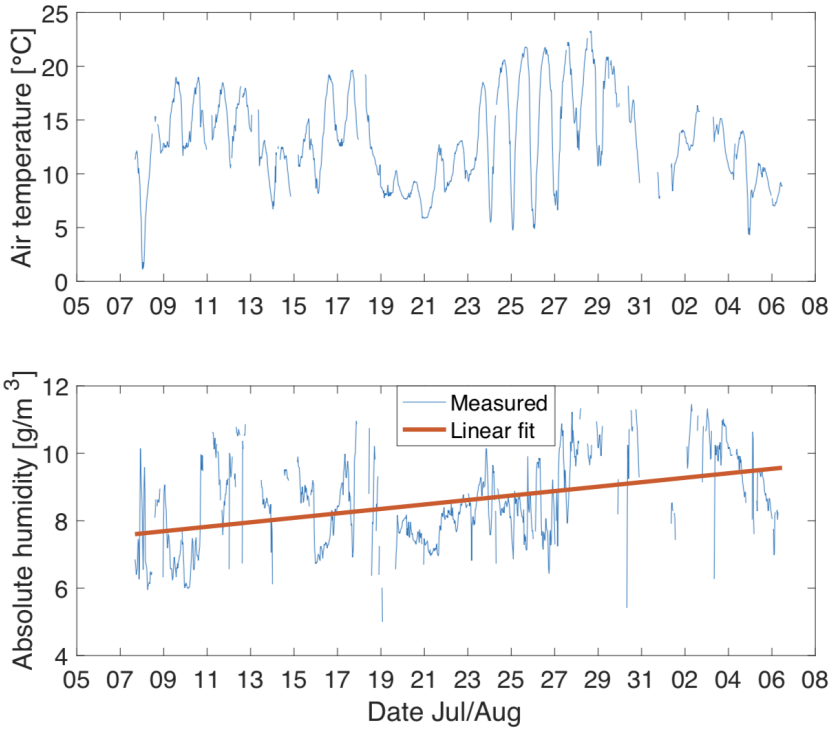

Figure 6.4: Time series of air temperature (top panel) and absolute humidity (lower panel) at the site for the whole measurement period.

6.2 Slow fluxes

We refer to radiation and soil heat transfer as *slow fluxes*, because they were sampled at f^{-1} = 1 min, as opposed to 20 Hz for the case of the turbulent fluxes. The data coverage

[2]Required direct current voltage for the LI-7500 is 10-30 V, whereas the CSAT3 needs only 10-16 V. See Campbell Scientific (2012) and LI-COR (2004b).

for all the slow fluxes was > 99 %, and missing data is found only on 8 and 13 July, when we were still in the field and disconnected the data logger briefly for technical purposes. No data was recorded during these interruptions.

6.2.1 Radiation

Midnight sun on our site lasted until 24 July, and on 6 August sunrise was around 2.30 and sunset at 22.10. Variations in theoretical maximum solar irradiance were small during the campaign, ranging from 953 W/m^2 on 7 July to 910 W/m^2 on 6 August (PVEducation, 2018).

In the upper panel of Fig. 6.5, we have plotted the raw time series of the four radiation components. Even though our site is located in the sub-Arctic, the summertime solar radiation (SD) at Iškoras resembles closely that of a mid-latitude station in spring or fall, with peak values exceeding 1000 W/m^2 on three days of the campaign, and 800 W/m^2 on 15 days. The maximum SD is 1084 W/m^2 and was recorded at 12.30 on 12 July. Values greater than the theoretical maximum are likely due to the reflection of shortwave radiation by bright cumulus clouds not in the way of the sun (Kipp & Zonen, 2018). The least sunny day was 14 July, when SD peaked at only 161 W/m^2, but also 19 and 31 July must have been quite cloudy, with SD maxima barely exceeding 200 W/m^2. Yet, the diurnal cycle is evident on all days for SD. This is not the case for the longwave components, which were almost constant on the days with less solar heating. During cloudy days, the upwelling (LU) and the downwelling (LD) longwave components balance each other, but otherwise LU > LD, which is reasonable. Days with longwave balance and little solar radiation seem to coincide with the dense data gaps found in the wind, temperature and humidity records described earlier in this chapter. Longwave minima are seen during the night on 8 July, when very low air temperatures were recorded. Not just LU, which depends on the ground surface temperature, but also LD, which is related to the effective sky temperature, reach their minima at this time. On the other hand, while LU is high at bright sunshine, average daily LD is in fact lower on clear days than otherwise – notice the gradual decline in LD from 19 to 25 July. This is because the absence of clouds on sunny days exposes the pyrgeometer to the cold, free atmosphere where diurnal heating is negligible.

SU is the reflected part of SD and peaks at exactly the same time as SU at only 162 W/m^2. The shortwave terms have a natural minimum at zero, whereas the longwave components have different diurnal minima – they are both lowest on clear nights, but for different reasons. LU simply follows the surface temperature, which is lowest when there are no clouds to re-emit the longwave radiation from the surface at nighttime. On the other hand, the effective sky temperature, which controls LD, is a complex function of the cloud situation (extent, type and base height), as well as the temperature and humidity profile between the surface and the clouds, if there are clouds. But in general, low nighttime LD coincide with low LU. The maximum in LD is found on 29 July, when there was bright sunshine but likely also low and warm cumulus clouds driven by a convective boundary layer.

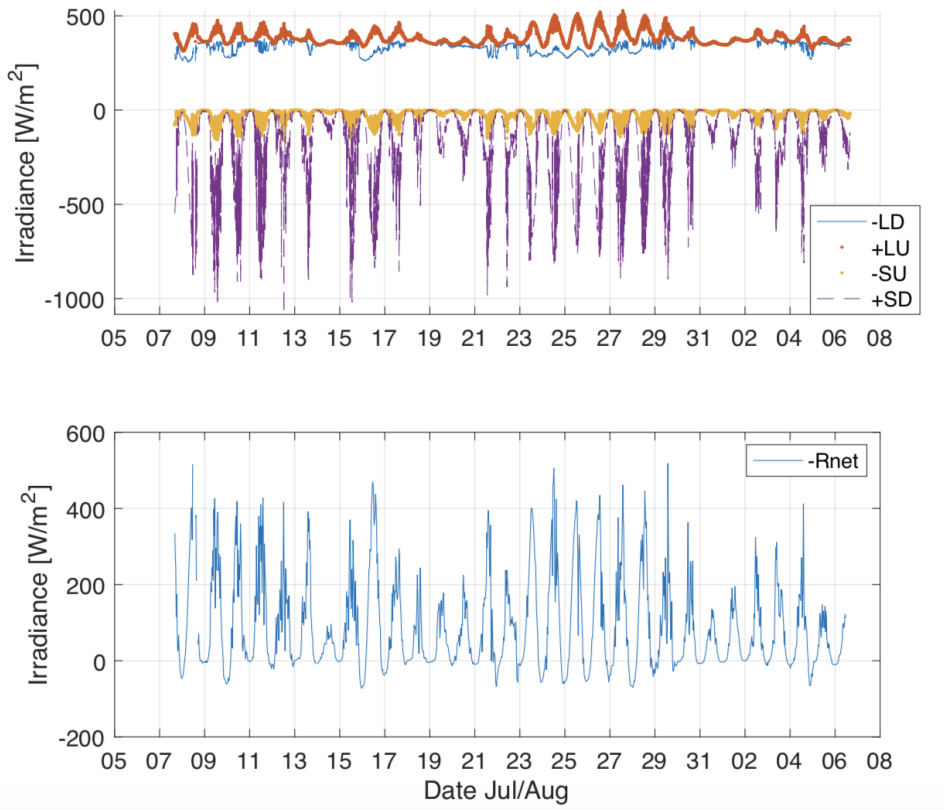

Figure 6.5: Top: Time series of the raw four radiation components. i.e. at 1-min sampling rate. S and L denote shortwave and longwave, and D and U indicate downwelling and upwelling, respectively. Fluxes going out of the surface are positive, but we have flipped LD and SU for illustrative purposes. Bottom: Time series of 30 min-averaged net radiation R_{net}, flipped for simplicity.

$-R_{net}$, as seen in the lower panel of Fig. 6.5 was typically about half of +SD during the day – they were in fact almost proportional (r = 0.98). $-R_{net} \gtrsim 400$ W/m^2 is seen on a majority of days, but not on 14, 17-20, 22 and 31 July, as well as most of the days in August. The raw $-R_{net}$ time series, not shown here, peaked at 811 W/m^2 on 12 July, coinciding with the +SD peak. However, this was a very transient maximum, and the 30-min averaged $-R_{net}$ is reduced by 50 % at this time. Rather, the 30-min $-R_{net}$ reached its highest values during the warm week and on 8 and 16 July. The overall maximum $-R_{net}$ was 518 W/m^2 and was measured at 13.45 on 29 July.

In Fig. 6.6a, the shortwave ensemble of all days is plotted together with the mean,

all presented as hourly averages. While peak values are similar to those of midlatitude stations in spring or autumn, it is clear from the daily duration of shortwave irradiance that we are indeed at a high latitude (compare to Fig. 2.2). As soon as SD reaches ~0, it starts increasing again upon the early sunrise, while it remain zero for many hours at lower latitudes. A large spread is seen between the days, which suggests that the cloud cover was in general quite significant during our campaign. Both SD and SU peak at noon or early in the afternoon. The average SD is 159 W/m^2, and SU has a mean of 24 W/m^2.

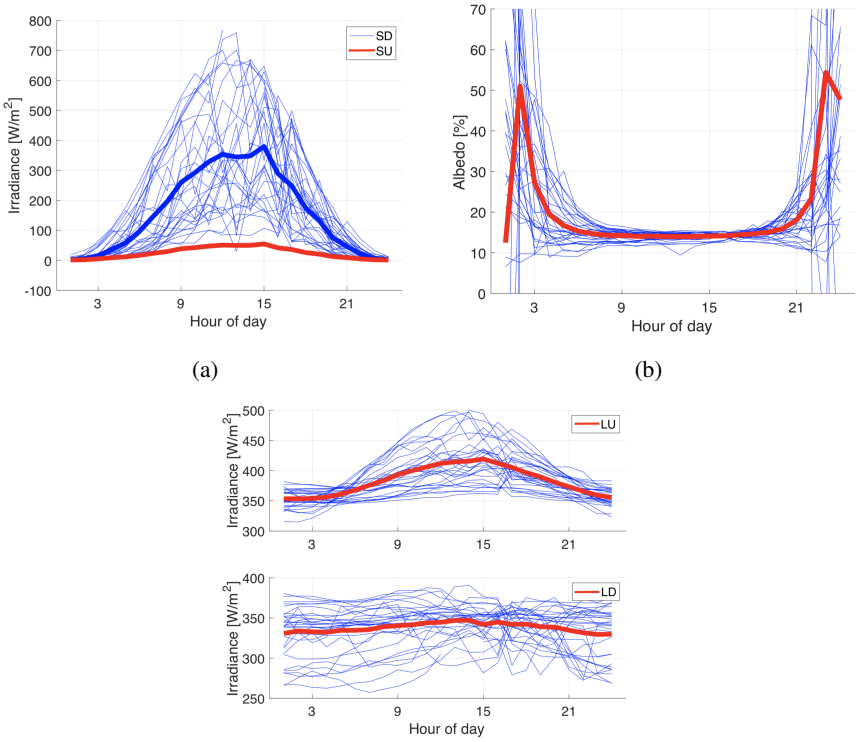

Figure 6.6: Diurnal course of a) shortwave radiation components, b) albedo and c) longwave components. Bold lines indicate averages for the whole campaign, and thin lines represent individual days. For SU only the average is given. All daytime fluxes are positive for simplicity.

Fig. 6.6b shows the diurnal course of albedo plotted against time of day. Some negative values are seen during the evening and night hours, which is due to a zero offset in the pyranometers (Kipp & Zonen, 2018). The mean albedo is 20 %, but this is affected by the unstable values during the night. Therefore it is more meaningful to calculate the median, which gives only 15 %. Albedo is almost constant during daytime, despite the

large spread in SD, which suggests that the reflectivity is independent of the cloud cover. The spread that we do see during the day is related mostly to surface moisture variability, causing albedo changes of ~ 25 percentage units relative to the median. As reviewed in Section 2.2, a parabolic diurnal signal in albedo is expected, due to higher reflectivity at low solar angles.

The diurnal course of LU and LD is seen in Fig. 6.6c. LU shows a strong diurnal signal, but is shifted by a few hours compared to SD, with maxima found around 3 p.m. and minima a little after midnight. The average LD is almost flat throughout the day, which is related to the two opposing effects of sunshine on LD, namely 1) heating of the atmosphere, which increases the signal, and 2) exposure to the free atmosphere, which lowers it. The greater spread in LD compared to LU is likely associated with variations in cloud base height and cloud cover in general. On the other hand, LD has a greater spread than LU, suggesting that the effective sky temperature varies more than the surface temperature.

Average LU is 383 W/m^2, which for $\epsilon = 0.962$[3] corresponds to a surface temperature of 16.2 °C, 3.1 °C higher than the mean air temperature.

Fig. 6.7 shows the air, surface and soil temperatures. The surface temperature (T_{surf}) is calculated from the Stefan-Boltzmann equation using an emissivity of 0.962, and the soil temperature (T_{soil}) is estimated from eq. 2.12 from the average surface temperature for the whole campaign, and with a thermal diffusivity of 0.12×10^{-6}m^{2}s^{-1} for saturated peat (Arya, 2001, p. 50). This gives a damping depth of 0.06 m and a time shift of 6.5 hours at 10 cm. The theoretical time shift, which is proportional to the depth, agreed very well with what we observed from the heat flux plate readings. T_{soil} follows the T_{surf} and is greater than the air temperature T_{air} most of the time. T_{soil} might be overestimated due to the seasonal lag, but at shallow depths such as 10 cm the offset is expected to be small.

T_{surf} is occasionally lower than T_{air} during the night, but otherwise $T_{surf} > T_{air}$, especially on days with strong solar heating. Nighttime minima are similar for T_{surf} and T_{air}, but daytime maxima are much higher for T_{surf}. Both temperatures are highest around 3 in the afternoon. The correlation coefficient is r = 0.87, and there seems to be a quadratic relationship between the temperatures. T_{surf} departs relatively more than usual from T_{air} on 21 July and 4 August, but this is likely due to northerly winds on these days, which was shown in Fig. 6.2. Cold air advection in high light would limit the heating of the atmosphere from a warm surface.

[3] $\epsilon = 0.962$ is the emissivity provided by Foken (2008b, p. 13) for wet fine sand.

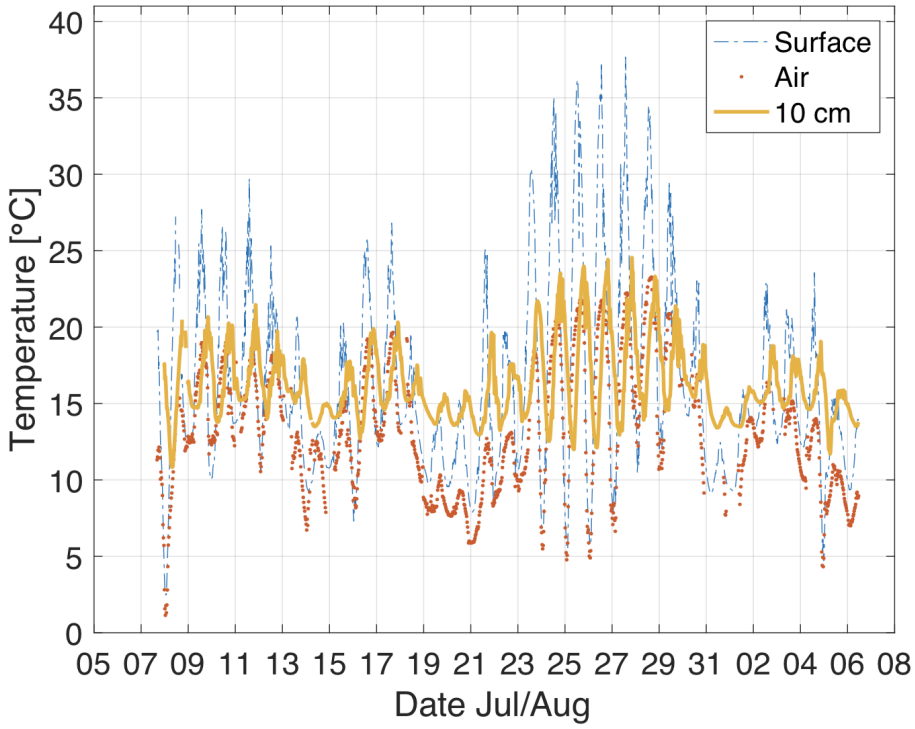

Figure 6.7: Time series of air, surface and soil temperatures.

6.2.2 Soil heat fluxes

Time series of the heat flux plate readings at 20 cm (SH20) and 10 cm (SH10) are given in the top panel of Fig. 6.8. Since they are measured rather deep, we refer to them as soil heat fluxes instead of ground heat fluxes. Daytime soil heat flux values are ~ 10 % of the radiative and turbulent fluxes outlined above. Total maximum of SH20 is 23 W/m^2, whereas SH10 peaks at 31 W/m^2. Meanwhile, the turbulent heat fluxes frequently exceed 100 and 150 W/m^2, and three of the radiative terms are on the order of 300-500 W/m^2 during the day. Reflected shortwave radiation SU is similar in magnitude to the SH fluxes, but even SU reaches 100 W/m^2 at bright sunshine. SH10 has a mean of 7 W/m^2, whereas SH20 is in fact greater, with an average of 9 W/m^2. For the upper sensor, this corresponds to 8.0 % of the net radiation, when considering the whole campaign.

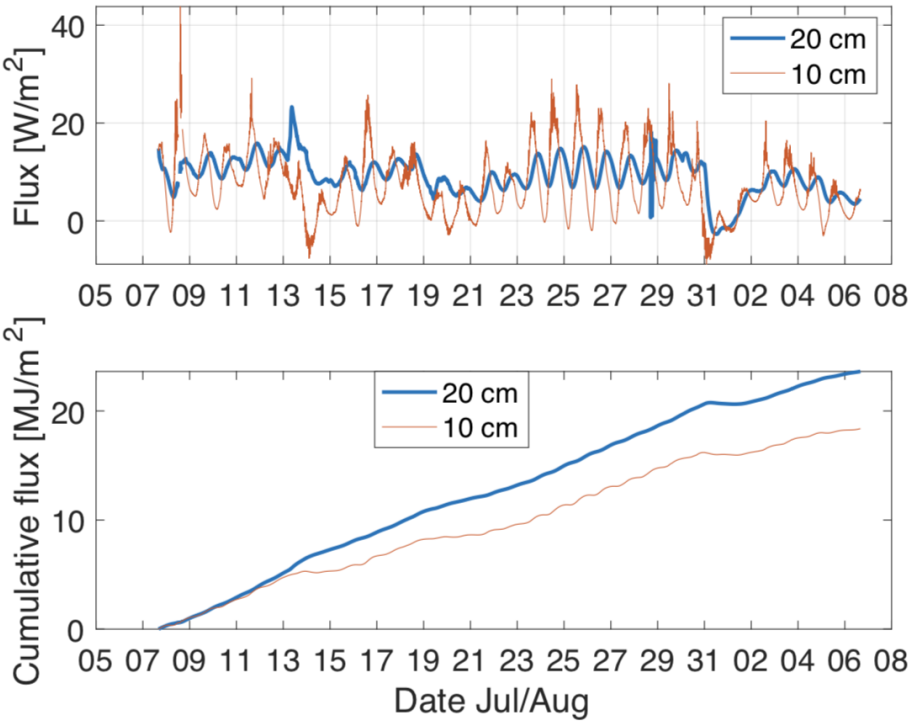

Figure 6.8: Time series of instantaneous (top) and cumulative (bottom) soil heat fluxes measured at 20 cm and 10 cm for the whole campaign, sampled every 1 min. Positive fluxes are directed away from the surface.

SH20 largely follows SH10, but its amplitude is 2-3 times greater than that of SH20, and a certain time delay in the deeper soil is seen upon close inspection. SH10 peaks around 3 p.m., i.e. at roughly the same time as the surface temperature, whereas SH20 maxima are found at 9 p.m.

The diurnal signal is clearly seen on most of the days in both fluxes, and the time evolution is much smoother than in the radiative fluxes. SH10 is somewhat noisy at most daily maxima, but otherwise the measured soil heat transfer is quite regular. Both fluxes are nearly always positive, but negative SH10 values are seen briefly on several days, primarily during the night but also at daytime on a few days. SH20 is negative only on 31 July and 1 August, after a strong decrease in both readings.
Strange flux behaviour is found on 13 July, when SH20 jumps to > 20 W/m^2 without any foreshadowing in the shallower SH10. SH10 is also more affected by noise at this time. This, as well as the spike in SH10 on 8 July, is likely due to a technical malfunction, related to the brief measurement breaks around on these days. SH20 is subject to strong

noise on 29 July, which seems unrelated to surface processes.
The overall time evolution of SH10 and SH20 is consistent with radiation and air temperature data, with a strong decrease on the first day of the campaign, low fluxes around 14, 20 and 31 July and a pronounced diurnal cycle between 23 and 30 July. On the other hand, the steep drop on 31 July is unexpected, because minimum surface temperatures as seen in Fig. 6.7 are several °C lower on 8 July than on this day. This might be related to the heat storage in the soil, which can induce large heat vertical gradients if suddenly the surface is cooled by for instance frontal weather. Based on observations from the Iškoras mountain station (yr.no, 2018a) and our own experience during the campaign, the days prior to 7 July were quite cool and windy – maximum air temperature on e.g. 5 July was only 4.2 °C. On the other hand, the days before 31 July were very warm. Thus, soil temperatures might have been low on 8 July, and high on 31 July, which could explain the stronger flux signal on the latter day.
Heat is accumulated at both levels at rates of 0.7-0.9 MJ/m^{2}d, as shown in the lower panel of Fig. 6.8. Cumulative fluxes are largely parallell, but the deeper soil receives more heat over time, according to the measurements. Around 13, 19 and 31 July, but also from 4 August through the end of the campaign, SH20 exceeds SH10, and this energy surplus appears to stay in the deep soil. This would imply a gradual cooling of the upper soil layer during the campaign, which is very unlikely. The timing of these departures coincides well with the days of low atmospheric pressure (Fig. 6.2) and likely rainfall, which suggests that SH10 is underestimated during and after rain events, likely due to the different thermal properties of moist soil. If the ground water table was between 10 and 20 cm after rain events, the lower soil would experience higher heat capacity but also a higher thermal conductivity. Without soil moisture and temperature measurements it is difficult to assess why the deeper soil supposedly gained more heat, but a similar pattern was documented by Halliwell et al. (1991). Neglecting these effects, we find that the true heat gain was probably very similar at 10 and 20 cm, which leads to the conclusion that only the deeper soil (> 20 cm) experienced long-term warming during the campaign. While the active layer thickness was not measured for this study, Christiansen[4] measured a thaw depth of about 45 cm in mid September at the same site. At any rate, substantial soil heat uptake in summertime is typical in permafrost regions (McFadden et al., 1998).

SH10 consumes on average only 8.0 % of the net radiation, and daytime maxima represent even less (6 %). Other studies from the Arctic and sub-Arctic during summer, e.g. Halliwell and Rouse (1987); Westermann et al. (2009), have reported 2-3 times greater fractions of $-R_{net}$ partitioned into the ground heat flux, using soil temperature and moisture profiles. McFadden et al. (1998) found midday ground heat fluxes of up to 33 % of net radiation, while daily sums ranged from 1 to 3 MJ/m^{2}d, across various vegetation types on the Alaskan tundra. It is therefore likely that the deep placements of our soil heat flux plates, and possibly also the effects of moisture, which we have not considered, has led to a large (> 50 %) underestimation of the ground heat flux at the surface. The effect of greater thermal conductivity in the sensor (0.76 W/mK) than in the soil (between 0.06 W/mK and 0.5 W/mK) would mitigate placement errors, but since the soil must have been quite moist during the whole campaign, we do not expect this to compensate for the

[4]Casper Tai Christiansen, personal communication

underestimation.

6.3 Turbulent fluxes

The footprint climatology from the methods described in Section 5.4 is shown in Fig. 6.9, and indicates that the palsa complex covers about 80 % of the footprint, which is considered sufficient. However, the 90 % contour line contains a more vegetated mire area without permafrost, which could influence fluxes during northerly wind. While the instantaneous footprint would increase in stable (nighttime) conditions, we note that the wind speed at our site, which was generally greater during the day than during the night, would act to balance such changes.

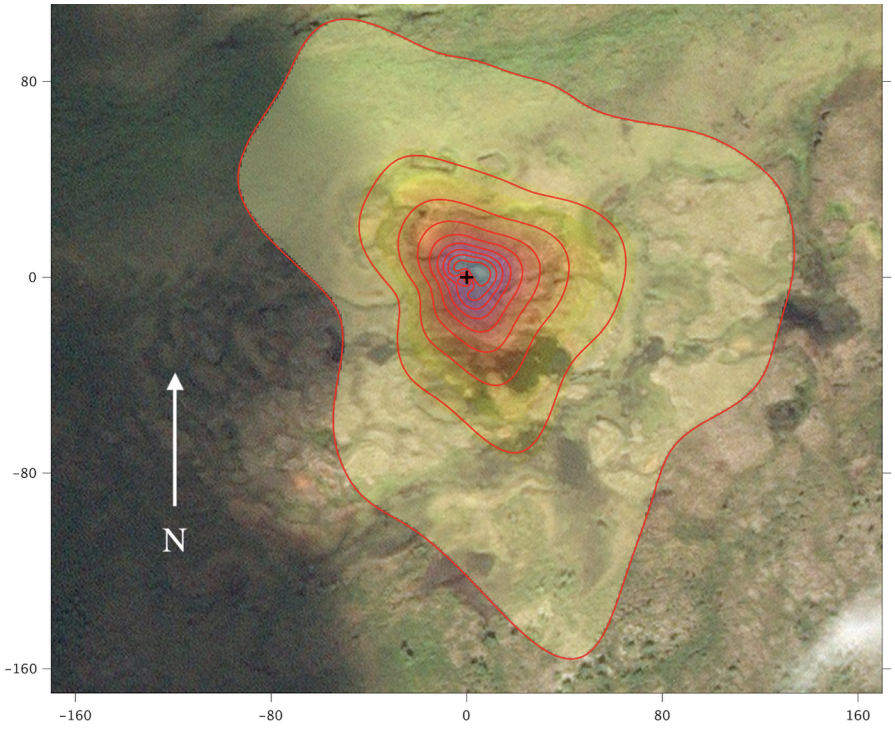

Figure 6.9: Footprint climatology of the eddy covariance tower for the whole campaign. Contour lines represent from 90 % to 10 % fetch area, in 10 % steps, and axis ticks are in meters. The flux tower is indicated by a cross.

Fig. 6.10 shows time series of the three turbulent fluxes, that is, sensible (SH) and latent heat (LH) and the net ecosystem exchange of CO_2 (NEE). The data coverage was 66 % for SH and 57 % for LH. Both LH and SH largely follow the net radiation, with correlation coefficients of 0.85-0.87. Some of the remaining differences between SH and

LH are perhaps controlled by the wind speed. This is seen on for instance 9 and 16 July, when there were relatively high winds (U > 4 m/s) and strong net radiation ($-R_{net}$ > 400 W/m^2). In these conditions, LH exceeds SH, whereas they are more equal during the warm week starting on 23 July. However, recall that SH and LH would probably have been 2-5 % greater if the Moore correction had been applied, as mentioned in Section 5.2.2.

Mean LH overall is 52 W/m^2, almost twice the mean of SH (27 W/m^2), which means that on average 58 % and 30 % of the net radiation were consumed by the latent and sensible heat, respectively. However, upon inspection of the data we find that the data gaps are not evenly distributed over the day – missing data is more frequent at nighttime, which leads to a slight bias when calculating the mean. Correcting for this effect, the new averages become 47 W/m^2 for LH and 22 W/m^2 for SH, or 53 % and 25 % of the net radiation.

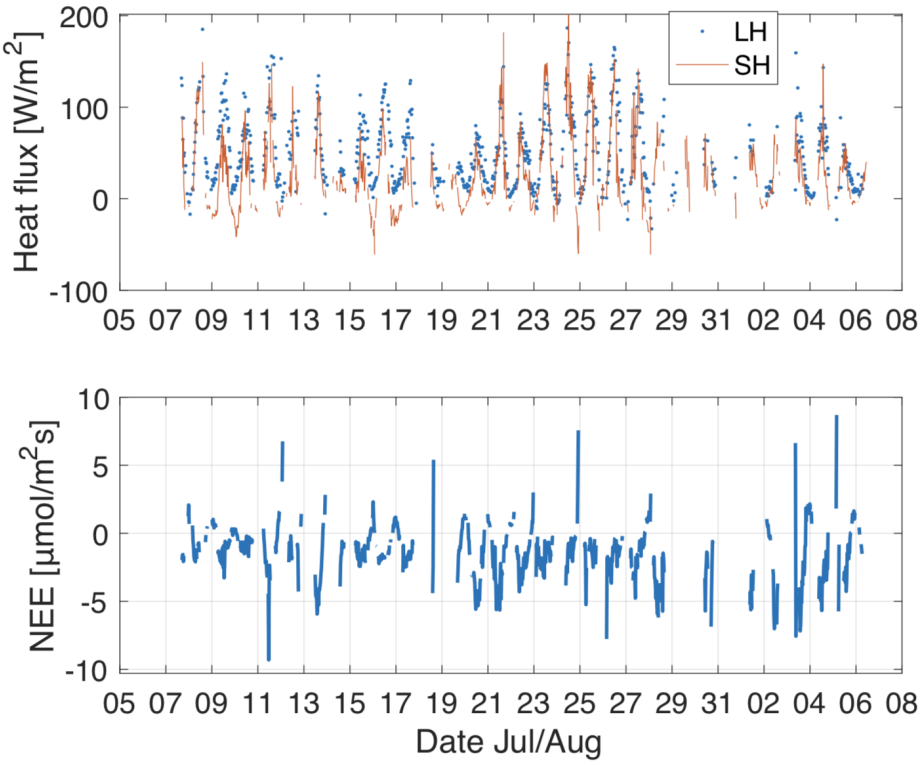

Figure 6.10: Time series of sensible and latent heat fluxes (upper panel) and the net ecosystem exchange of CO_2 (lower panel). Positive fluxes are out of the surface, and negative fluxes indicate an uptake of heat/CO_2 by the ground.

The difference between LH and SH is reasonable, because the turbulent heat release

from wetland surfaces is typically dominated by evaporation in summertime (e.g. Siedlecki et al., 2016; Aurela et al., 2001). SH and LH peak on 24 July, with maxima of 202 and 187 W/m^2, respectively. Negative LH values, which indicate dew deposition, are seen on a few nights, but this is measured less than 2 % of the time, whereas sensible cooling affects almost every night and represents 20 % of the time series.

Large data gaps – 50 % in total – make the NEE time series difficult to interpret. However, NEE is clearly negative most of the time, indicating carbon uptake, and correlates negatively with $-R_{net}$ (r = –0.44). The diurnal NEE amplitude increases during the campaign, which can hardly be explained by the air temperature or radiation data. On the other hand, while there was no positive trend in the estimated 10 cm soil temperature seen in Fig. 6.7, the deeper soil must have been warming, which could have led to both greater photosynthesis (i.e., negative NEE) and greater soil respiration (positive NEE) (Heinonsalo and Pumpanen, 2014). However, the gradual NEE increase might also be related, perhaps more importantly, to vegetation growth, as was found by Nykänen et al. (2003) during summer on a palsa mire in northern Finland.

Average NEE for the whole campaign was –1.5 μmol/m^{2}s. That would correspond to a total CO_2-carbon (C) uptake of 45.4 g/m^2 over the 31 days, but since the data gaps are found disproportionately during the night when NEE > 0, a more realistic estimate is –1.1 μmol/m^{2}s on average, and an uptake 34.0 g/m^2. This suggests that photosynthesis at our site during the 2017 growing season exceeded respiration, despite ongoing permafrost thaw, which is in good agreement with previous eddy-covariance studies from similar ecosystems. Christensen et al. (2012) reported a growing season NEE of ~ 1-2 g C/m^{2}d between 2001 and 2008 on a palsa mire in sub-Arctic Sweden, but they observed a general increase in summertime C uptake over these years. In northeastern Siberia, Euskirchen et al. (2017) measured a daily C accumulation of ~ 1-3 g C/m^2 between June and August during the years 2013-2015 at a thawing permafrost site, but their area was vegetated by shrubs up to 1 m, which could explain higher productivity at their site relative to ours. On the other hand, while the annual CO_2 budget measured by Christensen et al. (2012) was negative, corresponding to a C uptake, the annual release of methane on the same mire was positive and substantial. In contrast, Cassidy et al. (2016) found positive CO_2 fluxes, though low, from a degrading permafrost site in northern Canada during the 2014 growing season, but these fluxes originated from a so-called retrogressive thaw slump. Such slumps indicate very rapid erosion (French, 1976, p. 120) and are, when active, associated with no established vegetation (Lantuit and Pollard, 2008). The thaw slump considered by Cassidy et al. (2016) was indeed poorly vegetated, which would limit carbon uptake. The vegetation on our site, however, contained various productive plants such as sedges and low shrubs up to ~ 20 cm tall, though patches of exposed peat and lichen were also common.

In Fig. 6.11a we have spatially partitioned the NEE and R_{net} data into four categories, where 'N' represents measurements taken during northerly wind (NW-NE), 'S' during southerly wind (SW-SE) and so on. Two points can be made from this plot. First, light saturation seems to be reached around $-R_{net}$ = 200 W/m^2 regardless of the wind direction, well before peak intensity, as expected from e.g. Munn (1966, p. 30). This corresponds to a solar irradiance of about 350 W/m^2 – recall the very linear relationship between the

net all-wave radiation and solar radiation.

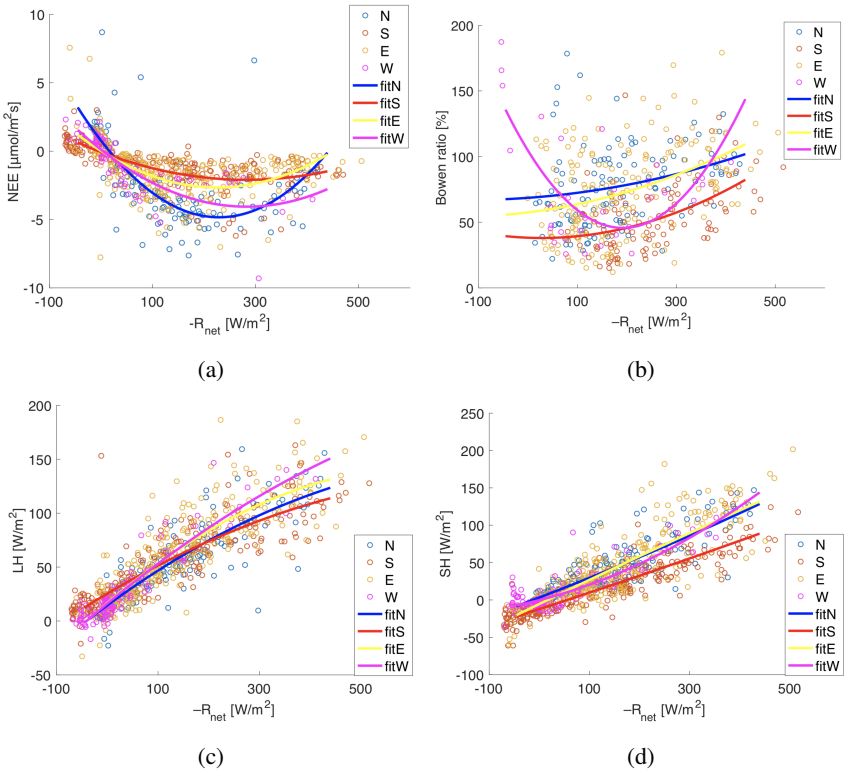

Figure 6.11: Scatter plots of net radiation against a) NEE, b) Bowen ratio, c) LH and d) SH. Each of the four variables have been split into four groups according to the wind direction, where 'N' denotes wind from the northerly sector, 'S' from the southerly and so on. Least square's regression lines are of second degree.

Second, Fig. 6.11a suggests that the ecosystem response to solar radiation is not the same for all wind directions. In fact, northerly winds are associated with higher photosynthesis than are southerly winds. The difference is quite pronounced, with nearly 3 times greater mean uptake for the northerly group than the southerly. Systematic differences in weather conditions depending on wind regime could have contributed to this effect, but we find no evidence to support that argument. The radiation is largely independent of wind direction, except during westerly winds, which were recorded primarily during the night and coincided with dim light. Air temperature and wind speed are higher during southerly winds, which would promote the opposite pattern, i.e. *lower* uptake for northerly winds. Therefore, the differences in carbon gain could be related to the flux footprint, which is greener towards the north of the tower than on what is primarily palsa mire elsewhere. The green area is mostly beyond the 80 % footprint

contour and strictly speaking not part of the palsa mire we are interested in, but our total uptake estimates are nevertheless typical of thawing permafrost areas.

Photosynthesis in the thaw ponds observed to the south-southeast of the station is expected to be particularly low. At low or negative radiation, +NEE is somewhat greater for the northerly case, which adds confidence to our conclusion – recall that respiration increases with photosynthesis. This indicates that our measured carbon fluxes are sensitive to the footprint, and suggests that the eddy-covariance measurements are of good quality. A vegetation analysis within the footprint would strengthen this argument, but that is beyond the scope of this study.

Similar plots are made for LH and SH in Fig. 6.11c and 6.11d. It is clear that the heat fluxes show a much more linear dependence on the radiation, regardless of the wind direction. Obviously, light saturation does not apply to the heat budget as it does to the NEE. Systematic differences between wind directions are not as pronounced as for NEE – westerly winds are associated with somewhat greater LH at high radiation, but this is less significant since very few daytime readings of westerly wind were recorded at all during the campaign. However, SH appears to be lower in southerly winds than otherwise, which is likely more related to the generally higher temperature at such winds (15.0 °C in southerly winds compared to 13.1 °C overall). At daytime, warm air advection would act to limit the vertical temperature gradient in the surface layer and thereby limit SH. This leads us to the Bowen ratio β (SH/LH), which was calculated only for LH, SH > 10 W/m^2. On Arctic coastal sites, β is known to increase during onshore advection (Ohmura, 1982) in summertime, and greater ratios were indeed found at northerly winds for our site, as seen in Fig. 6.11b. This is mostly due to the SH dependence on wind direction. While our palsa mire is ~ 50 km from the nearest fjord and > 100 km from the ocean, winds blowing from the north did bring colder air (mean temperature 12 °C in northerly winds), which suggests that coastal effects may well influence continental regions – the absolute humidity was also somewhat greater at northerly winds (not shown). Different flux footprints can hardly explain the observed variability in β. Finally, the strong curvature in the westerly wind regression line is likely not very significant, since westerly wind was rare at daytime.

Average and individual diurnal courses of latent heat (LH), sensible heat (SH), net ecosystem exchange (NEE) of CO_2 and the Bowen ratio are plotted in Fig. 6.12. The energy fluxes do not vanish at nighttime. Between 21 in the evening and 03 in the morning, mean LH is +10 W/m^2, but SH is –10 W/m^2. Otherwise they are both mostly positive, with average maxima of 95 W/m^2 and 66 W/m^2, found at midday.

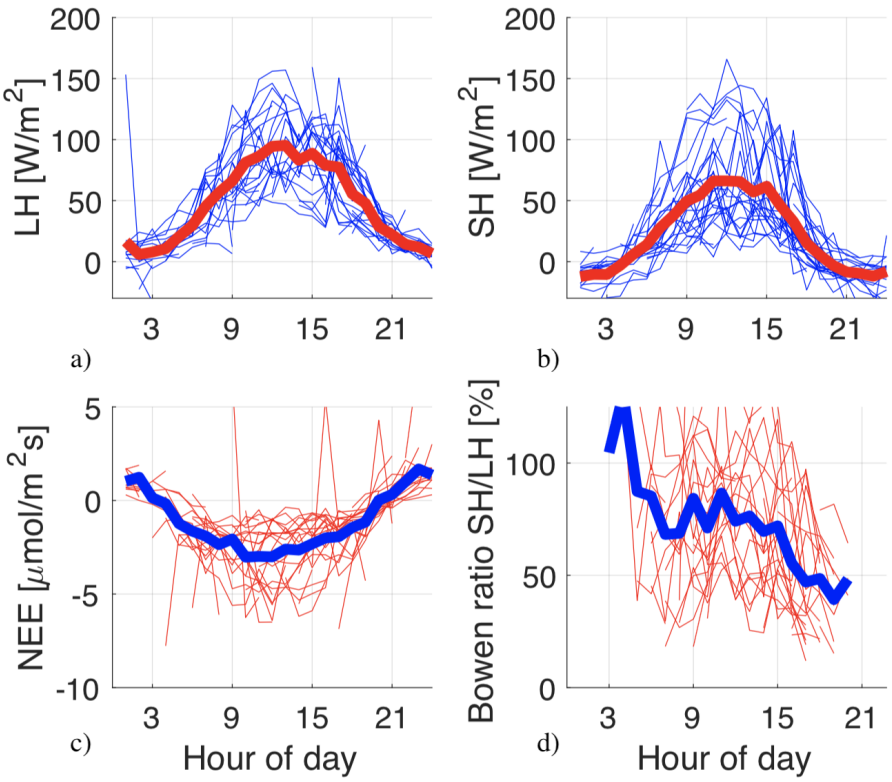

Figure 6.12: Diurnal course of a) latent heat (LH), b) sensible heat (SH), c) net ecosystem exchange (NEE) of CO_2 and d) Bowen ratio. Bold lines indicate averages for the whole campaign, and thin lines represent individual days, all from hourly-averaged data. Positive fluxes correspond to a release from the ground to the atmosphere.

All fluxes show a strong diurnal pattern, but LH and SH are skewed towards the afternoon, especially LH. Peak CO_2 uptake is found at 10-11 in the morning on average, which could be related to the light saturation as we have already discussed. However, like LH and SH, NEE is largely constant in the early afternoon. Between 8 p.m. and 4 a.m., NEE is positive, indicating respiratory carbon release. Average maximum nighttime NEE is +1.7 μmol/m^{2}s.

The average Bowen ratio β is 70 %, and the mean at noontime is 74 %. At daytime β follows a certain diurnal cycle, suggesting that SH becomes increasingly important until midday. There is also a decline in β over the whole day, which indicates that LH is somewhat delayed relative to SH. Our measured Bowen ratios are typical of the growing season in sub-Arctic ecosystems, where evaporation is limited by sunshine rather than by soil moisture. Aurela et al. (2001) report a daytime mean Bowen ratio of 76 % during the

1997 summer on a mire in northern Finland, whereas Lafleur et al. (1997) found $\beta = 0.46$ in summertime on a boreal peatland in Canada.

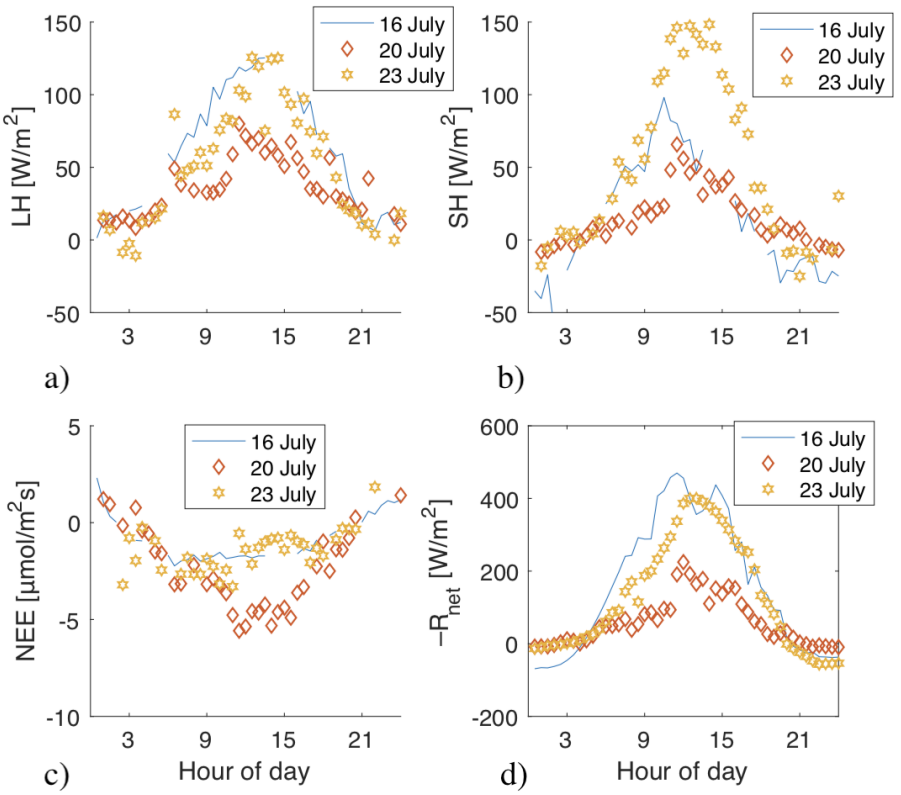

Figure 6.13: Diurnal course of a) latent heat, b) sensible heat, c) net ecosystem exchange of CO_2 and d) net radiation, on 20, 21 and 23 July.

To illuminate further how the fluxes depend on radiation, we have plotted in Fig. 6.13 the diurnal courses for three selected days with various degrees of sunlight. On 16 and 23 July, the net radiation exceeded 400 W/m^2, which indicates relatively strong solar intensity. LH and SH are both higher here than on 20 July, when there was a cloud cover and only half as much net irradiance. Differences between SH and LH are in part associated with the wind speed and direction, as already discussed. On the other hand, the greatest [–NEE] here is seen not on the two sunny days, but on 20 July, which was one of the coldest days of the whole campaign. This is likely related to light saturation, which as already mentioned was reached at $-R_{net} \approx 200$ W/m^2. Specifically, at $-R_{net} >$ 200 W/m^2, photosynthesis does not respond much to increased radiation. So there must

have been other factors controlling the day-to-day variability in NEE, perhaps especially the wind direction, which was indeed N-NW on 20 July and S-E on the two warmer days. This could also have contributed to the observed long-term increase in the diurnal NEE amplitude during the campaign, since southerly winds were absent after 31 August.

6.3.1 Surface energy balance

Energy balance at the surface does not by itself imply good quality in the turbulent fluxes (Foken, 2008b, p. 104). However, the surface energy balance has historically been used to verify the eddy-covariance method (Wilson et al., 2002), and should provide at least some information on the performance of this technique, even though the non-turbulent fluxes may also contain errors.

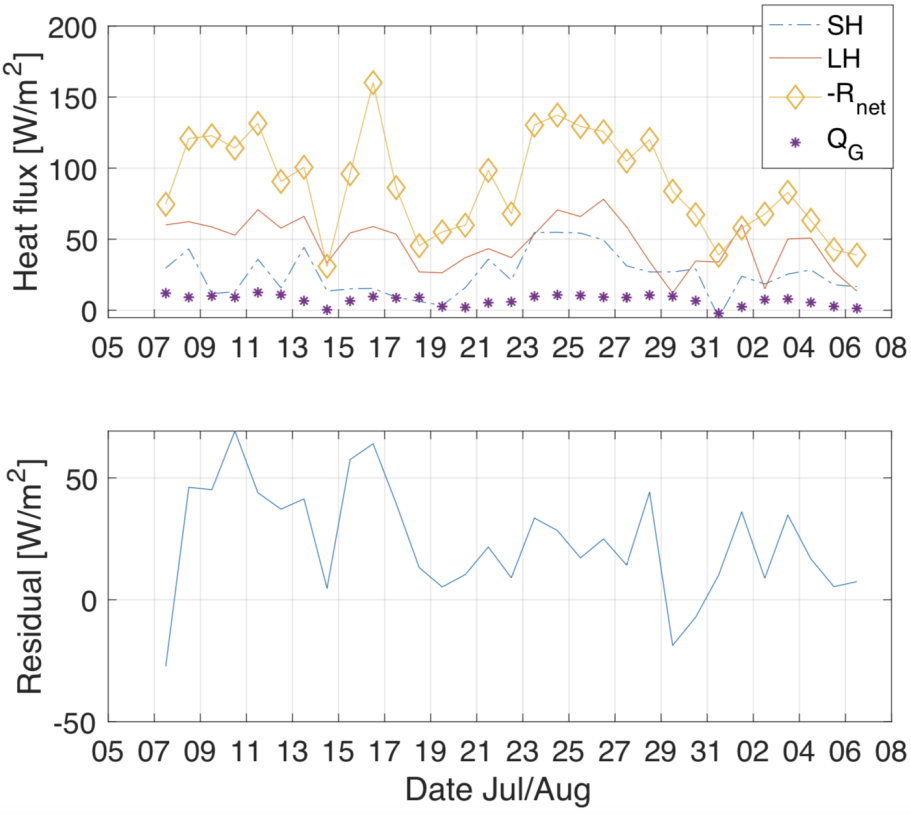

Figure 6.14: Time series of average daily energy fluxes (upper panel) and residual (lower panel), i.e. one value per day, for the whole campaign. 7 July and 6 August are incomplete days.

The monthly course of all heat fluxes and the residual $Res = -Rnet - Q_g - SH - LH$,

where Q_g is the soil heat flux at 10 cm, is shown in Fig. 6.14. The residual largely follows $-R_{net}$ (r = 0.61), especially in the first half of the campaign. Changes in $-R_{net}$ are sometimes reflected in the turbulent fluxes, and the increase in $-R_{net}$ on 22 July coincides with elevated SH, LH and Q_G.

From 28 July through 2 August, data coverage for the turbulent fluxes is sparse, especially the latent heat which is missing more than 80 % of the data during this week. The days from 21 to 29 July had relatively good data quality, and show a residual of 20-30 % of $-R_{net}$.

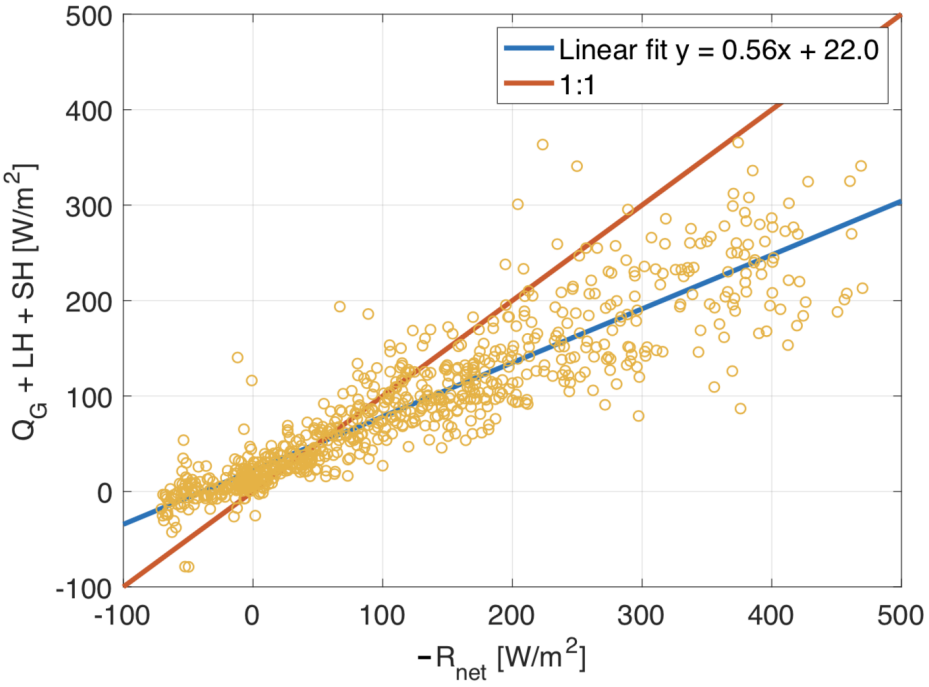

Figure 6.15: Scatter plot of net radiation ($-R_{net}$) vs. nonradiative fluxes. The 1:1 line corresponds to surface energy balance closure, whereas the regression is a least square's fit for the actual data.

It is perhaps more meaningful to evaluate the surface energy balance (SEB) using scatter plots, without any time component. This is shown in Fig. 6.15. A perfectly closed energy balance would produce the 1:1 line with zero scatter, but the least square's fit for our data has a slope of only 0.56. Thus, $-R_{net}$ is in general greater than the sum of Q_G, LH and SH during the day, and more negative during the night. The nighttime balance is especially poor, when non-radiative fluxes are close to zero whereas $-R_{net}$ is strongly negative. However, while the scatter appears to increase for $-R_{net} > 200$ W/m^2, the overall distribution follows the regression line quite well (r = 0.90), which suggests that there are

systematic errors in one or more of the fluxes.

Fortunately, most studies arrive at the same conclusion – experimental data are unable to verify the SEB equation, and $-R_{net}$ is usually found to be greater than the non-radiative fluxes (Foken, 2008a). Some of the imbalance would be accounted for by the Moore correction, which was not applied, but this can hardly explain such a large mismatch. Therefore, we propose three main reasons for the imbalance in our campaign:

1) Systematic errors in the CNR 1 radiometer, discussed in Section 4.2.3. The window heating offset at bright sunshine in the upward-facing CG 3 pyrgeometer, which measures downwelling longwave radiation, is expected to cause errors of +15-20 W/m^2 during solar radiation of 700 W/m^2. This translates to ~5 % of the net radiation on clear days. Similarly, nighttime shortwave measurements may suffer from far infrared cooling, which can lead to negative offsets down to –15 W/m^2 during clear nights. Both of these effects would contribute to the observed mismatch seen in Fig. 6.15. In contrast, Foken (2008a) argues that the net radiation is *not* overestimated and can not explain the lack of SEB closure.

2) Shortcomings of the eddy-covariance (EC) method. Despite all the corrections discussed in Chapter 5, EC performance is reduced by certain meteorological effects which cannot easily be dealt with. These are primarily advection and large eddies. Oncley et al. (2007) reported a certain improvement in energy balance closure when advection was estimated using 10 EC towers, which indicates that CO_2 can also be advected below an EC system. However, such instrumentation was not available for our study, and Foken (2008b, pp. 116-117) argues that the storage term – which is included by TK3 in the NEE calculation – together the WPL correction should account for at least some of the advective fluxes. The contribution of large eddies can be addressed using ogives, which were detailed in Section 5.3.3. Ogives of SH, LH and NEE for the period between 13 July and 6 August, excluding the first week of our campaign, are shown in Fig. 6.16. The sign is conserved in the spectral calculations, so that positive ogives at low frequencies indicate positive fluxes, and negative ogives indicate negative fluxes. Ogive convergence can be evaluated objectively using thresholds, which was done very successfully by Aalstad (2015) on Svalbard. He found a clear relationship between ogive convergence and atmospheric stability, with stable conditions being the less well-behaved. In this study, however, the ogives are presented for illustrative purposes only.

A large part of the ogives, perhaps the majority for the case of LH and NEE, appear not to converge at low frequencies. This could be due to longwave eddies, but it is likely also related to other disturbing factors such as flow distortion (Sievers et al., 2015). However, it is clear that one 'S-shaped' trajectory, indicating convergence, is favoured for all three fluxes. Nighttime ogives, i.e. negative SH, positive NEE and low/negative LH, are less convergent than are daytime ogives, which suggests that longwave eddies were more common in stable conditions. This is also supported by the slope of the distribution in Fig. 6.15, which is particularly poor at night.

Thus, all our eddy fluxes are likely underestimated, as others have found (e.g. Foken et al. (2006)), but this applies especially to nighttime conditions, which is also consistent with the literature (Aubinet et al., 2012). Unfortunately, though there have been attempts,

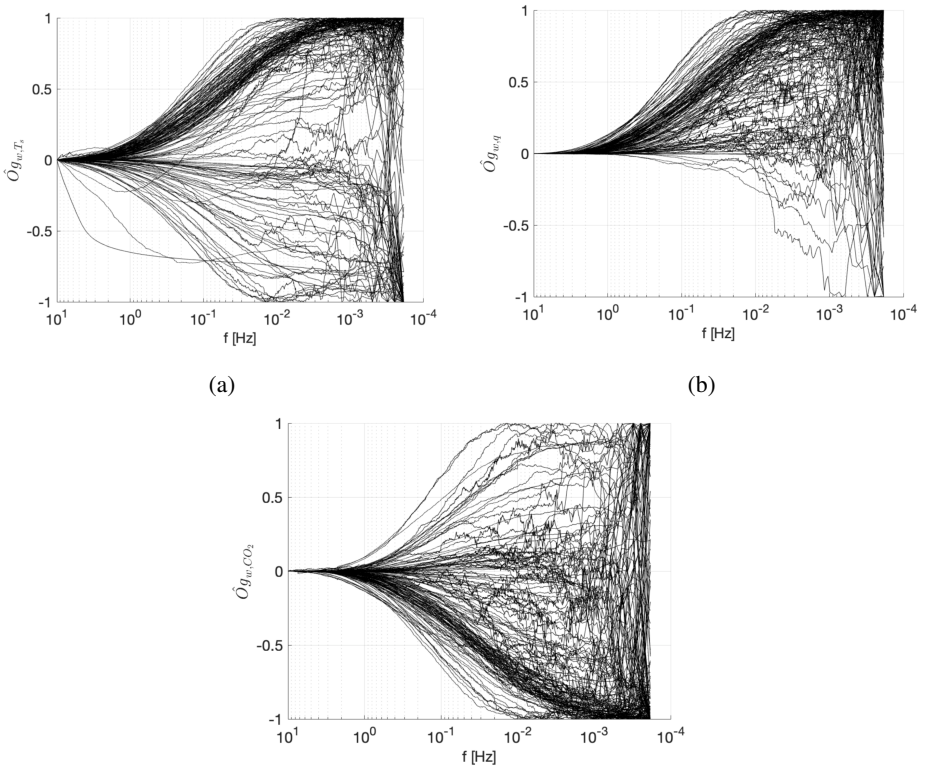

Figure 6.16: Ogives of a) sensible heat flux, b) latent heat flux and c) CO_2 flux, all for the period 13 July-6 August 2017.

there is no accepted method to include the contribution of large atmospheric structures (Massman and Clement, 2004). One natural solution would be to increase the averaging time to for instance an hour or more, but this can introduce non-stationarity and advection to the eddy covariance, as pointed out by e.g. (Malhi et al., 2004), which is perhaps more problematic.

3) Underestimated and shifted ground heat flux. As already mentioned, our ground heat flux measurements are hardly representative of the surface, due to the deep placement of the HFP01 sensors. However, using heat transfer theory, we can calculate a more realistic surface ground heat flux based on the 10 cm temperature, the surface temperature and the 10 cm flux:

$$Q_G(0) = Q_G(-z) + \frac{C_S \mid \Delta z \mid [\overline{T(t_2)} - \overline{T(t_1)}]}{t_2 - t_1} \tag{6.1}$$

where the temperature and flux data are 1-min, but Q_G is averaged over 30 min. This equation was derived in Section 2.3, and the second term represents the change in heat storage above the 10 cm level. For the volumetric soil heat capacity C_S we have used $4.02 \cdot 10^6$, which is the value given for wet peat by Arya (2001, p. 50).

Replacing SH10 by this modified flux gives a better slope than in Fig. 6.15, but a very large spread, likely because moisture changes would greatly modify the soil heat capacity. To overcome some of the adverse affects of moisture, we applied a digital filter[5] to the raw estimate. The resulting raw and filtered Q_G and the new SEB are shown in Fig. 6.17. While the raw (30-min) Q_G is clearly erroneous, the filtered estimate looks quite realistic in terms of the diurnal phase and the time development, but ranging from –215 W/m^2 to 250 W/m^2 it is still very much overestimated – the resulting regression line has a slope of 1.05. This is probably again related to the soil thermal properties, since we have assumed wet peat during the whole campaign, while dry peat has a much lower (~85 ‰) heat capacity. In any event, Fig. 6.17 indicates that the SEB is sensitive to improved estimates of the soil heat flux.

[5]The running mean filter in MATLAB can be described by

$$y(n) = \frac{1}{b}[x(n) + x(n-1) + \ldots + x(n-b+1)] \tag{6.2}$$

where x is the input data. In our case, the window size b was set at 10.

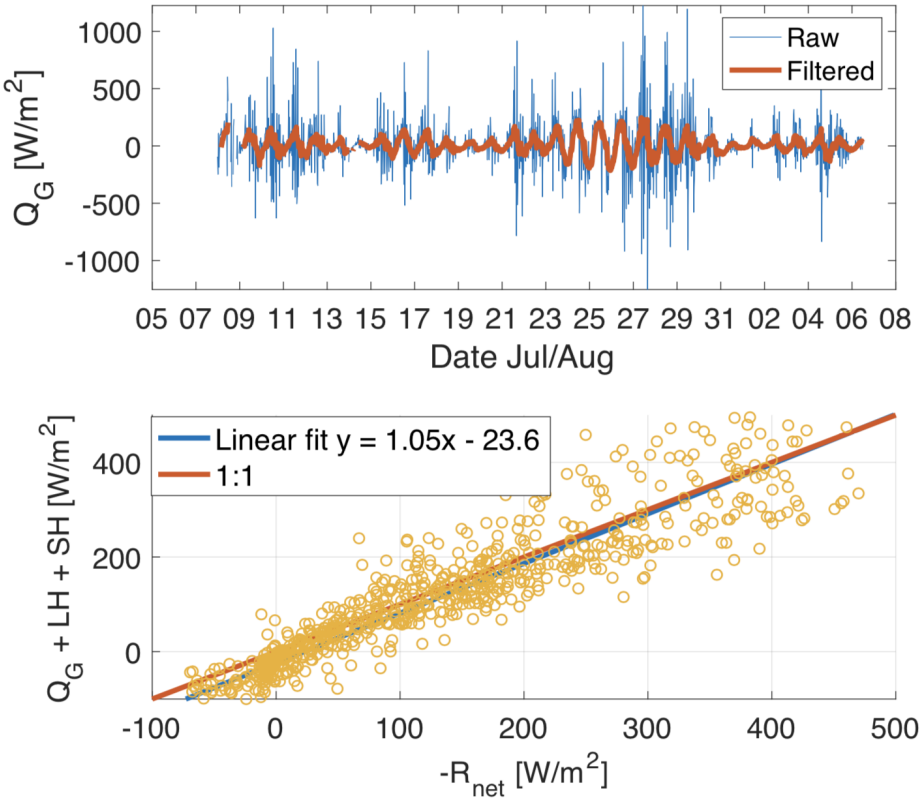

Figure 6.17: Top: Time series of estimated raw and filtered ground heat flux at the surface. Bottom: Scatter of net radiation vs. turbulent fluxes and filtered Q_G

Chapter 7

Summary and outlook

We have presented measurements of surface fluxes taken between 7 July and 6 August 2017, on a palsa mire near the Iškoras mountain in Finnmark, northern Norway. Palsa mires are a particular landform found at the edge of the discontinuous permafrost zone, where mean annual temperatures are close to 0 °C and climate change is expected to have a high impact. The palsas in Finnmark have been degrading for several decades – likely because of the amplified warming observed at high northern latitudes – which raises the concern of potential climate feedbacks from permafrost carbon release and surface energy balance shifts. While Finnmark and Fennoscandia may be small areas, they are part of the same permafrost zone as Siberia, and changes observed here might reveal what lies ahead in colder permafrost regions.

For turbulent fluxes we applied the eddy-covariance (EC) method, a widely used technique which requires fast-response measurements of the 3D wind and the constituents of interest, usually scalars. Complementary energy balance data was provided by a net radiometer and two soil heat flux plates installed at depths of 0.1 and 0.2 m. The raw turbulence data was processed by the validated TK3 software package, which applies the plausability tests, corrections and quality controls needed for reliable flux calculations. Through a footprint analysis we found the average turbulent fetch area to overlap well with our ecosystem of interest, in that only 20 % of the footprint climatology was outside the palsa mire. However, a significant dependence on wind direction was found for the net ecosystem exchange of CO_2 (NEE), which suggests that the more vegetated area outside of the palsa mire did influence our flux measurements.

The soil heat flux at both levels was positive most of the time, and from our cumulative flux estimates we found a substantial soil heat uptake during the campaign. Permafrost soils are known to accumulate heat in summertime when the active layer is deepening, more than soils in warmer regions. According to our readings, the 0.2 m level received more heat over time than the upper level, but this is likely an artifact of soil moisture disturbances. The average maximum daytime flux from our 0.1 m sensor was only 6 % of the corresponding net radiation, which is in general less than what other permafrost studies have found, likely due to the heat storage change above 0.1 m.

The weather conditions during the campaign were rainier than the climatology, which explains in part why the turbulent flux data coverage was only about 60 % in total. However, several interesting observations could be made despite these limitations. Our turbulent fluxes all showed a clear diurnal cycle and reached their maxima (minimum for the CO_2 flux) close to midday, because they were all strongly related to the net radiation. The wind speed seemed to control some of the remaining variability in the turbulent energy fluxes, in that the latent heat release was magnified at high winds, whereas the sensible heat was not.

The average NEE during the campaign was –1.1 μmol/m^{2}s, which indicates carbon uptake and compares well to what has been reported in other studies from similar sites in summertime. Differences in carbon budgets between sites seem to be associated with the vegetation cover. A certain long-term increase in [–NEE] was found, likely related to plant growth, wind direction differences and perhaps also soil warming and thereby active layer deepening.

The latent and sensible heat fluxes consumed on average 53 % and 25 % of the net radiation, respectively, and the mean daytime Bowen ratio was 74 %, which is typical for sub-Arctic wetlands in summer. We observed relatively higher Bowen ratios during northerly wind, but this had probably more to do with the greater sensible heat flux associated with cold air advection, than with the local footprint.

Our estimated surface energy budget showed a great imbalance – nonradiative fluxes could only account for 56 % of the net radiation, and even less at nighttime. We presented three explanations to this mismatch: systematic errors in the radiometer, limitations of the EC method and an underestimated ground heat flux. The latter two, which were probably the dominant error sources, were further investigated. Our ogive test suggested that a significant fraction of the turbulent fluxes were inadequately sampled with a block averaging period of only 30 min. It also confirmed our suspicion that large, undetected eddies were more important during the night. Unfortunately, there is no simple and straight-forward way to resolve this issue. One can, of course, increase the averaging time to e.g. one hour or more, but will then inevitably run into challenges related to non-stationarity.

On the other hand, soil heat transfer theory does offer a method for correcting heat flux plate measurements taken in the soil. We developed a novel approach to estimate the change in soil heat storage, using longwave radiation data for the surface temperature and the corresponding 10 cm soil temperature, and added this to the 0.1 m soil heat flux. While the result was strongly overestimated by the high heat capacity, this experiment illustrated that ground heat flux corrections are possible and can improve the surface energy balance.

The present work is part of a larger project, where e.g. chamber measurements are taken across hydrological gradients within the palsa mire. These are recorded on an annual basis and will provide information on the fine-scale variability in carbon exchange within the palsa mire, while our EC measurements allow for the upscaling of such fluxes. It will be interesting to see how vegetation and moisture affect the photosynthesis and respiration on our site. Obviously, no conclusions can be drawn on the annual carbon budget based on one summertime campaign, but awaited work on the continous measurements will shed light on this matter. We are particularly puzzled by our soil heat flux observations,

and recommend strongly to measure the soil temperature and moisture profiles in future studies, including the active layer depth. Finally, it should be noted again that other permafrost regions in for instance Russia are severely under-sampled by the scientific community, and require much greater attention than they have received so far.

Bibliography

Aalstad, K. (2015). Applying the Eddy Covariance Method Under Difficult Conditions. Lessons from the northernmost FLUXNET Site: Bayelva, Svalbard (70°N). Master's thesis, University of Oslo.

Ahlenius, H. (2007). Permafrost extent in the Northern Hemisphere. UNEP/GRID-Arendal. Accessed 2018-04-03, from $http://grid-arendal.herokuapp.com/resources/5234$.

Åhman, R. (1977). *Palsar i Nordnorge. En studie av palsars morfologi, utbredning och klimatiska förutsättningar i Finnmarks och Troms fylke*. PhD thesis, Lund University.

American Meteorological Society (2018). Atmospheric boundary layer. Accessed 2018-10-09, from $http://glossary.ametsoc.org/wiki/Atmospheric_boundary_layer$.

Andrews, D. (2000). *An Introduction to Atmospheric Physics*. Cambridge University Press, 2nd edition.

Arya, P. (2001). *Introduction to Micrometeorology*. Academic Press, 2nd edition.

Aubinet, M., Feigenwinter, C., Heinesch, B., Laffineur, Q., Papale, D., Reichstein, M., Rinne, J., and Van Gorsel, E. (2012). *The Eddy Covariance Method. A practical guide to measurement and data analysis*, chapter 5. Nighttime Flux Correction, pages 369–432. Springer.

Aubinet, M., Grelle, A., Ibrom, A., Rannik, Ü., Moncrieff, J., Foken, T., Kowalski, A., Martin, P., Berbigier, P., Bernhoffer, C., Clement, R., Elbers, J., Granier, A., Grünwald, T., Morgenstern, K., Pilegaard, K., Rebmann, C., Snijders, W., Valentini, R., and Vesala, T. (2000). *Estimates of the Annual Net Carbon and Water Exchange of Forests: The EUROFLUX Methodology*, volume 30, pages 113–175. Academic Press.

Aurela, M., Laurila, T., and Tuovinen, J. (2001). Seasonal CO_2 balances of a subarctic mire. *Journal of Geophysical Research*, 106:1623–1637.

Baldocchi, D. (2003). Assessing the eddy covariance technique for evaluating carbon dioxide exchange rates of ecosystems: past, present and future. *Global Change Biology*, 9:479–492.

Baldocchi, D., Falge, E., Gu, L., Olson, R., Hollinger, D., Running, S., Anthoni, P., Bernhoffer, C., Davis, K., Evans, R., Fuentes, J., Goldstein, A., Katul, G., Law, B., Lee, X., Malhi, Y., Meyers, T., Munger, W., Oechel, W., Paw U, K., Pilegaard, K., Schmid, H., Valentini, R., Verma, S., Vesala, T., Wilson, K., and Wofsy, S. (2001). FLUXNET: A new tool to study the temporal and spatial variability of ecosystem-scale carbon dioxide, water vapor, and energy flux densities. *Bulletin of the American Meteorological Society*, 82:2415–2434.

Baldocchi, D., Verma, S., and Rosenberg, N. (1981). Environmental Effects on the CO_2 Flux and CO_2–Water Flux Ratio of Alfalfa. *Agricultural Meteorology*, 24:175–184.

Blindheim, J. and Østerhus, S. (2005). *The Nordic Seas: An Integrated Perspective*, chapter The Nordic Seas, Main Oceanographic Features. American Geophysical Union.

Bolch, T. and Christiansen, H. (2015). *Snow and Ice-Related Hazards, Risks and Disasters 2015*, chapter 7 – Mountains, Lowlands, and Coasts: The Physiography of Cold Landscapes. Academic Press.

Borge, A., Westermann, S., Solheim, I., and Etzelmüller, B. (2017). Strong degradation of palsas and peat plateaus in northern Norway during the last 60 years. *The Cryosphere*, 11:1–16.

Brown, J. and Romanovsky, V. (2008). Report from the International Permafrost Association: State of Permafrost in the First Decade of the 21st Century. *Permafrost and Periglacial Processes*, 19:255–260.

Brown, R. (1967). Comparison of permafrost conditions in Canada and the USSR. *The Polar Record*, 13(87):741–751.

Brown, R. and Péwé, T. (1973). Distribution of permafrost in North America and its relationship to the environment: A review, 1963-1973. Technical report, Division of Building Research. National Research Council Canada.

Callaghan, T., Björn, L., Chapin III, F., Chernov, Y., Christensen, T., Huntley, B., Ims, R., Johansson, M., Riedlinger, D., Jonasson, S., Matveya, N., Oechel, W., Panikov, N., and Shaver, G. (2005). *Arctic Climate Impact Assessment*, chapter 7. Arctic Tundra and Polar Desert Ecosystems, pages 243–352. Cambridge University Press.

Campbell Scientific (2010). *CNR1, CNR1-L. Solar and Far Infrared Radiation Balance Radiometers. Brochure.*

Campbell Scientific (2012). *CSAT3 Three Dimensional Sonic Anemometer. Instruction Manual.*

Cassidy, A., Christen, A., and Henry, G. (2016). The effect of a permafrost disturbance on growing-season carbon-dioxide fluxes in a high Arctic tundra ecosystem. *Biogeosciences*, 13:2291–2303.

Chapin III, F., Matson, P., and Vitousek, P. (2011). *Principles of Terrestrial Ecosystem Ecology*. Springer, 2nd edition.

Chapin III, F., Woodwell, G., Randerson, J., Rastetter, E., Lovett, G., Baldocchi, D., Clark, D., Harmon, M., Schimel, D., Valentini, R., Wirth, C., Aber, J., Cole, J., Goulden, M., Harden, J., Heimann, M., Howarth, R., Matson, P., McGuire, A., Melillo, J., Mooney, H., Neff, J., Houghton, R., Pace, M., Ryan, M., Running, S., Sala, O., Schlesinger, W., and Schulze, E. (2006). Reconciling carbon-cycle concepts, terminology, and methods. *Ecosystems*, 9:1041–1050.

Christensen, T., Jackowicz-Korczyński, M., Aurela, M., Crill, P., Heliasz, M., Mastepanov, M., and Friborg, T. (2012). Monitoring the Multi-Year Carbon Balance of a Subarctic Palsa Mire with Micrometeorological Techniques. *Royal Swedish Academy of Sciences*, 41:207–217.

Christensen, T., Johansson, T., Åkerman, H., Mastepanov, M., Malmer, N., Friborg, T., Crill, P., and Svensson, B. (2004). Thawing sub-arctic permafros: Effects on vegetation and methane emissions. *Hydrology and Land Surface Studies*, 31:L04501.

Christiansen, H., Etzelmüller, B., Isaksen, K., Juliussen, H., Farbrot, J., Humlum, O., Johansson, M., Ingeman-Nielsen, T., Kristensen, L., hjort, J., Holmlund, P., Sannel, A., Sigsgaard, C., Åkerman, H., Foged, N., Blikra, L., Pernosky, M., and Ødegård, R. (2010). The Thermal State of Permafrost in the Nordic Area during the International Polar Year 2007–2009. *Permafrost and Periglacial Processes*, 21:156–181.

Ciais, P., Sabine, C., Bala, G., Bopp, L., Brovkin, V., Canadell, J., Chhabra, A., DeFries, R., Galloway, J., Heimann, M., Jones, C., Le Quéré, C., Myneni, R., Piao, S., and Thornton, P. (2013). *Climate Change 2013: The Physical Science Basis. Contribution of Working Group I to the Fifth Assessment Report of the Intergovernmental Panel on Climate Change*, chapter 6. Carbon and Other Biogeochemical Cycles. Cambridge University Press.

Cline, D. (1997). Snow surface energy exchanges and snowmelt at a continental, midlatitude alpine site. *Water Resources Research*, 33:689–701.

Collins, M., Knutti, R., Arblaster, J., Dufresne, J., Fichefet, T., Friedlingstein, P., Gao, X., Gutowski, W., Johns, T., Krinner, G., Shongwe, M., Tebaldi, C., Weaver, A., and Wehner, M. (2013). *Climate Change 2013: The Physical Science Basis. Contribution of Working Group I to the Fifth Assessment Report of the Intergovernmental Panel on Climate Change 2013: The Physical Science Basis. Contribution of Working Group I to the Fifth Assessment Report of the Intergovernmental Panel on Climate Change*, chapter 12. Long-term Climate Change: Projections, Commitments and Irreversibility. Cambridge University Press.

Dannevig, P. (2009). Finnmark – klima. Store norske leksikon. Accessed 2018-09-21.

Davidson, E. and Janssens, I. (2006). Temperature sensitivity of soil carbon decomposition and feedbacks to climate change. *Nature*, 440:165–173.

eKlima (2018). Free access to weather- and climate data from Norwegian Meteorological Institute from historical data to real-time observations, available at $http : //www.eklima.no$.

Encyclopædia Britannica (2018). Tundra climate. Accessed 2018-09-28, from $https : //www.britannica.com/science/tundra - climate$.

Euskirchen, E., Edgard, C., Bret-Harte, M., Kade, A., Zimov, N., and Zimov, S. (2017). Interannual and Seasonal Patterns of Carbon Dioxide, Water, and Energy Fluxes From Ecotonal and Thermokarst-Impacted Ecosystems on Carbon-Rich Permafrost Soils in Northeastern Siberia. *Journal of Geophysical Research: Biogeosciences*, 122:2651–2668.

Faber, T. (2018). Fluid mechanics. Accessed 2018-10-25, from $https : //www.britannica.com/science/fluid - mechanics$.

Fleagle, R. and Businger, J. (1980). *An Introduction to Atmospheric Physics*. Academic Press, 2nd edition.

Foken, T. (2006). 50 Years of the Monin-Obukhov Similarity Theory. *Boundary-Layer Meteorology*, 119:431–447.

Foken, T. (2008a). The energy balance closure problem: An overview. *Ecological Applications*, 18(6):1351–1367.

Foken, T. (2008b). *Micrometeorology*. Springer.

Foken, T., Aubinet, M., and Leuning, R. (2012a). *Eddy Covariance. A Practical Guide to Measurement and Data Analysis*, chapter 1. The Eddy Covariance Method, pages 1–16. Springer Atmospheric Series.

Foken, T., Leuning, R., Oncley, S., Mauder, M., and Aubinet, M. (2012b). *The Eddy Covariance Method. A practical guide to measurement and data analysis.*, chapter 4. Corrections and Data Quality Control, pages 85–131. Springer Atmospheric Sciences. Springer.

Foken, T., Wimmer, F., Thomas, C., and Liebethal, C. (2006). Some aspects of the energy balance closure problem. *Atmospheric Chemistry and Physics*, (6):4395–4402.

Fratini, G. and Mauder, M. (2014). Towards a consistent eddy-covariance processing: an intercomparison of EddyPro and TK3. *Atmospheric Measurement Techniques*, 7:2273–2281.

French, H., editor (1976). *The Periglacial Environment*. Longman, 2nd edition.

Furseth, A. (2011). Isvinteren 1880 – 1881 – og dei store snøskredkatastrofane i Nord-Noreg. *Ottar*, (285).

Garratt, J. (1992). *The atmospheric boundary layer*. Cambridge University Press.

Gentine, P., Entekhabi, D., and Heusinkveld, B. (2012). Systematic errors in ground heat flux estimation and their correction. *Water Resources Research*, 48:1–15.

Gisnås, K. (2011). Modelling of permafrost in norway using two equilibrium models. pages 49, 54.

Gisnås, K., Etzelmüller, B., Lussana, C., Hjort, J., Sannel, A., Isaksen, K., Westermann, S., Kuhry, P., Christiansen, H., Frampton, A., and Åkerman, J. (2016). Permafrost Map for Norway, Sweden and Finland. *Permafrost and Periglacial Processes*, 28:359–378.

Gjærevoll, O. (1978). *Finnmarksvidda. Natur-kultur*. Miljøverndepartementet.

Government of Canada (2018). Canadian climate normals 1981-2010 station data. Temperature and precipitation graph for 1981 to 2010 Canadian climate normals. Winnipeg Richardson Int'l A. Accessed 2018-09-21.

Grogan, P. and Jonasson, S. (2006). Ecosystem CO_2 production during winter in a Swedish subarctic region: the relative importance of climate and vegetation type. *Global Change Biology*, 12:1479–1495.

Guerney, S. (2001). Aspects of the genesis, geomorphology and terminology of palsas: perennial cryogenic mounds. *Progress in Physical Geography: Earth and Environment*, 25:249–260.

Halliwell, D. and Rouse, W. (1987). Soil heat flux in permafrost: characteristics and accuracy of measurement. *Journal of Climatology*, 7:571–584.

Halliwell, D., Rouse, W., and Weick, E. (1991). Surface energy balance and ground heat flux in organic permafrost terrain under variable moisture conditions. In *Fifth Canadian Proceedings, Nordicana*, number 54, pages 223–229.

Heginbottom, J., Brown, J., Humlum, O., and Svensson, H. (2013). Permafrost and periglacial environments. In Jr., R. W. and Ferrigno, J., editors, *State of the Earth's Cryosphere at the Beginning of the 21st Century: Glaciers, Global Snow Cover, Floating Ice, and Permafrost and Periglacial Environments*, pages A425–A496. US Geological Survey.

Heinonsalo, J. and Pumpanen, J. (2014). The link between plant photosynthesis and soil carbon and nitrogen dynamics. In Lehtoranta, J., Ekholm, P., Vihervaara, P., and Kortelainen, P., editors, *Coupled biogeochemical cycles and ecosystem services. Reports of the Finnish Environment Institute 21.*, page 17.

Hinzman, L. and Kane, D. (1992). Potential response of an arctic watershed during a period of global warming. *Journal of Geophysical Research*, 97:2811–2820.

Horst, T. and Weil, J. (1992). Footprint estimation for scalar flux measurements in the atmospheric surface layer. *Boundary-Layer Meteorology*, 59:279–296.

Hugelius, G., Strauss, J., Zubrycki, S., Harden, J., Schuur, E., Ping, C., Schirrmeister, L., Grosse, G., Michaelson, G., Koven, C., O'Donnell, J., Elberling, B., Mishra, U., Camill, P., Yu, Z., Palmtag, J., and Kuhry, P. (2014). Estimated stocks of circumpolar permafrost carbon with quantified uncertainty ranges and identified data gaps. *Biogeosciences*, 11:6573–6593.

Hukseflux (2016a). *User Manual HFP01 & HFP03. Heat flux plate / heat flux sensor*.

Hukseflux (2016b). *User Manual HFP01SC. Self-calibrating heat flux sensor.* Hukseflux Thermal Sensors B.V.

Kaimal, J. and Finnigan, J. (1994). *Atmospheric Boundary Layer Flows: their structure and measurement*. Oxford University Press, Inc.

Kaimal, J. and Gaynor, J. (1991). Another look at sonic thermometry. *Boundary-Layer Meteorology*, 56:401–410.

Kipp & Zonen (2002). *CNR 1 Net Radiometer. Instruction Manual.*

Kipp & Zonen (2003). *CG 3 Pyrgeometer. Instruction manual.*

Kipp & Zonen (2018). FAQ. Accessed 2018-10-02, from *http* : *//www.kippzonen.com/Knowledge − Center/FAQ*.

Kirkebøen, S. (2013). Karasjok varmest i Europa. *Aftenposten*. Accessed 2018-09-22.

Kljun, N. (2017). *Online tool of a simple two-dimensional parameterisation for Flux Footprint Prediction (FFP)*.

Kljun, N., Calanca, P., Rotach, M., and Schmid, H. (2004). A simple parameterisation for flux footprint predictions. *Boundary-Layer Meteorology*, 112:503–523.

Kljun, N., Calanca, P., Rotach, M., and Schmid, H. (2015). A simple two-dimensional parameterisation for Flux Footprint Prediction (FFP). *Geoscientific Model Development*, 8:3695–3713.

Köppen, W. (1936). *Handbuch der Klimatologie in fünf Bänden*, volume 1. Gebrüder Borntrager.

Kristiansen, S., Mamen, J., and Szewczyk-Bartnicka, H. (2017). Været i Norge. Klimatologisk månedsoversikt. Juli 2017. Technical report, Norwegian Meteorological Institute.

Kuhn, P. (1963). Measured effective long-wave emissivity of clouds. *Monthly Weather Review*, 91(10).

Kuhry, P., Dorrepaal, E., Hugelius, G., Schuur, E., and Tarnocai, C. (2010). Potential remobilization of belowground permafrost carbon under future global warming. *Permafrost and Periglacial Processes*, 21:208–214.

Lafleur, P., McCaughey, J., Joiner, D., Bartlett, P., and Jelinski, D. (1997). Seasonal trends in energy, water and carbon dioxide fluxes at a northern boreal wetland. *Journal of Geophysical Research*, 102:29,009–29,020.

Lantuit, H. and Pollard, W. (2008). Fifty years of coastal erosion and retrogressive thaw slump activity on Herschel Island, southern Beaufort Sea, Yukon Territory, Canada. *Geomorphology*, 96:84–102.

Laurila, T., Aurela, M., and Tuovinen, J. (2012). *The Eddy Covariance Method. A practical guide to measurement and data analysis*, chapter 14. Eddy Covariance Measurements over Wetlands, pages 913–966. Springer.

Laurila, T., Soegaard, H., Lloyd, C., Aurela, M., Tuovinen, J., and Nordstroem, C. (2001). Seasonal variations of net CO_2 exchange in European Arctic ecosystems. *Theoretical and Applied Climatology*, 70:183–201.

Le Quéré, C., Raupach, M., Canadell, J., Marland, G., Bopp, L., Ciais, P., Conway, T., Doney, S., Feely, R., Foster, P., Friedlingstein, P., Gurney, K., Houghton, R., House, J., Huntingford, C., Levy, P., Lomas, M., Majkut, J., Metzl, N., Ometto, J., Peters, G., Prentice, I., Randerson, J., Running, S., Sarmiento, J., Schuster, U., Sitch, S., Takashi, T., Viovy, N., van der Werf, G., and Woodward, F. (2009). Trends in the sources and sinks of carbon dioxide. *Nature Geoscience*, 2:831–836.

Leclerc, M. and Foken, T. (2014). *Footprints in Micrometeorology and Ecology*. Springer.

Lee, H., Schuur, E., Inglett, K., Lavoie, M., and Chanton, J. (2011). The rate of permafrost carbon release under aerobic and anaerobic conditions and its potential effects on climate. *Global Change Biology*, 18:515–527.

Lee, X., Finnigan, J., and Paw U, K. (2004). *Handbook of Micrometeorology. A guide for surface flux measurement and analysis.*, chapter 3. Coordinate Systems and Flux Bias Error, pages 33–66. Kluwer Academic Publishers.

Leuning, R. (2005). *Handbook of Micrometeorology. A guide for surface flux measurement and analysis.*, chapter 6. Measurements of Trace Gas Fluxes in the Atmosphere Using Eddy Covariance: WPL Corrections Revisited, pages 119–132. Kluwer Academic Publishers.

LI-COR (2004a). *Li-7000. CO_2/H_2O Analyzer. Instruction manual.*

LI-COR (2004b). *Li-7500 CO2/H2O Analyzer. Instruction manual.*

LI-COR (2005). *LI-7500 For Web*.

LI-COR (2018). Application note # 129. The importance of water vapor measurements and corrections. Technical report, LI-COR.

Liebethal, C. (2006). *On the determination of the ground heat flux in micrometeorology and its influence on the energy balance closure.* PhD thesis, University of Bayreuth.

Liebethal, C., Huwe, B., and Foken, T. (2005). Sensitivity analysis for two ground heat flux calculation approaches. *Agricultural and Forest Meteorology*, 132.

Malhi, Y., McNaughton, K., and Von Randow, C. (2004). *Handbook of Micrometeorology. A guide for surface flux measurement and analysis.*, chapter 5. Low Frequency Atmospheric Transport and Surface Flux Measurements. Kluwer Academic Publishers.

Marchgraber, R. (1967). Solar radiation as a meteorological parameter and its measurement. *Section of planetary sciences, U.S. Army Electronics Command, Fort Monmouth, N.J.*, 29(6):755.

Massman, W. and Clement, R. (2004). *Handbook of Micrometeorology. A guide for surface flux measurement and analysis*, chapter 4. Uncertainty in eddy covariance flux measurements resulting from spectral attenuation, pages 67–99. Kluwer Academic Publishers.

Mauder, M., Cuntz, M., Drüe, C., Graf, A., Rebmann, C., Schmid, H., Schmidt, M., and Steinbrecher, R. (2013). A strategy for quality and uncertainty assessment of long-term eddy-covariance measurements. *Agricultural and Forest Meteorology*, 169:122–135.

Mauder, M. and Foken, T. (2015). *Documentation and Instruction Manual of the Eddy-Covariance Software Package TK3 (update)*.

McFadden, J., Chapin III, F., and Hollinger, D. (1998). Subgrid-scale variability in the surface energy balance of arctic tundra. *Journal of Geophysical Research*, 103:28,947–28,961.

Metcalfe, D., Hermans, T., Ahlstrand, J., Becker, M., Berggren, M., Björk, R., Björkman, M., Blok, D., Chaudhary, N., Chisholm, C., Classen, A., Hasselquist, N., Jonsson, M., Kristensen, J., Kumordzi, B., Lee, H., Mayor, J., Prevéy, J., Pantazatou, K., Rousk, J., Sponseller, R., Sundqvist, M., Tang, J., Uddling, J., Wallin, G., Zhang, W., Ahlström, A., Tenenbaum, D., and Abdi, A. (2018). Patchy field sampling biases understanding of climate change across the Arctic. *Nature Ecology & Evolution*, 2:1443–1448.

Mikan, C., Schimel, J., and Doyle, A. (2002). Temperature controls of microbial respiration in arctic tundra soils above and below freezing. *Soil Biology and Biochemisty*, 34:1785–1795.

Montgomery, R. (1948). Vertical eddy flux of heat in the atmosphere. *Journal of meteorology*, 5:265–274.

Moore, C. (1986). Frequency response corrections for eddy correlation systems. *Boundary-Layer Meteorology*, 37:17–35.

Muller, S. (1947). *Permafrost or Permanently Frozen Ground and Related Engineering Problems*. Military Intelligence Division Office, Chief of Engineers. US Army.

Munn, R. (1966). *Descriptive Micrometeorology*. Academic Press.

Nawri, N. and Harstveit, K. (2012). Variability of surface wind directions over Finnmark, Norway, and coupling to the larger-scale atmospheric circulation. *Theoretical and Applied Climatology*, 107:15–33.

Norsk klimaservicesenter (2016). Klimaprofil: Finnmark. et kunnskapsgrunnlag for klimatilpasning. Technical report.

NVE (2018). SeNorge. Accessed 2018-09-21.

Nykänen, H., Heikkinen, J., Pirinen, L., Tiilikainen, K., and Martikainen, P. (2003). Annual CO_2 exchange and CH_4 fluxes on a subarctic palsa mire during climatically different years. *Global Biogeochemical Cycles*, 17:1018.

Oechel, W., Vourlitis, G., Hastings, S., Zulueta, R., Hinzman, L., and Kane, D. (2000). Acclimation of ecosystem CO_2 exchange in the Alaskan Arctic in response to decadal climate warming. *Nature*, 406:978–981.

Ohmura, A. (1982). Climate and energy balance on the Arctic tundra. *Journal of Climatology*, 2:65–84.

Ohmura, A. (2012). Present status and variations in the arctic energy balance. *Polar Science*, 6(1).

Oke, T. (1987). *Boundary Layer Climates*, volume 2. Routledge.

Olefeldt, D., Roulet, N., Bergeron, O., Crill, P., Bäckstrand, K., and Christensen, T. (2012). Net carbon accumulation of a high-latitude permafrost palsa mire similar to permafrost-free peatlands. *The Cryosphere*, 39:L03501.

Oncley, S., Foken, T., Vogt, R., Kohsiek, W., de Bruin, H., Bernhofer, C., Christen, A., van Gorsel, E., Grantz, D., Feigenwinter, C., Lehner, I., Liebethal, C., Liu, H., Mauder, M., Pitacco, A., Ribeiro, L., and Weidinger, T. (2007). The Energy Balance Experiment EBEX-2000. part i: overview and energy balance. *Boundary-Layer Meteorology*, 123:1–28.

O'Shea, S., Allen, G., Gallagher, M., Bower, K., Illingworth, S., Muller, J., Jones, B., Percival, C., Bauguitte, S., Cain, M., Warwick, N., Quiquet, A., Skiba, U., Drewer, J., Dinsmore, K., Nisbet, E., Lowry, D., Fisher, R., France, J., Aurela, M., Lohila, A., Hayman, G., George, C., Clark, D., Manning, A., Friend, A., and Pyle, J. (2014). Methane and carbon dioxide fluxes and their regional scalability for the European Arctic wetlands during the MAMM project in summer 2012. *Atmospheric Chemistry and Physics*, 14:13159–13174.

Osterkamp, T. and Burn, C. (2015). Cryosphere | permafrost. In North, G., Pyle, J., and Zhang, F., editors, *Encyclopedia of Atmospheric Sciences*, volume 2, pages 208–216. Elsevier Science Ltd.

Pearson, R., Phillips, S., Loranty, M., Beck, P., Damoulas, T., Knight, S., and Goetz, S. (2013). Shifts in arctic vegetation and associated feedbacks under climate change. *Nature Climate Change*, 3:673–677.

Pedersen, K. (2013). Eli Kari besøker stedet uten sommer. Accessed 2018-09-28, from $http://www.yr.no/artikkel/her-er-det-aldri-sommer-1.11158527$.

Péwé, T. (2018). Permafrost. *Encyclopædia Britannica, Inc.* Accessed 2018-09-26.

PVEducation (2018). Calculation of solar insolation. Accessed 2018-10-02, from $https://www.pveducation.org/pvcdrom/properties-of-sunlight/calculation-of-solar-insolation$.

Rannik, Ü., Sogachev, A., Foken, T., Göckede, M., Kljun, N., Leclerc, M., and Vesala, T. (2012). *The Eddy Covariance Method. A practical guide to measurement and data analysis*, chapter 8. Footprint analysis. Springer Atmospheric Sciences. Springer.

Rebmann, C., Kolle, O., Heinesch, B., Queck, R., Ibrom, A., and Aubinet, M. (2012). *The Eddy Covariance Method. A practical guide to measurement and data analysis*, chapter 3. Data Acquisition and Flux Calculations, pages 59–84. Springer Atmospheric Sciences. Springer.

Rosenberg, N., Blad, B., and Verma, S. (1983). *Microclimate. The biological environment*, volume 2. John Wiley & Sons, Inc.

Schädel, C., Bader, M., Schuur, E., Biasi, C., Bracho, R., Čapek, P., De Baets, S., Diáková, K., Ernakovich, J., Estop-Aragones, C., Graham, D., Hartley, I., Kane, C. I. E., Knoblauch, C., Lupascu, M., Martikainen, P., Natali, S., Norby, R., O'Donnell, J., Chowdhury, T., Šantrůčková, H., Shaver, G., Sloan, V., Treat, C., Turetsky, M., Waldrop, M., and Wickland, K. (2016). Potential carbon emissions dominated by carbon dioxide from thawed permafrost soils. *Nature Climate Change*, 6:950–953.

Schlesinger, W. (1991). *Biogeochemistry: an analysis of global change*. Academic Press.

Schotanus, P., Nieuwstadt, F., and de Bruin, H. (1983). Temperature-measurement with a sonic anemometer and its application to heat and moisture flux. *Boundary-Layer Meteorology*, 26:81–93.

Schuur, E., Bockheim, J., Canadell, J., Euskirchen, E., Field, C., Goryachkin, S., Hagemann, S., Kuhry, P., Lafleur, P., Lee, H., Mazhitova, G., Nelson, F., Rinke, A., Romanovsky, V., Shiklomanov, N., Tarnocai, C., Venevsky, S., Vogel, J., and Zimov, S. (2008). Vulnerability of permafrost carbon to climate change: Implications for the global carbon cycle. *BioScience*, 58:701–714.

Schuur, E., McGuire, A., Schädel, C., Grosse, G., Harden, J., Hayes, D., Hugelius, G., Koven, C., Kuhry, P., Lawrence, D., Natali, S., Olefeldt, D., Romanovsky, V., Schaefer, K., Turetsky, M., Treat, C., and Vonk, J. (2015). Climate change and the permafrost carbon feedback. *Nature*, 520:171–179.

Scott, P. and Rouse, W. (1995). Impacts of increased winter snow cover on upland tundra vegetation: a case example. *Climate Research*, 5:25–30.

Seppälä, M. (2011). Synthesis of studies of palsa formation underlining the importance of local environmental and physical characteristics. *Quaternary Research*, 75:366–370.

Siedlecki, M., Pawlak, W., Fortuniak, K., and Zieliński, M. (2016). Wetland Evapotranspiration: Eddy Covariance Measurement in the Biebrza Valley, Poland. *Wetlands*, 36:1055–1067.

Sievers, J., Papakyriakou, T., Larsen, S., Jammet, M., Rysgaard, S., Sejr, M., and Sørensen, L. (2015). Estimating surface fluxes using eddy covariance and numerical ogive optimization. *Atmospheric Chemistry and Physics*, 15:2081–2103.

Stiegler, C., Johansson, M., Christensen, T., Mastepanov, M., and Lindroth, A. (2016). Tundra permafrost thaw causes significant shifts in energy partitioning. *Tellus B: Chemical and Physical Meteorology*, 68.

Stieglitz, M., Déry, S., Romanovsky, V., and Osterkamp, T. (2003). The role of snow cover in the warming of arctic permafrost. *Geophysical Research Letters*, 30:54 – 1 – 54 – 4.

Stocker, T., Qin, D., Plattner, G., Alexander, L., Allen, S., Bindoff, N., Bréon, F., Church, J., Cubasch, U., Emori, S., Forster, P., Friedlingstein, P., Gillett, N., Gregory, J., Hartmann, D., Jansen, E., Kirtman, B., Knutti, R., Krishna Kumar, K., Lemke, P., Marotzke, J., Masson-Delmotte, V., Meehl, G., Mokhov, I., Piao, S., Ramaswamy, V., Randall, D., Rhein, M., Rojas, M., Sabine, C., Shindell, D., Talley, L., Vaughan, D., and Xie, S. (2013). *Climate Change 2013: The Physical Science Basis. Contribution of Working Group I to the Fifth Assessment Report of the Intergovernmental Panel on Climate Change*, chapter Technical Summary. Cambridge University Press.

Stull, R. (1988). *An Introduction to Boundary Layer Meteorology*. Kluwer Academic Publishers.

Tanner, C. and Thurtell, G. (1969). Anemoclinometer measurements of reynolds stress and heat transport in the atmospheric surface layer. *Research and Development Technical Report. ECOM 66-G22-F to the United States Army Electronics Command*.

Tarnocai, C., Canadell, J., Schuur, E., Kuhry, P., Mahzitova, G., and Zimov, S. (2009). Soil organic carbon pools in the northern circumpolar permafrost region. *Global Biogeochemical Cycles*, 23:GB2023.

te Beest, M., Sitters, J., Ménard, C., and Olofsson, J. (2016). Reindeer grazing increases summer albedo by reducing shrub abundance in arctic tundra. *Environmental Research Letters*, 11:1–13.

Trenberth, K., Fasullo, J., and Kiehl, J. (2009). Earth's global energy budget. *Bulletin of the American Meteorological Society*, 90(3):311.

Vallée, S. and Payette, S. (2007). Collapse of permafrost mounds along a subarctic river over the last 100 years (northern Québec). *Geomorphology*, 90:162–170.

van Everdingen, R., editor (1998). *Multi-language glossary of permafrost and related ground-ice terms*. International Permafrost Association.

Vickers, D. and Mahrt, L. (1997). Quality Control and Flux Sampling Problems for Tower and Aircraft Data. *Journal of Atmospheric and Oceanic Technology*, 14:512–526.

Vikhamar-Schuler, D., Hanssen-Bauer, I., and Førland, E. (2010). Long-term climate trends of Finnmarksvidda, Northern Norway. Met.no report 6, Norwegian Meteorological Institute.

Vinjar, A. and Askheim, S. (2017). Finnmarks energi. Accessed 2018-09-28, from $https://snl.no/Finnmarks_energi$.

Vourlitis, G. and Oechel, W. (1999). Eddy covariance measurements of CO_2 and energy fluxes of an alaskan tussock tundra ecosystem. *Ecology*, 80:686–701.

Wallace, J. and Hobbs, P. (2006). *Atmospheric Science. An Introductory Survey.* Academic Press.

Washburn, A. (1973). *Periglacial processes and environments*. Edward Arnold [publishers] Ltd.

Webb, E., Pearman, G., and Leuning, R. (1980). Correction of flux measurements for density effects due to heat and water vapour transfer. *Quarterly Journal of the Royal Meteorological Society*, 106:85–100.

West, E. (1952). A study of the annual soil temperature wave. *Australian Journal of Scientific Research, Series A: Physical Sciences*, 5.

Westermann, S., Lüers, J., Lander, M., Piel, K., and Boike, J. (2009). The annual surface energy budget of a high-arctic permafrost site on Svalbard, Norway. *The Cryosphere*, 3:245–263.

Wilczak, J., Oncley, S., and Stage, S. (2001). Sonic anemometer tilt correction algorithms. *Boundary-Layer Meteorology*, 99:127–150.

Wilson, K., Goldstein, A., Falge, E., Aubinet, M., Baldocchi, D., Berbigier, P., Bernhofer, C., Ceulemans, R., Dolman, H., Field, C., Grelle, A., Ibrom, A., Law, B., Kowalski, A., Meyers, T., Moncrieff, J., Monson, R., Oechel, W., Tenhunen, J., Valentini, R., and Verma, S. (2002). Energy Balance Closure at FLUXNET Sites. *Agricultural and Forest Meteorology*, 113:223–243.

World Meteorological Organization (2008). *Guide to Meteorological Instruments and Methods of Observation*, chapter 5. Measurement of surface wind. Number 8. WMO, 7 edition.

Wyngaard, J. (2010). *Turbulence in the Atmosphere*. Cambridge University Press.

yr.no (2018a). Weather statistics for Iškoras observation site. Accessed 2018-10-04.

yr.no (2018b). Weather statistics for Karasjok (finnmark). Accessed 2018-09-21.

Zhang, R., Huang, J., Wang, X., Zhang, J., and Huang, F. (2016). Effects of precipitation on sonic anemometer measurements of turbulent fluxes in the atmospheric surface layer. *Oceanic and Coastal Research*, 15:389–398.

Zhang, T. (2005). Influence of the seasonal snow cover on the ground thermal regime: An overview. *Reviews of Geophysics*, 43:RG4002.

Zuidhoff, F. and Kostrup, E. (2000). Changes in Palsa Distribution in Relation to Climate Change in Laivadalen, Northern Sweden, Especially 1960-1997. *Permafrost and Periglacial Processes*, 11:55–69.